Non-Double-Couple Components in Moment Tensors of Aftershock Seismicity and Laboratory Earthquakes

DISSERTATION
zur Erlangung des akademischen Grades

Doktor der Naturwissenschaften
(Dr. rer. Nat.)

In der Wissenschaftsdisziplin Geophysik
eingereicht an der Geowissenschaftlichen Fakultät
der Freien Universität Berlin

vorgelegt von Eva Stierle
Berlin, Mai 2015

Eidesstattliche Erklärung

Ich erkläre hiermit an Eides statt, dass ich die vorliegende Dissertation selbstständig und nur unter Verwendung der angegebenen Quellen und Hilfsmittel angefertigt habe.

Berlin, den 18.05.2015

Referent	Prof. Dr. Marco Bohnhoff
Korreferent	Dr. Vaclav Vavryčuk
Datum der Disputation	10.07.2015

Freie Universität Berlin

Fachbereich Geowissenschaften

Institut für Geologische Wissenschaften

Malteserstr. 74 – 100

12249 Berlin

Summary

Recent developments in waveform data-acquisition technology in combination with improved methods of modelling of seismic waves have enabled us to study the details of physical processes in earthquake sources with an unprecedented accuracy. This has revealed that the common assumption that earthquakes represent shear faulting on a planar rupture in an isotropic Earth's crust is too simplistic and does not explain data adequately. The complexities of the earthquake process are, in particular, evidenced by the presence of non-double-couple (non-DC) components frequently observed in seismic moment tensors. Early studies showed, however, that non-DC components are difficult to determine accurately being often contaminated by numerical errors. The non-DC components are sensitive to noise in the input data, to errors in the modelling procedure, to a velocity model, to an earthquake location and to the amount of data in terms of the focal sphere coverage. In addition, their physical origin covers a broad range of possibilities, which further complicates the interpretation of the non-DC components. Therefore, high-quality data with good focal sphere coverage and detailed knowledge of the medium are essential for determining reliable non-DC components. This thesis deals with the determination and error analysis of the non-DC components of seismic moment tensors. In the thesis, the state-of-the-art moment tensor inversion algorithms are refined and extensive synthetic tests are performed in order to study the uncertainties and resolvability of the non-DC components. By analysing high-quality waveform data of earthquakes on various scales, the non-DC components are retrieved and suggestions for their physical origin are given.

On the field scale, the aftershock sequence of the M_w=7.4 1999 Izmit earthquake in northwestern Turkey is analysed. The analysed earthquake catalogue contains waveforms of more than 4000 relative relocated events observed at 35 three-component short-period seismic stations surrounding the rupture zone. The Izmit earthquake is one of the best studied M>7 earthquakes worldwide and therefore detailed knowledge of the tectonic setting is available. To analyse the sensitivity of the given network to detecting source-related non-DC components, a synthetic case study is performed. In addition, two different moment tensor inversion approaches were tested – a linear full moment tensor inversion and a non-linear moment tensor inversion, which is constrained to the shear-tensile source model. A synthetic dataset mimicking seismic observations of aftershock recordings of the 1999 Izmit earthquake was modelled, adopting the shear-tensile source model. To analyse the resolution capability of the network, synthetic amplitudes were contaminated with artificial noise. In addition realistic errors in the location as well as in the velocity model were considered. The synthetic tests revealed that the error bounds for the ISO and the CLVD component remain considerable at approximately ±15%, while the orientations of P- and T-axes are well determined even when errors in the modelling procedure are high. In general, the tests showed that the aftershock recordings lack observations with near-epicentral distances (<15 km), which causes irregular focal sphere coverage. Thus, finding stable moment tensor solutions is a difficult task for the given network geometry. However, the non-linear inversion is constrained to a shear-tensile source model, which yields significantly smaller errors in the non-DC components compared to the full moment tensor inversion. In particular, the errors in the CLVD component are reduced.

After completing the synthetic tests, the analysis of aftershock recordings was performed by inverting P- and S-wave amplitudes for the moment tensor. Prior to the inversion, strict selection criteria were applied to the event catalogue reducing the number

of events from more than 4000 to only 33. This is mostly due to the poor focal sphere coverage. The 33 moment tensors display significant differences in the percentage of the non-DC components for the three distinct fault segments in the study area: the Izmit-Sapanca, Karadere-Düzce and the Akyazi segments. Events located in the Izmit-Sapanca and Karadere-Düzce segments show mainly strike-slip mechanisms with rather low percentages of the non-DC components, which are mainly positive if present. This correlates well with the predominant pure shear, strike-slip stress regime along this segment and also with the main shock rupture comprising a right lateral strike-slip. In contrast, we found substantial percentages of the non-DC components for events below the Akyazi Plain, which is a pull-apart structure. The observed non-DC components are entirely positive, indicating a tensional regime, and range from 20 to 48%, clearly exceeding the defined error bounds assessed from the synthetic case study. This observation is in accordance with the post-seismic setting following the Izmit main shock that left a remarkable slip deficit of 3.5 m below the Akyazi bend. The tension throughout the seismogenic layer might have allowed fluids to migrate upwards, thereby reducing effective normal traction (or friction) on coseismically stressed normal faults and accelerating the compensation of the slip deficit.

On the laboratory scale, a newly developed moment tensor inversion approach was implemented and applied to acoustic emission waveform recordings. During rock deformation experiments in the laboratory with differential loading, the seismic velocities become highly anisotropic and waves were attenuated due to opening or closure of microcracks. In this part of the thesis, the sensitivity of the moment tensor inversion to anisotropy of P-wave velocities and attenuation of the rock sample was studied. Neglecting attenuation and anisotropy of P-wave velocities in the moment tensor inversion can produce significant uncertainties in the retrieved moment tensors and may lead to misinterpretations of the source mechanisms. Interestingly, the sensitivity depends on the fracturing mode of AEs. The tensile events are more sensitive to anisotropy of the P-wave velocity and attenuation of the sample than the shear events. Furthermore, the geometry of faulting in anisotropic rock samples should be studied using the source tensors, since the P and T axes of the moment tensors are affected by anisotropy of the P-wave velocity and deviate from the true orientation of faulting. The stronger the anisotropy the higher the deviations are. Finally, the moment tensor inversion was applied to a large dataset of AEs to find optimum values of the attenuation parameters of the rock sample in a grid-search scheme. The resolution of the method is sufficiently high for quantitatively distinguishing anisotropic behaviour of attenuation of P-waves. The method is capable of measuring differences between the P-wave attenuation in the horizontal and vertical directions in the sample and allows detection of the effects of dilatant cracking according to the stress regime.

The results obtained here for datasets on the laboratory as well as on the field scale demonstrate the challenges in reliably determining and interpreting the non-DC components. The analysis revealed the importance of evaluating the non-DC components for studying fracture modes during earthquake processes and for understanding their driving mechanisms. In addition, the analysis showed that a joint inversion for moment tensors of a family of earthquakes is capable of providing not only information on seismic sources but also on seismic anisotropy and attenuation in the focal zone.

Zusammenfassung

Neuste Entwicklungen in dem Bereich der Akquisition von seismischen Wellenfelddaten in Kombination mit verbesserten Konzepten der Momententensor-Inversion bilden die Basis für die vorliegende Dissertation. In den letzten Jahrzehnten hat sich in der seismologischen Fachwelt die Überzeugung durchgesetzt, dass die Annahme eines reinen Scherbruchs nicht ausreicht, um z.B. signifikante Nicht-Scheranteile im Herdprozess zu beschreiben. Erste Studien dazu haben ergeben, dass die Nicht-Scheranteile sich sensitiv gegenüber Rauschen in den Daten, Fehlern in der Modellierung und der Herdflächenüberdeckung verhalten. Daher sind hochqualitative Daten mit einer optimalen Herdflächenüberdeckung und detaillierte Kenntnisse über das durchlaufene Medium essentiell für eine zuverlässige Bestimmung von Nicht-Scheranteilen. Die vorliegende Dissertation beschäftigt sich mit der Bestimmung und Analyse von Nicht-Scheranteilen auf zwei verschiedenen Skalen, um deren Auflösung und physikalischen Ursprung unter Verwendung von hochqualitativen Daten und der Weiterentwicklung von Momententensor-Inversionsalgorithmen zu untersuchen.

Auf der Feld-Skala wurde die Nachbebenserie des M_w=7.4 Izmit Erdbebens von 1999 im Nordwesten der Türkei analysiert. Der Erdbebenkatalog umfasst mehr als 4000 relokalisierte Erdbeben, welche von einem 35 Stationen-Netzwerk, ausgestattet mit kurzperiodischen, 3-Komponenten Seismometern, aufgezeichnet wurden. Vor der Analyse der Nachbeben in Bezug auf das Auftreten von möglichen Nicht-Scheranteilen wurde eine umfangreiche synthetische Studie durchgeführt, um das Auflösungsvermögen des Netzwerkes zur Erfassung von quellgebundenen Nicht-Scheranteile zu analysieren. Weiterhin wurden zwei verschiedene Inversionsalgorithmen getestet – eine lineare Momententensor-Inversion, in welcher der volle Momententensor bestimmt wird, und eine nichtlineare Momententensor-Inversion, welche auf das Model des kombinierten Scher-Zugbruches beschränkt ist. Dazu wurde ein synthetischer Datensatz generiert, welcher seismische Beobachtungen des Izmit-Erdbebens mit dem Modell des Scher-Zugbruches simuliert. Um das Auflösungsvermögen des Netzwerkes zu untersuchen, wurden die synthetischen Amplituden mit zufällig verteiltem Rauschen überlagert und es wurden weiterhin Fehler in den Lokalisierungen und Fehler im Geschwindigkeitsmodell eingebaut. Die synthetische Studie hat ergeben, dass die Fehlergrenzen der Nicht-Scheranteile beträchtlich sind und annähernd ±15% betragen. Die Ausrichtung der P- und T-Achsen dagegen ist gut bestimmt auch für den Fall verhältnismäßig großer Fehler in der Modellierung. Die nichtlineare Inversion, welche auf den Scher-Zugbruch beschränkt ist, ergibt kleinere Fehler in den Nicht-Scheranteilen als die lineare Momententensor-Inversion, welche den vollen Momententensor bestimmt. Insbesondere Fehler in der CLVD (engl. compensated linear vector dipole) Komponente können deutlich reduziert werden. Insgesamt hat die Studie gezeigt, dass viele der Nachbebenaufzeichnungen eine schlechte Überdeckung der Herdfläche aufweisen, da Beobachtungen mit kurzen epizentralen Abständen (<15 km) fehlen. Dadurch ist es problematisch, stabile Momententensorlösungen zu erhalten.

Nach Abschluss der synthetischen Studie wurde die Analyse der Nachbebenserie des Izmit-Bebens durchgeführt, indem der Momententensor durch die Inversion von P- und S-Wellenamplituden bestimmt wurde. Zunächst wurde der gesamte Erdbebenkatalog durch strenge Auswahlkriterien gefiltert, wodurch sich die Anzahl der Beben von über 4000 auf nur 33 reduziert hat. Dies ist hauptsächlich der limitierten Herdkugelüberdeckung geschuldet. Die 33 stabilen, hochqualitativen Momententensorlösungen zeigen signifikante

Unterschiede in den prozentualen Nicht-Scheranteilen entlang der drei untersuchten Verwerfungssegmente des Izmit Erdbebens: dem Izmit-Sapanca, dem Karadere-Dücze und dem Akyazi Segment. Beben, welche in dem Izmit-Sapanca und dem Karadere-Dücze Segment lokalisiert sind, zeigen hauptsächlich Blattverschiebungen mit eher kleinen prozentualen Nicht-Scheranteilen, welche überwiegend positiv sind. Diese Ergebnisse stimmen gut mit den vorwiegend Scherungs- und Blattverschiebungsregime entlang dieser Segmente der Verwerfung und mit der dextralen Blattverschiebung des Hauptbebens überein. Im Gegensatz dazu weisen Beben, die unterhalb der Akyazi-Ebene, einem Pull-apart-Becken, auftreten, signifikante Nicht-Scheranteile auf. Diese Nicht-Scheranteile sind alle positiv und deuten damit eine Dehnungskomponente im Quellmechanismus an. Sie reichen von 20% bis 48% und liegen damit deutlich über der in der synthetischen Studie bestimmten Fehlergrenze. Diese Beobachtung erklärt die postseismischen Gegebenheiten nach dem Izmit-Hauptbeben, welches ein beträchtliches laterales Verschiebungsdefizit von 3.5 m unterhalb der Akyazi-Ebene hinterlassen hat. Die resultierenden Spannungen in der seismogenen Kruste könnten es Fluiden erlaubt haben, sich aufwärts zu bewegen, und dabei die effektive Normalspannung auf coseismisch unter Spannung gesetzte Abschiebungen zu reduzieren. Die Aktivierung der Abschiebungen mit signifikanten Dehnungskomponenten wiederum hat zur Kompensation des Verschiebungsdefizites in der Region beigetragen.

Auf der Laborskala wurde ein neuer Ansatz für die Momententensor-Inversion entwickelt und auf Wellenformregistrierungen von Laborerdbeben (engl. Acoustic Emission - AE) angewendet. Bei Deformationsexperimenten unter triaxialer Belastung von Gesteinsproben im Labor werden aufgrund der Öffnung und Schließung von Mikrorissen die seismischen Geschwindigkeiten anisotrop und elastische Wellen werden stärker gedämpft. Im Rahmen der Dissertation wurde ein Inversionsalgorithmus in visko-elastischen anisotropen Medien entwickelt um die Sensitivität von Momententensoren gegenüber den anisotropen P-Wellengeschwindigkeiten und den Dämpfungsparametern des Gesteins zu untersuchen. Es hat sich gezeigt, dass signifikante Fehler in den Momententensoren auftreten können, wenn die Dämpfung und die Anisotropie in den P-Wellengeschwindigkeiten nicht berücksichtigt werden. Interessanterweise hängt die Sensitivität von dem Quellmechanismus ab. Dehnungsbrüche sind empfindlicher gegenüber der Anisotropie von P-Wellengeschwindigkeiten und den Dämpfungsparametern des Gesteins als reine Scherbrüche. Außerdem sollte die Geometrie des Quellmechanismus in anisotropen Medien vom Quelltensor abgeleitet werden, da die P- und T-Achsen des Momententensors von den elastischen Parametern des umgebenden Gesteins beeinflusst werden und stark von der wahren Ausrichtung abweichen können. Je stärker die Anisotropie ausgeprägt ist, desto größer sind die Abweichungen. Schließlich wurde die Momententensor-Inversion in anisotropen und visko-elastischen Medien in einem Gitternetz-Such-Verfahren (engl. Grid-Search) auf einen großen Datensatz mit AEs angewendet, um die Dämpfungsparameter des Gesteins zu bestimmen. Die Methode erlaubt es, den Unterschied in den Dämpfungsparametern in horizontaler und vertikaler Richtung aufzulösen, welcher durch Mikrorisse verursacht wird.

Zusammenfassend lässt sich sagen, dass beide, die Labor- und die Feldskala, die Herausforderungen in Bezug auf die Bestimmung und Analyse von Nicht-Scheranteilen aufzeigen. Die Untersuchung von Nicht-Scheranteilen auf beiden Skalen trägt zu einem besseren Verständnis der grundlegenden Mechanismen von Nicht-Scheranteilen bei und verdeutlicht den Einfluss von äußeren Randbedingungen und Gesteinsparametern des durchlaufenen Mediums auf die Entstehung von Nicht-Scheranteilen im seismischen Quellprozess.

Contents

1 General Introduction

The Earth is a dynamic planet and continuously at unrest. Human activity, waves of the ocean, volcanic, tectonic and atmospheric processes continuously produce perpetual elastic vibrations within the Earth. Seismology describes seismic sources, the propagation of the elastic waves generated by these processes and the medium through which they propagate. The signals comprise a wealth of information that allows seismologists to quantify active wave sources and determine structures and processes at all depths throughout the planetary interior.

A large variety of seismic sources exists. Earthquakes, which occur at plate boundaries, deep in the Earth's mantle, within continents or in the frame of volcanic and geothermal regions, are the most prominent natural sources. Since a single earthquake can kill tens of thousands of people and cause huge economic losses it is of high interest for the human society to better understand the origin and driving mechanisms of destructive earthquakes, volcanic eruptions, tsunamis and the associated seismic hazard and risk. Predicting exactly when such natural risks will occur is a complicated task, but key advances have already been made by monitoring the seismicity in the Earth's subsurface using sensitive instrumentation. Here, potential locations of future earthquakes can be defined to setup early warning systems via integrated earth science infrastructure. Another societal and political application of seismology is to verify compliance with the Nuclear-Test-Ban-Treaty by monitoring nuclear testing. Likewise, seismology plays an important role in discovering, exploiting, and managing natural resources that power global civilization. Here, seismology focusses on the analysis of artificial seismic sources such as explosions, mine collapses, quarry blasts or seismicity induced by the extraction of hydrocarbons. This research field in seismology is becoming more and more important because the number of earthquakes associated with human activities has dramatically increased during the last few decades (Ellsworth, 2013). A better understanding of boundary conditions and mechanisms of such events should lead to improved policies for the regulation and operation of exploitation of natural resources.

The primary task of most applications in seismology is to quantify earthquakes by determining earthquake source parameters such as magnitudes, locations, focal mechanisms, source time function, seismic moment tensors, etc. The analysis of seismic moment tensors is one of the most efficient tools for describing and investigating earthquake source processes with a high precision. The moment tensor represents equivalent body forces acting at a seismic point source (Burridge & Knopoff, 1964; Gilbert, 1971; Backus & Mulcahy, 1976) and is today routinely used for describing seismic sources of all scales: from acoustic emissions and micro-earthquakes to large devastating earthquakes (Kanamori & Given, 1982; Dziewonski & Woodhouse, 1983; Jost & Herrmann, 1989).

The significance of moment tensors is emphasized by the existence of global, regional and local moment tensor catalogues continuously accumulating moment tensors of high precision for large earthquakes over the whole Earth (USGS catalogue, Harvard Centroid Moment Tensor (CMT) Catalogue) or for moderate and small earthquakes in certain seismoactive regions (e.g. European-Mediterranean Regional CMT catalogue, Swiss Regional

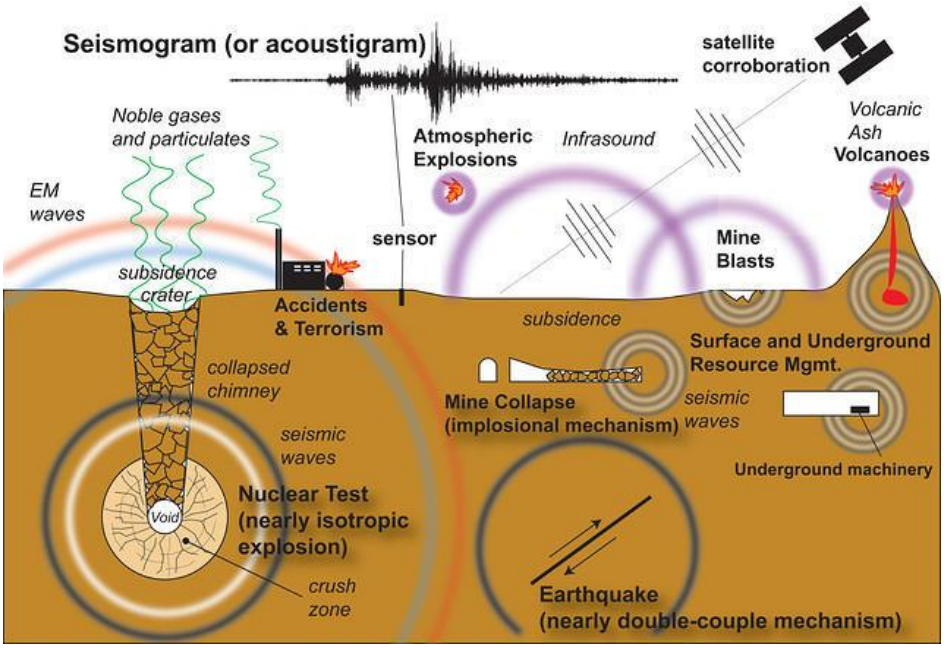

Figure 1.1 Schematic view of the seismological monitoring environment of the Earth. Human activity, waves of the ocean, volcanic, tectonic and atmospheric processes continuously produce perpetual elastic vibrations within the Earth that are detected with seismic sensor networks. (Image courtesy of W. Walter and D. Harris, taken from www.iris.edu)

Moment Tensor catalogue, or Northern California Earthquake Data Center Moment Tensor catalogue). The Harvard CMT catalogue routinely provides moment tensors of earthquakes with magnitudes greater than 5 that occur anywhere in the world. The regional and local moment tensor catalogues include moment tensors of earthquakes with significantly smaller magnitudes with threshold values depending on the sensitivity of the respective seismic network.

Various methods have been developed for inverting waveform recordings for the moment tensor. The most common methods are the inversions using complete waveforms, amplitudes of direct waves or the amplitude ratios (Dziewonski & Woodhouse, 1983; Dziewonski et al., 2001; Jechumtálová & Šílený, 2005; Vavryčuk, 2007b; Sokos & Zahradnik, 2008). The moment tensor can be inverted using the absolute (Horálek et al., 2002; Minson & Dreger, 2008) or relative (Oncescu, 1986; Dahm, 1996; Andersen, 2001) methods and using the linear or non-linear inversion schemes (Kikuchi & Kanamori, 1991; Vavryčuk, 2001). The absolute moment tensor inversion approaches (Minson & Dreger, 2008; Cesca et al., 2013) are applied to individual earthquakes and usually require detailed information about the velocity model. The relative inversion methods are applied to a family of earthquakes with well-clustered hypocentres (Dahm, 1996) and should be less sensitive to the velocity model. The sensitivity to the velocity model is also suppressed if full waveforms are in the low-frequency range or if only amplitudes of direct waves are inverted (Dziewonski & Woodhouse, 1983; Dziewonski et al., 2001; Vavryčuk, 2007b).

The essential part of any moment tensor inversion is calculating the Green's functions. Depending on the complexity of the velocity model, we can use either discrete wavenumber or matrix methods for layered media (Bouchon & Coutant, 1994; Randall, 1994; Saikia, 1994), computationally demanding finite difference and spectral methods (Kelly et al., 1976; Vidale et al., 1985; Komatitsch & Tromp, 1999; Nissen-Meyer et al., 2007) or a computationally more effective seismic ray theory (Červený, 2001) which calculates the Green's function in the high frequency approximation.

Earthquakes are most commonly described by the double-couple (DC) moment tensor, which represents the force equivalent of shear faulting on a planar fault in isotropic media. The eigenvectors of the double-couple moment tensors inform us about the orientation of the fault and the direction of the slip vector. However, some studies reveal that seismic sources can also display more general moment tensors with significant non-double-couple (non-DC) components (Julian et al., 1998; Miller et al., 1998) indicating portions of volumetric strain (dilatation or compaction) in the faulting mechanism. The non-DC components can be source-related, being produced e.g. by the collapse of a cavity in mines (Rudajev & Šílený, 1985; Šílený & Milev, 2006); by shear faulting on a non-planar (curved or irregular) fault (Sipkin, 1986); by tensile faulting induced by fluid injection in geothermal or volcanic areas (Ross et al., 1996; Julian et al., 1997); or when the slip vector is inclined from the fault and causes its opening (Vavryčuk, 2001, 2011). Likewise, non-DC components can be produced by seismic anisotropy in the focal area (Vavryčuk, 2004, 2005; Rössler et al., 2007). On the other hand, the non-DC components can also be spurious, being generated by errors in the moment tensor inversion (Kravanja et al., 1999; Šílený, 2009). Here, not only errors in the location of the hypocentre or in the velocity model but also noise in observed waveforms or a sparse distribution of seismic stations on the focal sphere can produce 'artificial' non-DC components. Hence, distinguishing between the artificial and true non-DC components is usually not an easy task and every careful study of non-DC components should be preceded by synthetic tests to investigate the sensitivity of moment tensors to errors in the modelling procedure, given the setup and boundary conditions of the network recording the data (Panza & Saraò, 2000)

However, the seismic moment tensor is a basic quantity evaluated not only for earthquakes on all scales but also for acoustic emissions (AEs) generated during rock deformation experiments in the laboratory. Acoustic emissions as 'laboratory' earthquakes are an ideal tool to investigate not only the nucleation and migration of earthquakes in space and time under controlled boundary conditions but also to test, verify and optimize seismological methods such as the moment tensor inversion to better understand earthquake processes in detail addressing scaling-related objectives. Here, the opportunity to refine moment tensor inversion algorithms allows determination of high-precision moment tensors, which provide us with key information on the orientation of activated fractures, the fracture process itself and on properties of the material in the focal zone.

1.1 Motivation and Outline

Significant progress in seismic monitoring has been achieved in recent years, allowing datasets of an unprecedented quality to be acquired. At the same time improvements in moment tensor inversion techniques and increasing computer capacity allow determination of high-quality moment tensors necessary for the analysis of non-DC components. Based on these developments, this dissertations aims at presenting a comprehensive study of the resolution capability and interpretation of non-DC components of moment tensors of seismic sources covering different fault dimensions extending from 10^{-6} m² (laboratory earthquakes) to 10^{6} m² (M~4 earthquakes) using high-quality data and refining state of the art moment tensor inversion techniques. Analysing earthquakes over a wide range of scales extending from microseismicity to large earthquakes is of high interest for a systematic analysis of non-DC components and different aspects of the analysis of non-DC components can be highlighted. Laboratory earthquakes are an ideal tool for studying the occurrence of

non-DC components under controlled boundary conditions. This knowledge can be used for finding the origin and for interpreting the non-DC components of earthquakes observed in the field. The main goal and motivation of this study is to

- substantially contribute to the long-standing and ongoing debate related to the significance, origin and physical interpretation of non-DC components in seismic moment tensors of different types of earthquakes.
- refine existing inversion algorithms. For example to constrain the moment tensor inversion to physically reasonable source models or to simultaneously invert for the seismic moment tensor and other parameters of the medium.
- argue for the role of crustal fluids and seismic anisotropy in the focal zone for generating non-DC components in earthquakes.
- bridge the gap between geophysical field studies (where seismic monitoring serves as a tool to monitor rupture processes under fixed boundary conditions) and laboratory experiments (where boundary conditions such as confining pressure, fluid content and composition can be controlled and optimized) with the perspective to design future experiments in the laboratory simulating specific aspects of the earthquake rupture process.

To address these topics two datasets containing seismicity on different scales have been analysed. First, the aftershock sequence of the 1999 M_w7.4 Izmit earthquake representing earthquake with magnitudes ranging from two to four was studied. A 35-station seismic network covering the entire rupture was completed only four days after the main shock allowing a data set of the Izmit and Düzce aftershock activity to be acquired that is supposed to be one of the best in the world. Here, two peer-reviewed manuscripts have been published in the *Geophysical Journal International* (Chapter 3 and 4). Second, AE recordings from a triaxial loading rock deformation experiment in the laboratory representing magnitudes ranging from -4 to -6 were analysed. A manuscript has recently been submitted to the *Geophysical Journal International* (Chapter 5). These works are hereinafter referred to as chapters, which are briefly introduced in the following:

Chapter 2 provides the basic theory of moment tensors. The definition and decomposition of the moment tensor, the inversion for the moment tensor, and the principles of the shear-tensile source model are briefly introduced. Theory and methods are not discussed in detail since a theoretical and methodological introduction to the specific topics is included in each of the following chapters.

Chapter 3 presents extensive synthetic tests on the resolution of non-DC components of aftershock recordings of the 1999 M_w = 7.4 Izmit earthquake. First a synthetic dataset was compiled to mimic seismic observations of aftershocks of the Izmit earthquake. Uncertainties are simulated by incorporating errors in the velocity model and hypocentre locations. Synthetic amplitudes are further contaminated with noise to analyse the resolution capability of the given network. In addition, two different inversion approaches - a linear full moment tensor inversion and a nonlinear moment tensor inversion constrained to a shear-tensile source model - were tested. The results of this chapter are of great interest when aiming to detect potential non-DC components by a regional seismic network. Furthermore, the results are essential for the interpretation of the non-DC components of aftershock recordings of the 1999 Izmit earthquake presented in the following chapter.

Chapter 4 focuses on the application of the refined moment tensor inversion algorithm, presented in the previous chapter, to aftershock recordings of the 1999 Izmit earthquake to retrieve high precision moment tensors. To ensure high-quality data, strict selection criteria were applied to the earthquake catalogue. The selection reduces the number of events from more than 4000 to only 33 events. Finally, the non-DC components were determined for the retrieved moment tensors taking into consideration the error bounds retrieved in Chapter 3. A comprehensive interpretation of the non-DC components and a discussion of their physical origin considering the tectonic settings form the main part of this chapter.

In **Chapter 5** advanced moment tensor inversion techniques are applied to AE recordings in laboratory rock deformation experiments. In this study, a new approach to moment tensor inversion in anisotropic and attenuating media is tested and applied to AEs produced by a differential loading of a granite sample. In this experiment, the velocity model is anisotropic, attenuating and time dependent due to the opening or closure of microcracks in the sample caused by loading. It is therefore inevitable to consider the time-dependency and anisotropy of the velocity model as well as the attenuation of waves for the moment tensor inversion. Here, a new algorithm for moment tensor inversion considering these aspects is presented and tested. The sensitivity of moment tensors to the P-wave anisotropy and attenuation is investigated. Moreover, it is demonstrated that the moment tensor inversion applied to a large dataset of AEs can be utilized to provide information on the attenuation parameters of the rock sample. The resolution of the method is even high enough to distinguish anisotropic attenuation of P waves.

Chapter 6 summarizes the main findings of the studies presented in this thesis and concludes with a joint interpretation and discussion of the results. It indicates implications of the findings and considers suggestions for further research.

2 Moment Tensors: Theory

2.1 The Representation Theorem

The elastodynamic equation of motion describes the generation of elastic waves due to a sudden change of stress in a medium. It takes the following form in elastic, inhomogeneous, unbounded and anisotropic media (Aki & Richards, 2002):

$$\rho \frac{\partial^2 u_i}{\partial t^2} - \frac{\partial}{\partial x_j}\left(c_{ijkl} \frac{\partial u_k}{\partial x_l}\right) = f_i \quad i = 1,2,3 \tag{2.1}$$

where u_i is the ith component of the displacement vector $\mathbf{u}$ generated by the ith component of the body force $\mathbf{f}$, ρ is the density of the medium and c_{ijkl} is the fourth order elasticity tensor containing the elastic coefficients of the medium surrounding the source. Here, only internal forces are considered. The simplest body force is a unidirectional unit impulse acting at one point (point source) and acting at instantaneous time. The response of the medium at position $\mathbf{x}$ and time t to the point source applied at position $\boldsymbol{\xi}$ and instant time τ acting in the direction x_n is described by the elastodynamic second-order Green's tensor $G_{in}(\mathbf{x},t,\boldsymbol{\xi},\tau)$. Equation 2.1 reads then:

$$\rho \frac{\partial^2 G_{in}}{\partial t^2} - \frac{\partial}{\partial x_j}\left(c_{ijkl} \frac{\partial G_{kn}}{\partial x_l}\right) = \delta_{in}\delta(\mathbf{x} - \boldsymbol{\xi})\delta(t - \tau) \quad i, n = 1,2,3 \tag{2.2}$$

where δ_{in} is the Kronecker delta and $\delta(t)$ is the Dirac delta function. Considering equations 2.1 and 2.2 the observed displacement field $\mathbf{u}$ at position $\mathbf{x}$ and time t caused by the internal force $\mathbf{f}$ at point $\boldsymbol{\xi}$ and time τ is expressed as a convolution of the Green's function G_{in} and the body force f_n over space and time (Aki & Richards, 2002):

$$u_i(x,t) = f_n * G_{in} = \int_{-\infty}^{\infty} \iiint_V f_n(\boldsymbol{\xi},\tau) G_{in}(\boldsymbol{x},t,\boldsymbol{\xi},\tau) d\tau dV(\boldsymbol{\xi}) \tag{2.3}$$

Equation 2.3 is called the general representation theorem. As the name suggests equation 2.3 is general and the source must be specified for seismological applications. The most common approach to describe seismic sources is the approximation by a model of dipole forces acting along a fault plane Σ (Figure 2.1):

$$f_n(\boldsymbol{\xi},\tau) = -m_{nk} \frac{\partial \delta(\Sigma)}{\partial \xi_k}, \tag{2.4}$$

where $\delta(\Sigma)$ is the Dirac delta function defined along the fault surface, and m_{nk} is called the seismic moment density tensor (Aki & Richards, 2002):

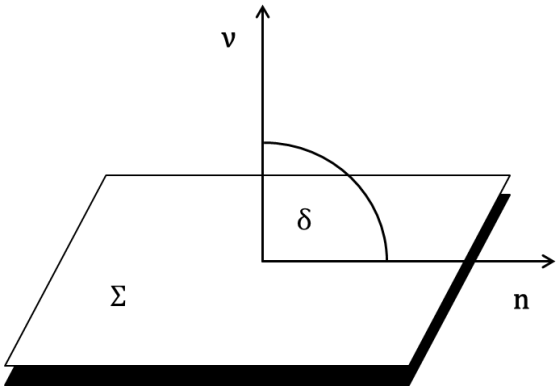

Figure 2.1: Geometry of a dislocation source described by the fault normal $\boldsymbol{\nu}$ and the slip vector $\mathbf{u}=u\mathbf{n}$, where $\mathbf{n}$ is the slip direction vector. For shear sources, the slip vector $\mathbf{u}$ lies within the fault surface Σ and the inclination angle δ is 90°. For tensile sources, δ is less than 90°, and for compressional sources, δ is greater than 90°.

$$m_{nk} = c_{ijnk}[u_i]\nu_j, \tag{2.5}$$

where $[u_i] = u_i^+ - u_i^-$ is the *i*th component of the displacement discontinuity along the fault and ν_j is the *j*th component of the fault normal. Moment density m_{nk} has the dimension of the moment per unit area. The moment tensor M_{nk} is defined as the integral of moment densities m_{nk} over Σ:

$$M_{nk} = \iint_{\Sigma} c_{ijnk}[u_i]\nu_j d\Sigma = \iint_{\Sigma} m_{nk} d\Sigma \tag{2.6}$$

and consequently the moment density tensor can be derived from the moment tensor as follows:

$$m_{nk} = \frac{dM_{nk}}{d\Sigma}. \tag{2.7}$$

Substituting equation 2.4 into 2.3 yields:

$$u_i(\mathbf{x},t) = f_n * G_{in} = -m_{nk}\frac{\partial\delta(\Sigma)}{\partial\xi_k} * G_{in} = m_{nk} * \frac{\partial}{\xi_k}G_{in} = m_{nk} * G_{in'k} \tag{2.8}$$

where symbol '$*$' means the space-time convolution. In practice seismologists analyse waveforms containing periods, which are much greater than the extension of the source (Σ). Thus the contributions of the different surface elements can be considered to be in phase and the whole system is described by force couples acting at a point source, where the moment tensor M_{nk} equals the integral of moment densities m_{nk} over Σ. For an effective point source, equation 2.8 reads:

$$u_i(\mathbf{x},t) = M_{nk} * G_{in'k}\,, \tag{2.9}$$

where the convolution is over time only. It follows from the condition of the zero total angular momentum of the inner source that the seismic moment tensor is always symmetric

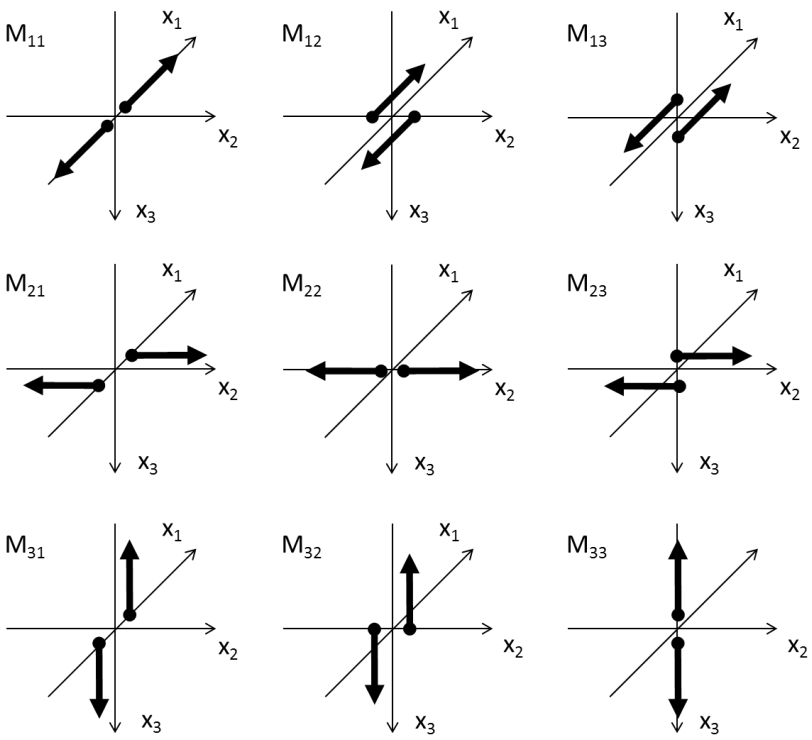

Figure 2.2: The nine possible force couples of the moment tensor that are required to obtain equivalent forces for a generally oriented displacement discontinuity (after Aki and Richards, 2002).

and is described therefore by six independent parameters. The moment tensor M_{nk} combines the force couples of a different orientation (Figure 2.2) and its moments thereby provide a general description of various seismic sources. Not only earthquakes but also explosions, implosions, rock falls, and mixed mode ruptures driven by fluid injection are described by the moment tensor. Thus, the concept of the moment tensors is quite general and flexible making moment tensor inversions an important tool in the seismic source characterization.

2.2 *Seismic Moment and Source Tensor*

In isotropic media, the interpretation of the moment tensor is straightforward in terms of the physical faulting parameters. But in anisotropic media it becomes complicated, since the moment tensor depends not only on the source parameters but also on the elastic parameters of the surrounding medium. Therefore, the density tensor is d_{kl} defined as follows (Vavryčuk, 2010a):

$$d_{kl} = \frac{1}{2}([n_k]v_l + [n_l]v_k), \qquad \textbf{2.10}$$

where d_{kl} describes the geometrical characteristics of the faulting process. Compared to the moment density tensor, the source density tensor is independent of the material properties in the focal zone. The source density tensor can be calculated directly from the moment density tensor

$$m_{ij} = c_{ijkl}d_{kl}. \qquad \textbf{2.11}$$

Assuming a point source in accordance with 2.6 the source tensor is determined by integrating the source density tensor over the fault surface Σ:

$$D_{kl} = \iint_{\Sigma} d_{kl} d\Sigma = \frac{u\Sigma}{2}(n_k \nu_l + n_l \nu_k), \tag{2.12}$$

where u is the average slip on the fault and Σ is the area of the fault. Accordingly, equation 2.11 simplifies as follows

$$M_{ij} = c_{ijkl} D_{kl}, \tag{2.13}$$

which is called the generalized Hooke's law in the source, because it resembles the relation between the stress and strain tensors described by the classical Hooke's law.

2.3 *Eigenvalues and Eigenvectors of the Source Tensor*

The source tensor is defined by the fault normal $\boldsymbol{\nu}$ and the direction of the slip vector $\mathbf{u}$ as follows.

$$\mathbf{D} = \frac{u\Sigma}{2}(\boldsymbol{n\nu} + \boldsymbol{\nu n}) = \frac{u\Sigma}{2}\begin{bmatrix} 2n_1\nu_1 & n_1\nu_2 + n_2\nu_1 & n_1\nu_3 + n_3\nu_1 \\ n_1\nu_2 + n_2\nu_1 & 2n_2\nu_2 & n_2\nu_3 + n_3\nu_2 \\ n_1\nu_3 + n_3\nu_1 & n_2\nu_3 + n_3\nu_2 & 2n_3\nu_3 \end{bmatrix} \tag{2.14}$$

It has the following diagonal form:

$$\mathbf{D}^{diag} = \frac{u\Sigma}{2}\begin{bmatrix} \mathbf{n}\cdot\boldsymbol{\nu} + 1 & 0 & 0 \\ 0 & 0 & 0 \\ 0 & 0 & \mathbf{n}\cdot\boldsymbol{\nu} - 1 \end{bmatrix} \tag{2.15}$$

where $\mathbf{u}\cdot\boldsymbol{\nu}$ denotes the scalar product. It follows that the maximum eigenvalue $d_1 = \frac{n_o\Sigma}{2}\,\mathbf{n}\cdot\boldsymbol{\nu} + 1$ is positive or zero and the minimum eigenvalue $d_3 = \frac{n_o\Sigma}{2}\,\mathbf{n}\cdot\boldsymbol{\nu} - 1$ is negative or zero. The corresponding eigenvectors are:

$$\mathbf{e}_1 = \frac{\mathbf{n}+\boldsymbol{\nu}}{|\mathbf{n}+\boldsymbol{\nu}|}, \quad \mathbf{e}_2 = \frac{\mathbf{n}\times\boldsymbol{\nu}}{|\mathbf{n}\times\boldsymbol{\nu}|}, \quad \mathbf{e}_3 = \frac{\mathbf{n}-\boldsymbol{\nu}}{|\mathbf{n}-\boldsymbol{\nu}|} \tag{2.16}$$

The symbol 'x' denotes the vector product. The angle between $\mathbf{n}$ and $\boldsymbol{\nu}$ is called the slip inclination $\boldsymbol{\delta}$ and can be derived directly from the eigenvalues of the source tensor**:**

$$\cos(\delta) = \frac{d_1 + d_3}{d_1 - d_3} \tag{2.17}$$

If we assume, for example, a pure shear source, $\mathbf{n}$ and $\boldsymbol{\nu}$ are perpendicular and the scalar product of both vectors is zero.

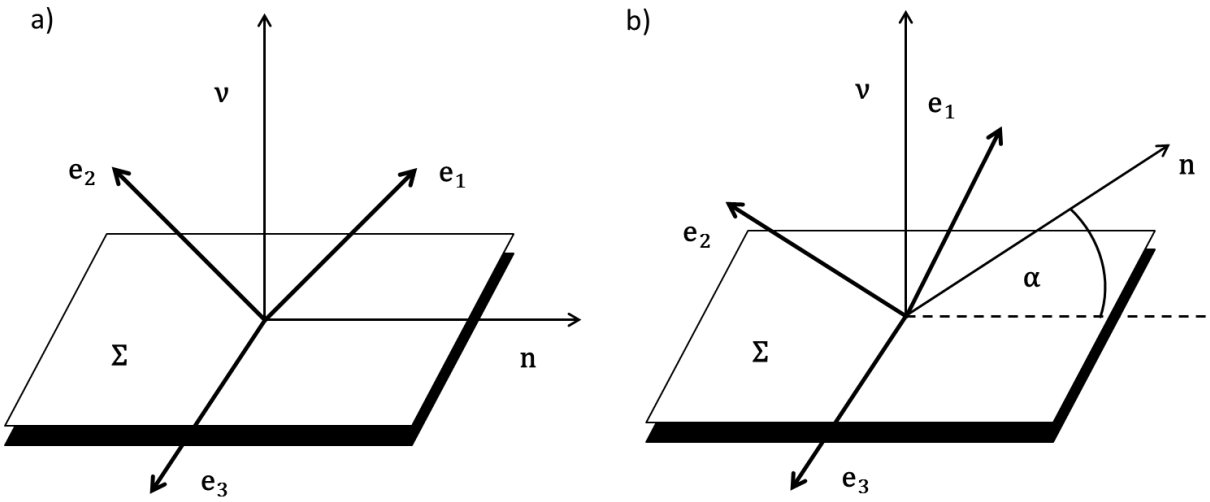

Figure 2.3: The shear source (a) and the tensile source (b) and its corresponding eigenvectors $\mathbf{e}_1$, $\mathbf{e}_2$, and $\mathbf{e}_3$. For both sources the fault normal $\boldsymbol{\nu}$ and the slip vector $\mathbf{n}$ span a plane, in which the eigenvectors $\mathbf{e}_1$ and $\mathbf{e}_2$ lie. For the shear source the angle between $\mathbf{e}_1$ and $\mathbf{n}$ and $\mathbf{e}_2$ and $\boldsymbol{\nu}$ is 45°, respectively. For a tensile source, where the slip vector deviates from the fault plane by an angle α, the angle between $\mathbf{e}_1$ and $\boldsymbol{\nu}$ is reduced to 45° - α/2 (modified after Vavryčuk, 2010a).

$$\mathbf{D}^{diag} = \frac{u\Sigma}{2}\begin{bmatrix}1 & 0 & 0\\ 0 & 0 & 0\\ 0 & 0 & -1\end{bmatrix} \qquad \textbf{2.18}$$

In this case, the eigenvector $\mathbf{e_1}$ and $\mathbf{e_2}$ lie in the plane spanned by $\mathbf{n}$ and $\boldsymbol{\nu}$ and both deviate by 45° (Figure 2.3a) from the eigenvectors. If the slip vector deviates from the fault surface by an angle α, also the eigenvectors are rotated accordingly (Figure 2.3b).

2.4 *Eigenvalues and Eigenvectors of the Moment Tensor*

The eigenvectors of the moment tensor define the coordinate system, in which the moment tensor diagonalizes. In isotropic media, they are denoted as $\mathbf{p}$, $\mathbf{t}$ and $\mathbf{b}$ and define the P, T and B axes. The P axis corresponds to the direction of the maximum compressional stress generated at the source and is derived from the minimum eigenvalue M_1. The T axis corresponds to the direction of the minimum compressional stress generated at the source and is derived from the maximum eigenvalue M_3. And lastly, the B axis corresponds to the direction of the intermediate stress at the source and is derived from the intermediate eigenvalue M_2. If the medium is isotropic, c_{ijkl} is described by only two elastic parameters, the Lame's parameters λ and μ:

$$c_{ijkl} = \lambda\delta_{ij}\delta_{kl} + \mu(\delta_{ik}\delta_{jl}+\delta_{il}\delta_{jk}). \qquad \textbf{2.19}$$

Equation 2.13 simplifies to

$$M_{ij} = \lambda D_{kk}\delta_{ij} + 2\mu D_{ij} \qquad \textbf{2.20}$$

and the moment tensor reduces to

$$\mathbf{M}^{diag} = u\Sigma \begin{bmatrix} (\lambda+\mu)\mathbf{n}\cdot\boldsymbol{\nu}+\mu & 0 & 0 \\ 0 & \lambda\mathbf{n}\cdot\boldsymbol{\nu} & 0 \\ 0 & 0 & (\lambda+\mu)\mathbf{n}\cdot\boldsymbol{\nu}-\mu \end{bmatrix} \quad \textbf{2.21}$$

Here, the moment tensor and the source tensor have the same eigenvectors and the $\mathbf{p}$, $\mathbf{t}$ and $\mathbf{b}$ vectors can directly be inferred from the fault normal and the slip direction according to equation 2.16.

$$\mathbf{t} = \frac{\mathbf{n}+\boldsymbol{\nu}}{|\mathbf{n}+\boldsymbol{\nu}|}, \quad \mathbf{b} = \frac{\mathbf{n}\times\boldsymbol{\nu}}{|\mathbf{n}\times\boldsymbol{\nu}|}, \quad \mathbf{p} = \frac{\mathbf{n}-\boldsymbol{\nu}}{|\mathbf{n}-\boldsymbol{\nu}|} \quad \textbf{2.22}$$

However, in anisotropic media the eigenvectors of the moment tensor are generally different from that of the source tensor. It means physically that the direction of the slip does not necessarily correspond to the maximum shear stress on the fault, but may deviate from it. Since the directions of the eigenvectors are influenced by the elastic parameters in the source region, they cannot be related directly to the faulting parameters.

2.5 *Decomposition of the Moment Tensor*

The source parameters are determined by decomposing the moment tensor. The decomposition into the deviatoric part $\mathbf{M}^{dev}$ and the isotropic part $\mathbf{M}^{iso}$ is unique, where the isotropic part is

$$\mathbf{M}^{iso} = \frac{1}{3}Tr(\mathbf{M}) \begin{bmatrix} 1 & 0 & 0 \\ 0 & 1 & 0 \\ 0 & 0 & 1 \end{bmatrix}. \quad \textbf{2.23}$$

$Tr(\mathbf{M})$ is the trace of the moment tensor. Analogously, the deviatoric part is defined as

$$\mathbf{M}^{dev} = \begin{bmatrix} 1-Tr(\mathbf{M})/3 & 0 & 0 \\ 0 & 1-Tr(\mathbf{M})/3 & 0 \\ 0 & 0 & 1-Tr(\mathbf{M})/3 \end{bmatrix} \quad \textbf{2.24}$$

The further decomposition is ambiguous and can be performed in several ways (Vavryčuk, 2015b). For our purpose, we refer to the procedure proposed by Knophoff and Randall (1970), in which the deviatoric part of the moment tensor splits into the double couple $\mathbf{M}^{dc}$ and into the compensated linear vector dipole $\mathbf{M}^{clvd}$:

$$\mathbf{M}^{dc} = (1-2|\epsilon|)\mathbf{M}^{*}_{|\boldsymbol{max}|} \begin{bmatrix} -1 & 0 & 0 \\ 0 & 0 & 0 \\ 0 & 0 & 1 \end{bmatrix} \quad \textbf{2.25}$$

$$\mathbf{M}^{clvd} = |\epsilon|\mathbf{M}^{*}_{|\boldsymbol{max}|} \begin{bmatrix} -1 & 0 & 0 \\ 0 & -1 & 0 \\ 0 & 0 & 2 \end{bmatrix} \quad \textbf{2.26}$$

with

$$\epsilon = -\frac{\mathbf{M}^{*}_{|\boldsymbol{min}|}}{\left|\mathbf{M}^{*}_{|\boldsymbol{max}|}\right|}. \quad \textbf{2.27}$$

$\mathbf{M}^*_{|min|}$ and $\mathbf{M}^*_{|max|}$ are the minimum and maximum eigenvalues of the deviatoric moment tensor, respectively. Components $\mathbf{M}^{dc}$ and $\mathbf{M}^{clvd}$ share the same P and T axes (Julian et al., 1998). For the interpretation, the moment tensor components $\mathbf{M}^{iso}$, $\mathbf{M}^{dc}$ and $\mathbf{M}^{clvd}$ are normalized to express their relative amount in the complete moment tensor. This work follows the convention proposed by Vavryčuk (2002), where the contributions are expressed in percentages as follows:

$$\mathrm{ISO} = \frac{1}{3}\frac{Tr(\mathbf{M})}{\left|M_{|max|}\right|} \cdot 100\% \qquad \textbf{2.28}$$

$$\mathrm{CLVD} = -2\epsilon(100\% - |\mathrm{ISO}|)$$

$$\mathrm{DC} = 100\% - |\mathrm{ISO}| - |\mathrm{CLVD}|$$

with |ISO|+|CLVD|+DC=100%. In isotropic media, the signs of the non-DC components, ISO and CLVD, define the type of the source. When both have a positive sign, the source is tensile (e.g. an opening crack), and when both have a negative sign, the source is compressive (e.g. a closing crack). The DC component is always positive. In isotropic media, a pure shear event, where the slip vector lies within the fault plane, produces a DC component of 100%. Since shearing in isotropic media is explained by two conjugated force couples, shear faulting on two 'conjugated' faults yields the same moment tensors. This ambiguity is inherent and can be removed using some additional information. For example tectonic settings derived from aftershock distributions can help to identify the rupture plane.

2.6 Physical Interpretation of Non-DC Components

The list of possible origins for the CLVD and ISO components is long, e.g. volumetric changes in the source mechanism or anisotropy in the focal zone, and therefore the interpretation of both is difficult. However, while the DC component is related to pure shear faulting, the ISO component is physically associated to volumetric changes in the source. For example, the pure isotropic moment tensor with positive sign is equivalent to the radiation pattern of an

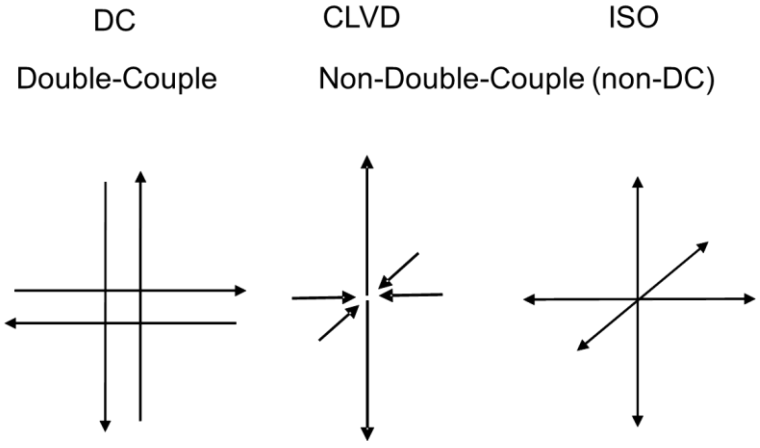

Figure 2.4: Body force equivalents of the DC, CLVD and ISO components. The DC component represents two force couples of equal size pointing in opposite direction. The ISO component is equivalent to the body forces of an explosion or implosion depending on the direction of the forces (pointing away from the source equals explosion and pointing to the source equals an implosion). The CLVD component consist of one large force couple and two smaller force couples pointing in the other direction with respect to the source.

explosion (Figure 2.4). While the ISO component is well explained by explosions and implosions depending on the sign, the interpretation of the CLVD is not straightforward. For example, faulting on a non-planar fault or the simultaneous activation of two differently oriented nearby faults can produce significant CLVD components (Frohlich et al., 1989; Kawakatsu, 1991). Another origin of the CLVD component is shear faulting in anisotropic media (Rössler et al., 2007; Vavryčuk, 2007b). In this case, it is important to substitute the decomposition of the moment tensor by that of the source tensor, if the elastic parameters are known. Similar observations are made for shear faulting in heterogeneous media. Furthermore rapid polymorphic phase changes can also produce significant non-DC components. In fact, the CLVD force system was invented by Knopoff and Randall (1970) to describe deep-focus earthquakes caused by phase transformations.

Both non-DC components, ISO and CLVD, can have several origins. For crustal earthquakes a positive sign in the non-DC component indicates a tensional component in the source mechanism. In geothermal or volcanically active areas, positive ISO and CLVD components are often observed and explained by opening cracks due to high pressure fluids, which is produced by a combination of shearing and opening of the fault (Panza & Saraò, 2000; Vavryčuk, 2002; Templeton & Dreger, 2006). Opening cracks might then be filled with fluid or magma. But pull-apart structures are also an environment that produces tensile fracturing with fluid playing an important role (Stierle et al., 2014a). Negative signs in the non-DC components indicate compressional components in the source mechanism. A prominent example is the cavity collapse in mines (Stickney & Sprenke, 1993). Lastly, non-DC components can also be produced, when single forces are present. For example, non-DC components are observed at landslides, volcanic eruptions or when an unsteady fluid flow occurs in volcanic channels.

The determination and interpretation of non-DC components is particularly difficult because the non-DC components can also be generated by errors in the modelling procedure. Beside the errors in the velocity model and an inaccurate location of an earthquake, a sparse distribution of stations on the focal sphere and noise in data also produce so-called ‘artificial’ non-DC components. Furthermore, a simplified source model can generate the non-DC components. Therefore, it is important to carefully interpret the retrieved non-DC components and a detailed analysis of uncertainties of the non-DC is essential. For example, extensive synthetic tests on the sensitivity of the non-DC components for the specific setup (network geometry, distribution and characteristics of seismicity, data quality, etc.) can define a confidence level above which the retrieved non-DC components can be considered as statistically significant (Panza & Saraò, 2000). Such tests reduce misinterpretations and contribute to a profound analysis of the non-DC components.

2.7 Moment Tensor Inversion

Several alternative methods have been developed for inverting moment tensors. Some invert full waveforms, while other concentrate on specific body wave phases such as the P and S waves. Depending on the quantity and quality of input data, either the full moment tensor can be obtained or only its part. For example, constraining the inversion to the deviatoric part reduces the number of unknown parameters and thus stabilizes the problem. The moment tensor can also be constrained to the double-couple moment tensor or to a moment tensor describing a shear-tensile source. In this case, the inversion scheme is non-linear and iterative procedures or a grid search must be used to solve it.

In the framework of this thesis, the inversion of P and S wave amplitudes is performed and the basic algorithm is written by Vavryčuk (2010b). When using amplitudes of waves, the problem is simplified by neglecting the source-time function in equation 2.9 and the convolution reduces to a multiplication. The representation theorem in equation 2.9 can be written in matrix form:

$$\mathbf{d} = \mathbf{G}\mathbf{m}, \tag{2.29}$$

where **d** is the vector containing *N* amplitudes, **G** is the Green's matrix of the dimension 3Nx6 containing the spatial derivatives of the Green's tensor, and **m** is the seismic moment vector containing the 6 independent parameters of the moment tensor (Vavryčuk, 2010a). Equation 2.29 can be written in an explicit form as follows:

$$\begin{bmatrix} u_1^{(1)} \\ u_2^{(1)} \\ u_3^{(1)} \\ \vdots \\ u_1^{(N)} \\ u_2^{(N)} \\ u_3^{(N)} \end{bmatrix} = \begin{bmatrix} G_{11}^{(1)} & G_{12}^{(1)} & G_{13}^{(1)} & G_{14}^{(1)} & G_{15}^{(1)} & G_{16}^{(1)} \\ G_{21}^{(1)} & G_{22}^{(1)} & G_{23}^{(1)} & G_{24}^{(1)} & G_{25}^{(1)} & G_{26}^{(1)} \\ G_{31}^{(1)} & G_{32}^{(1)} & G_{33}^{(1)} & G_{34}^{(1)} & G_{35}^{(1)} & G_{36}^{(1)} \\ \vdots & \vdots & \vdots & \vdots & \vdots & \vdots \\ G_{11}^{(N)} & G_{12}^{(N)} & G_{13}^{(N)} & G_{14}^{(N)} & G_{15}^{(N)} & G_{16}^{(N)} \\ G_{21}^{(N)} & G_{22}^{(N)} & G_{23}^{(N)} & G_{24}^{(N)} & G_{25}^{(N)} & G_{26}^{(N)} \\ G_{31}^{(N)} & G_{32}^{(N)} & G_{33}^{(N)} & G_{34}^{(N)} & G_{35}^{(N)} & G_{36}^{(N)} \end{bmatrix} . \begin{bmatrix} M_{11} \\ M_{22} \\ M_{33} \\ M_{23} \\ M_{13} \\ M_{12} \end{bmatrix} \tag{2.30}$$

Consequently, the resultant moment tensor is obtained from equation 2.30

$$\mathbf{m} = \mathbf{G}^{-1}\mathbf{d}\,. \tag{2.31}$$

Obviously, the problem must be overdetermined for equation 2.31 to be solvable. This means that we must have more observations than unknown parameters. In this case, the generalized inverse $\mathbf{G}^{-g}$ replaces $\mathbf{G}^{-1}$ with (Lay & Wallace, 1995)

$$\mathbf{G}^{-g} = [\mathbf{G}^T\mathbf{G}]^{-1}\mathbf{G}^T. \tag{2.32}$$

In practice, the input data are noisy and thus we need much more than 6 amplitudes to resolve vector $\mathbf{m}$ accurately.

After obtaining the moment tensor, a stability analysis should be performed to verify the reliability of the solution. For example, a repeated inversion of amplitudes superimposed with artificial random noise can be performed. The stability of the inversion depends on several aspects. First, it depends on the distribution of stations on the focal sphere. Ideally, the epicentre should be located in the middle of the network so that the rays cover a broad area of the radiated wavefield. Consequently, a few stations covering a broad area of the radiation pattern produce more accurate results than when a high number of stations, which cover only a small part of the radiation pattern, are used in the inversion. Furthermore, a good signal to noise ratio is crucial. This ratio can be improved by filtering of the signal. The type of filter depends on the knowledge of the medium, the inversion method and on the instrument, which recorded the signal. The aim of filtering is to suppress noise and to reduce the sensitivity of the inversion to local (unknown) inhomogeneties in the

medium. Choosing the optimum parameters for filtering is a difficult task, since the frequency content of the seismic signal often overlaps with the frequency content of noise.

2.8 THE SHEAR-TENSILE SOURCE MODEL

The shear-tensile source model was introduced by Vavryčuk (2001). It generalizes the shear source by allowing the slip vector to deviate from the fault plane by an angle α (Figure 2.5). If an isotropic medium is assumed and the slip direction vector $\mathbf{n}$ and fault normal $\boldsymbol{\nu}$ are defined as follows

$$\boldsymbol{\nu} = \begin{bmatrix} 0 \\ 0 \\ 1 \end{bmatrix}, \quad \mathbf{n} = \begin{bmatrix} \cos(\alpha) \\ 0 \\ \sin(\alpha) \end{bmatrix} \tag{2.33}$$

the moment tensor takes the following form:

$$M = u\Sigma \begin{bmatrix} \lambda \sin\alpha & 0 & \mu \cos\alpha \\ 0 & \lambda \sin\alpha & 0 \\ \mu \cos\alpha & 0 & (\lambda + 2\mu) \sin\alpha \end{bmatrix} \tag{2.34}$$

with α ranging from -90° to 90°. The non-DC content of the moment tensor is controlled by slope α. For α=90°, the source is pure tensile and the DC component of the moment tensor equals zero. If the source is pure shear, α equals zero and the DC component of the moment tensor is 100%. The slope angle α can be derived from the moment tensor components in different ways (Vavryčuk, 2001). It can either be evaluated from the percentage of the DC, CLVD and ISO

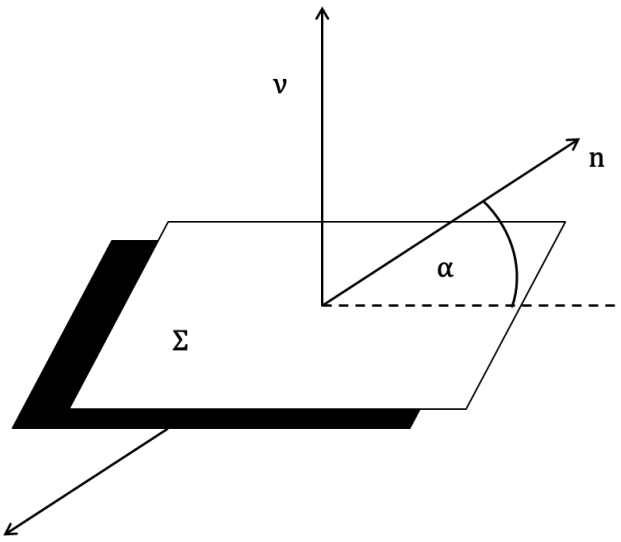

Figure 2.5: Geometry of the shear-tensile source model. The deviation of the slip direction vector $\mathbf{n}$ from the fault plane Σ is described by the angle α.

$$\alpha^{iso} = sign(ISO)arcsin\frac{|ISO|}{\left(\kappa+\frac{2}{3}\right)(100\% - |ISO|) - \frac{1}{3}|ISO|} \quad \textbf{2.35}$$

$$\alpha^{clvd} = sign(CLVD)arcsin\frac{|CLVD|}{\frac{4}{3}100\% - |CLVD|(\kappa+1)} \quad \textbf{2.36}$$

$$\alpha^{dc} = sign(CLVD)arcsin\frac{100\% - DC}{100\% + DC(\kappa+1)} \quad \textbf{2.37}$$

or from the eigenvalues of the moment tensor

$$\alpha = arcsin\left(3\frac{M^*_{max} + M^*_{min}}{|M^*_{\max}| + |M^*_{min}|}\right). \quad \textbf{2.38}$$

All four formulas are equivalent, if the data are noise free. However, they behave differently, when noise is present. The slope angle α can be best determined from the DC component (equation 2.37), because the DC component rapidly decreases with increasing α. Even small angles α of only 20° can produce non-DC components up to 50%. Furthermore if the analysed data consist of events at the same focal zone characterized by similar ratios of the Lames parameters denoted as

$$\kappa = \frac{\lambda}{\mu}, \quad \textbf{2.39}$$

equations 2.36, 2.37 and 2.38 are less sensitive to noise, since they utilizes additional information on κ. Note that κ is defined for a medium in the close vicinity of the fault only. Since a fault describes a zone of weakness, the rheological parameters of the fault differ from that of the surrounding medium. Therefore, κ cannot be compared to standard λ/μ ratios derived for the surrounding medium. However, the shear-tensile source model also allows κ to be resolvable either via the eigenvalues

$$\kappa = \frac{2}{3}\left(\frac{Tr(M)/3}{M^*_{max} + M^*_{min}} - 1\right) \quad \textbf{2.40}$$

or using the percentage of the ISO and CLVD

$$\kappa = \frac{4}{3}\left(\frac{ISO}{CLVD} - \frac{1}{2}\right) \quad \textbf{2.41}$$

Parameter κ is very important for detailed studies of physical conditions of a material along a fault and in its close vicinity.

3 Resolution of Non-Double-Couple Components in The Seismic Moment Tensor using Regional Networks: 1. A Synthetic Case Study[1]

SUMMARY

We perform a detailed synthetic study on the resolution of non-double-couple (non-DC) components in the seismic moment tensors from short-period data observed at regional networks designed typically for monitoring aftershock sequences of large earthquakes. In addition, we test two different inversion approaches - a linear full moment tensor inversion and a nonlinear moment tensor inversion constrained to a shear-tensile source model. The inversions are applied to synthetic first-motion P- and S-wave amplitudes, which mimic seismic observations of aftershocks of the 1999 M_w = 7.4 Izmit earthquake in north western Turkey adopting a shear-tensile source model. To analyse the resolution capability for the obtained non-DC components inverted, we contaminate synthetic amplitudes with random noise and incorporate realistic uncertainties in the velocity model as well as in the hypocentre locations. We find that the constrained moment tensor inversion yields significantly smaller errors in the non-DC components than the full moment tensor inversion. In particular, the errors in the compensated linear vector dipole (CLVD) component are reduced if the constrained inversion is applied. Furthermore, we show that including the S-wave amplitudes in addition to P-wave amplitudes into the inversion helps to obtain reliable non-DC components. For the studied station configurations, the resolution remains limited due to the lack of stations with epicentral distances less than 15 km. Assuming realistic noise in waveform data and uncertainties in the velocity model, the errors in the non-DC components are as high as ±15 per cent for the isotropic and CLVD components, respectively, thus being non-negligible in most applications. However, the orientation of P- and T-axes is well determined even when errors in the modelling procedure are high.

[1] This article has been published in the Geophysical Journal International: E. Stierle, V. Vavryčuk, J. Šílený, and M. Bohnhoff (2014). Resolution of Non-Double-Couple Components in The Seismic Moment Tensor using Regional Networks: 1. A Synthetic Case Study. 196(3), 1869-1877, doi: 10.1093/gji/ggt502. Published by Oxford University Press on behalf of The Royal Astronomical Society and Deutsche Geophysikalische Gesellschaft.

3.1 INTRODUCTION

Recent progress in seismic monitoring technology resulted in waveform recordings allowing detailed studies on the earthquake rupture process. In that respect, one of the key objectives is to resolve reliable non-shear components in the seismic moment tensors and to assess their resolution. Since it is known that brittle damage is expected to produce generically some tensile component of faulting (Ben-Zion & Ampuero, 2009), the approximation of a shear slip on a planar fault, represented by a double-couple (DC) source model, seems to be too simple for some types of seismicity such as volcanic or geothermal earthquakes. Earthquake rupture processes might involve significant amounts of non-DC components, such as tensional components in the source mechanism (Frohlich, 1994; Julian et al., 1998; Miller et al., 1998; Horálek et al., 2002; Minson et al., 2007; Rössler et al., 2007). However, observed non-DC components can also be artificial reflecting errors in the modelling procedure, seismic noise or a lack of data, for example, due to sparse distribution of stations on the focal sphere (Kravanja et al., 1999). In this respect, one principal but yet less addressed objective is estimating the accuracy and reliability of the source related non-DC components of retrieved seismic moment tensors. Specifically it is important to know, if and how accurately the non-DC components can be resolved for a given station configuration under certain conditions, such as seismic noise level and inaccurate information on the velocity structure. Therefore, it is desirable to quantify a confidence level above which non-DC components can be considered to be statistically significant prior to any analysis of field observations (Panza & Saraò, 2000).

Synthetic resolution studies of non-DC components have been published in several papers. For example, Vavryčuk (2007b) studied numerically the errors in the non-DC mechanisms for microearthquakes from synthetic borehole data with various configurations of boreholes, and Šílený (2009) performed a synthetic case study testing the resolution capability of non-DC mechanisms for microearthquakes at a station configuration simulating the geothermal site at Soultz-sous-Forets, France. The latter author showed that even low non-DC components were well resolved not being masked by spurious non-DC components when P- and S-wave amplitudes are inverted for the full moment tensor.

In contrast to previous studies dealing with microseismicity observed at local networks (<10 km), we focus on the resolution capability of regional networks (aperture ~220 km) with configurations designed typically for monitoring aftershock sequences of large (M > 7) earthquakes. In addition, we test two different moment tensor inversion techniques: First, we perform a standard linear inversion for the full moment tensor, and secondly, a non-linear moment tensor inversion constrained to a shear-tensile (also called tensile or dislocation) source model is used. Here, we have to emphasize that the latter method is only applicable to real observations, provided the data are consistent with the shear-tensile source model (Vavryčuk, 2001, 2011; Minson et al., 2007). The consistency of this model can be verified, for example, by evaluating the consistency factor proposed by Vavryčuk (2011), his equation 23). However, for both methods we test two different sets of input data: P- and S-wave amplitudes or P-wave amplitudes only. As a case study we simulate seismic observations of aftershocks of the 1999 Mw = 7.4 Izmit earthquake in north western Turkey and determine the resolution limits for their non-DC components. We model synthetic seismic recordings of aftershocks adopting several source types of shear-tensile faulting (Vavryčuk, 2001). To simulate real data, we contaminate the synthetic waveforms with random noise. We also use inaccurate hypocentre locations and velocity models when determining the Green's functions needed for the inversion. Finally, we investigate the

resolution of source related non-DC components in dependence of the linear and non-linear inversion approach as well as the input data P- and S-wave amplitudes. The application to real observations is presented in a companion paper (Stierle et al., 2014a).

3.2 Setup of the Experiment and Methods

As an example of regional network data, we adopt observations of aftershocks of the 1999 Mw = 7.4 Izmit earthquake. The Izmit earthquake ruptured a ~140 km long segment of the North Anatolian Fault Zone (NAFZ hereafter) in NW Turkey (Tibi et al., 2001; Barka et al., 2002). To monitor its aftershock activity, a network of 35 three-component short-period seismic stations (Figure 3.1) was completed within 4 days after the main shock covering the entire rupture (Baumbach et al., 2003). The aperture of the network is about 220 km and seismicity mainly occurred in a depth range between 6 and 16 km (Bulut et al., 2007). Aftershock focal mechanisms around the Izmit epicentre and at the eastern part of the rupture indicate dominantly strike-slip motions with some normal faulting components. In contrast, below the Akyazi Plain at the central part of the rupture, where a substantial slip deficit was accumulated during the main shock, events reflect purely EW-extensional normal faulting indicating a small pull-apart structure (Bohnhoff et al., 2006). This region can be seen as a potential area where significant non-DC components might exist.

For our synthetic case study, we choose three different hypocentres (1–3) with a focal depth of 11 km, representing spots of pronounced Izmit aftershock activity and located close to the main fault along the rupture (Figure 3.1). Synthetic amplitudes are calculated adopting a shear-tensile source model (Vavryčuk, 2001; Figure 3.2), where slope angle α controls the non-DC content of the source mechanism (Table 3.1). For each hypocentre we modelled nine strike slip (strike = 0°, dip = 90°, rake = 180°) events and nine EW extensional normal faulting (strike = 0°, dip = 45°, rake = −90°) events with combined shear-tensile source mechanisms, where α is ranging from 0° to 20° (Table 3.1). In total, 54 events with different locations and focal mechanisms were simulated.

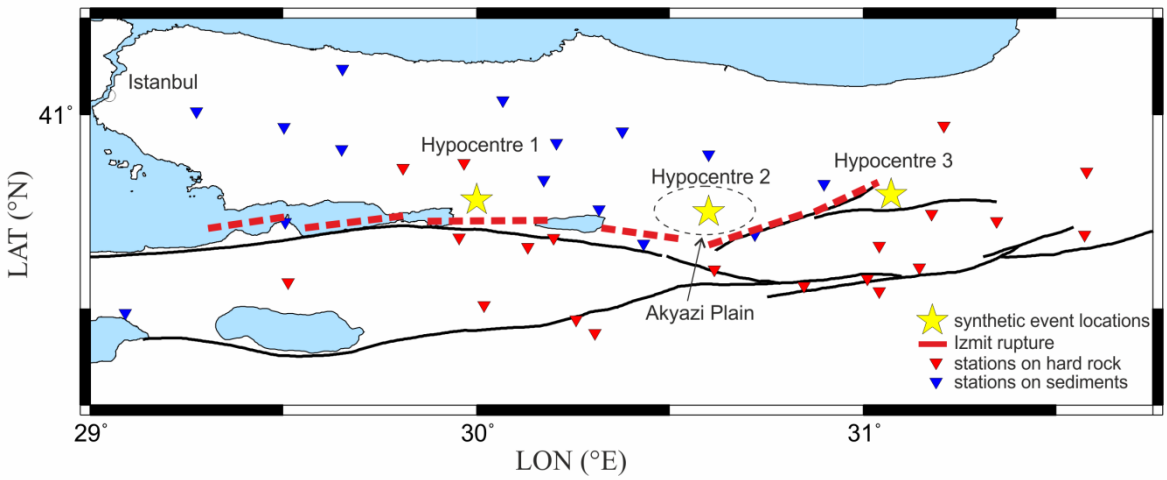

Figure 3.1: Configuration of stations of the seismic network deployed along the 1999 M_w = 7.4 rupture of the North Anatolian Fault Zone to monitor its aftershock activity (Baumbach et al., 2003). The stars mark the locations of the events considered in the synthetic tests. Red triangles represent stations on sediments and blue triangles represent stations on hard rock. Fault lines are taken from the Turkey General Directorate of Mineral Research and Exploration and red dashed lines are surface ruptures of the 1999 Izmit earthquake observed by Barka et al. (2002).

Alpha [°]	0	2.5	5	7.5	10	12.5	15	17.5	20
Non-DC [%]	0	12.1	22.2	30.9	38.5	44.6	50.1	54.8	60

Table 3.1: Percentages of the non-DC components in the seismic moment tensor of the shear-tensile source with varying slope α. The decomposition by Vavryčuk (2001) is used.

Bulut et al. (2007) presented a 1-D P-wave velocity model for the Izmit area derived from recordings of the aftershock sequence of the 1999 Izmit earthquake. Koulakov et al. (2010) further determined S-wave velocities as well as vP/vS ratios for the Izmit area using aftershocks of the Izmit earthquakes. Since stations are situated partly on hard rock and partly on a shallow sediment layer (Parolai et al., 2004), two different sets of path-specific 1-D velocity models are used for computing synthetic amplitudes: One set of velocity models representing stations situated on a shallow sediment layer and one set of velocity models for stations deployed on hard rock (Figure 3.3, red and black lines, respectively). The velocity models in each set vary within the first 5 km by ±15 per cent (see Figure 3.3).
Based on the 35-station seismic network, we selected a subset of 22 stations for each hypocentre representing a realistic number of stations recording an event of magnitude 3 (Figure 3.4). We find that all three coverages suffer from a rather poor distribution of stations at the centre of the focal sphere. In particular, near vertical directions are missing because of absence of stations at small epicentral distances (less than 15–20 km). This deficiency is inherent to all regional networks of a similar aperture being a compromise between demands on covering a large seismically active region and deploying a limited number of stations.

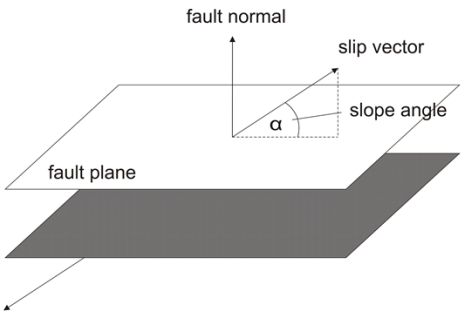

Figure 3.2: Shear-tensile source model. The non-DC content of the source mechanism is controlled by the slope angle α (α = 0° is for pure shear slip and α = 90° is tensile faulting).

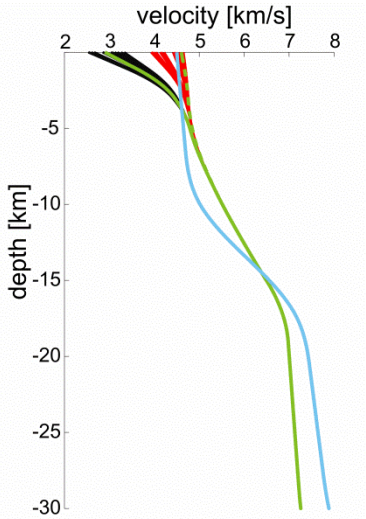

Figure 3.3: Smoothed velocity models used for the synthetic tests. Two different sets of velocity models were used for modelling synthetic amplitudes: with a shallow sediment layer (red lines) and without sediments (black lines). The models within one set differ from each other by approximately ±15 per cent within the first 5 km. Model 1 (green solid line), model 2 (green dashed line) and model 3 (blue solid line) were used for simulating errors in the velocity structure.

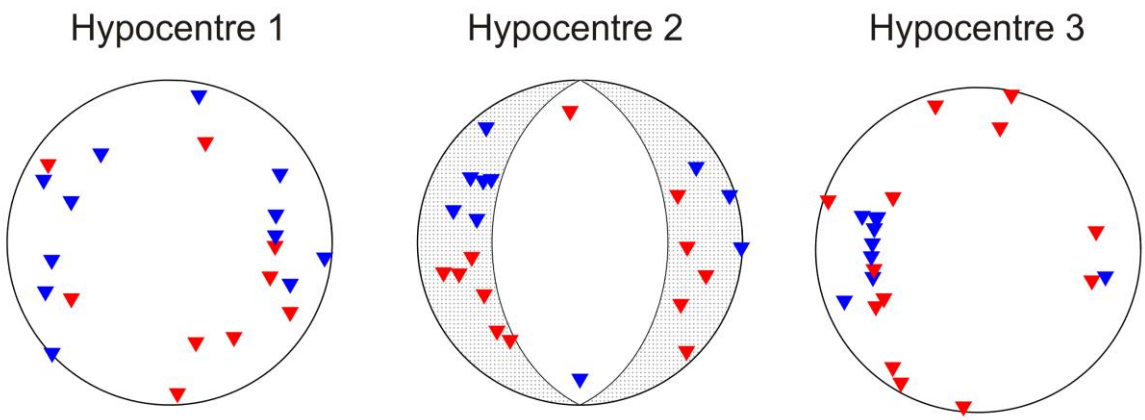

Figure 3.4: Station coverage on the focal sphere for a selected subset of 22 stations at the three hypocentres shown in Figure 3.1. Blue triangles are stations on sediments and red triangles are stations on hard rock. The focal sphere coverage is unfavourable for normal faulting mechanisms since the stations are located close to the nodal lines and therefore the P-wave amplitudes are small and more sensitive to errors.

Synthetic P- and S-wave amplitudes A_{syn} were calculated from prescribed moment tensor M and the spatial derivatives of the Green's function G using the representation theorem. Because we use a point-source approximation and invert amplitudes, the space-time convolution integral is reduced to a simple multiplication:

$$A_i^{syn} = M_{nk} \cdot G_{in,k}\,, \qquad 3.1$$

where subscript i is the sequential number of the station. As mentioned earlier, the moment tensor was determined adopting the shear-tensile source model after Vavryčuk (2001). To compute Green's functions, we used ray tracing techniques in a smoothed velocity model (Figure 3.3) after Červený (2001). The smoothed velocity model is necessary to ensure valid rays and to avoid caustic points, which produce artificially high amplitudes. The effect of the Earth's surface was incorporated in the Green's functions. Using ray tracing techniques, we obtained amplitudes corresponding to amplitudes of the direct P and S waves at each station of the network. For clarity, no waveform modelling is done and thus no picking of amplitudes was necessary for the synthetic tests.

After completing the pool of synthetic amplitudes, the full moment tensor inversion was performed. Prior to the inversion, amplitudes were weighted using two different scales. First, S-wave amplitudes were weighted by 0.5, because they are more difficult to pick and thus have higher uncertainties. Second, amplitudes measured at stations with epicentral distances smaller than 30 km were weighted by value of 1 and the remaining by value of 0.5. Since the signal at stations with large epicentral distance is usually weak and waves are more scattered and disturbed by noise and attenuation, picked amplitudes have generally less accuracy and are not as reliable as amplitudes at closer stations.

We introduce three different types of errors in the moment tensor inversion in order to analyse the sensitivity of non-DC components. First, the influence of uniformly distributed random noise was tested by a repeated inversion of amplitudes, where the noise level was station and distance dependent. In total, 100 realizations per event were performed. Second, the hypocentre was shifted by 2 km downwards and 2.5 km laterally with respect to its true position. These values represent the absolute location errors of the Izmit aftershocks (Bulut et al., 2007). Third, inaccuracies in the velocity model were introduced when computing Green's functions to simulate poor knowledge of the geological structure. By using only one model for stations on hard rock (model 2, Figure 3.3) and one

model for stations on sediments (model 1, Figure 3.3), we characterized low errors. To simulate higher errors in the velocity structure, we used one velocity model for all stations (model 3, Figure 3.3). The full moment tensor was determined by the generalized linear inversion (Lay & Wallace, 1995) of direct P- and S-wave amplitudes:

$$\mathbf{M} = \mathbf{G}^{-g}\mathbf{A} \text{ with } \mathbf{G}^{-g} = [\mathbf{G}^{T}\mathbf{G}]^{-1}\mathbf{G}^{T}, \tag{3.2}$$

where M is the full moment tensor, G is the matrix of spatial derivatives of the Green's function and A is the vector of observed amplitudes.

The moment tensor constrained to a shear-tensile source model was assessed via grid search by minimizing the L2 norm between observed and theoretical amplitudes. Using this approach the angles of the tensile source can directly be derived from the observed wavefield (Vavryčuk, 2011). Furthermore, the compensated linear vector dipole (CLVD) and isotropic (ISO) component are linearly dependent. They always have the same sign and their ratio is constant and depends on the vP/vS ratio in the source area (Vavryčuk, 2001, 2011):

$$\frac{\mathrm{ISO}}{\mathrm{CLVD}} = \frac{3}{4}\left(\frac{v_P}{v_S}\right)^2 - 1, \tag{3.3}$$

where ISO and CLVD mean the percentages calculated as follows

$$\mathrm{ISO} = \frac{1}{3}\frac{trace(\mathbf{M})}{\left|M_{|\max|}\right|}100\% \tag{3.4}$$

$$\mathrm{CLVD} = -2\frac{M^{*}_{|\min|}}{\left|M^{*}_{|\max|}\right|}\left[100\% - \left|\mathrm{ISO}\right|\right]. \tag{3.5}$$

Tensor M is the full moment tensor, and $M_{|\min|}$ and $M_{|\max|}$ are the eigenvalues of M with the minimum and maximum absolute value, respectively. Analogously, we define the eigenvalues for the deviatoric part M^{*} of the moment tensor M. Equation (3.3) implies that the errors of ISO and CLVD components are linked linearly and thus we obtain a similar accuracy for both.

Both inversions use ray tracing techniques in a smoothed velocity model and they incorporate calculation of ray-theoretical Green's functions (Červený, 2001). Basically, here we use the same procedure as for determining synthetic amplitudes. To assess the quality of the retrieved moment tensors, the normalized root-mean-square (RMS) error between theoretical and observed amplitudes is determined using the following formula:

$$RMS = \frac{\sqrt{\sum_{i=1}^{N}\left(A_i^{obs} - A_i^{theo}\right)^2}}{\sqrt{\sum_{i=1}^{N}\left(A_i^{obs}\right)^2}}, \tag{3.6}$$

where A_{obs} and A_{theo} are the observed and theoretical amplitudes, respectively, subscript i is the sequential number of the station and N is the total number of stations at which the amplitudes were recorded for the respective event. The decomposition of the moment

tensor into the percentage of the DC and non-DC components is performed after Vavryčuk (2001), where the non-DC component consists of a CLVD and an ISO component.

To analyse the accuracy of the retrieved source mechanisms and the resolution of the non-DC components, we use two criteria. First, theoretical and retrieved non-DC components are compared. Here, we analyse the absolute errors between retrieved and theoretical non-DC components. Therefore, a change in the polarity of ISO and CLVD components might appear as a minimum in the corresponding figure (for example, Figure 3.7, blue dashed line). Second, the deviation of P- and T-axes between the theoretical and retrieved DC mechanism is analysed to investigate the stability of the orientation of the fault plane. The angles between theoretical and retrieved P and T-axes are calculated using the scalar product of their direction vectors (e.g. Kagan, 1991).

3.3 Results of the Synthetic Experiment and Discussion

In the following, we discuss the results for Hypocentre 2 (Figure 3.1). Similar conclusions are drawn for Hypocentres 1 and 3 and obtained results for these are shown in the Appendix.

We started with contaminating the amplitudes with random noise. The noise level depends on the epicentral distance and was ranging from 10 to 25 per cent. It was further increased by 5 per cent for stations deployed on a sediment layer. The misfit of amplitudes measured by the RMS error was less than 0.15, which represents a good fit of amplitudes. Standard deviations for the ISO and CLVD components as well as the deviation of P- and T-axes are shown in Figure 3.5(a)–(c) for the inversion of P-wave amplitudes only and in Figure 3.6(a)–(c) for the inversion of P- and S-wave amplitudes. The orientation of the fault plane is well resolved in most cases regardless of the input data or type of inversion with deviations of P- and T-axes smaller than 8° (Figure 3.5c Figure 3.6c). Furthermore, we observe that errors in the ISO component are slightly higher for the full moment tensor inversion (∼2 per cent) than for the constrained inversion (∼1 per cent) when the P and S amplitudes are inverted. This difference is more significant for the inversion of only P-wave amplitudes, where the error is 7 per cent for the full moment tensor inversion and 3 per cent for the constrained inversion. Also the errors for the CLVD are about two to three times higher for the full moment tensor inversion of P- and S-wave amplitudes than for the constrained inversion. When inverting only P-wave amplitudes for the full moment tensor, the error in the CLVD component remarkably increases and it is as high as 30 per cent, whereas errors remain smaller than 10 per cent when the constrained inversion is applied. The observation that errors mainly affect the CLVD component in the full moment tensor inversion has been observed previously (Vavryčuk, 2011). The origin of such observation lies in the decomposition of the moment tensor into its CLVD and ISO percentages. The CLVD component is calculated from the ratio between the lowest and highest eigenvalues of the deviatoric moment tensor (see equation 3.4) and this non-linear relation makes the CLVD more sensitive to inaccuracies of the inverted moment tensor. In contrary, the relation between the ISO and the eigenvalues of the moment tensor is linear and therefore robust against the errors. Hence, the ISO component is, in general, less sensitive to errors in the modelling procedure and can be better resolved than the CLVD component. In the constrained inversion, however, the CLVD and ISO components are linearly dependent (Vavryčuk, 2001, 2011) and therefore the errors in the CLVD component are clearly reduced. Here, the error is about three times smaller than for the full moment tensor inversion.

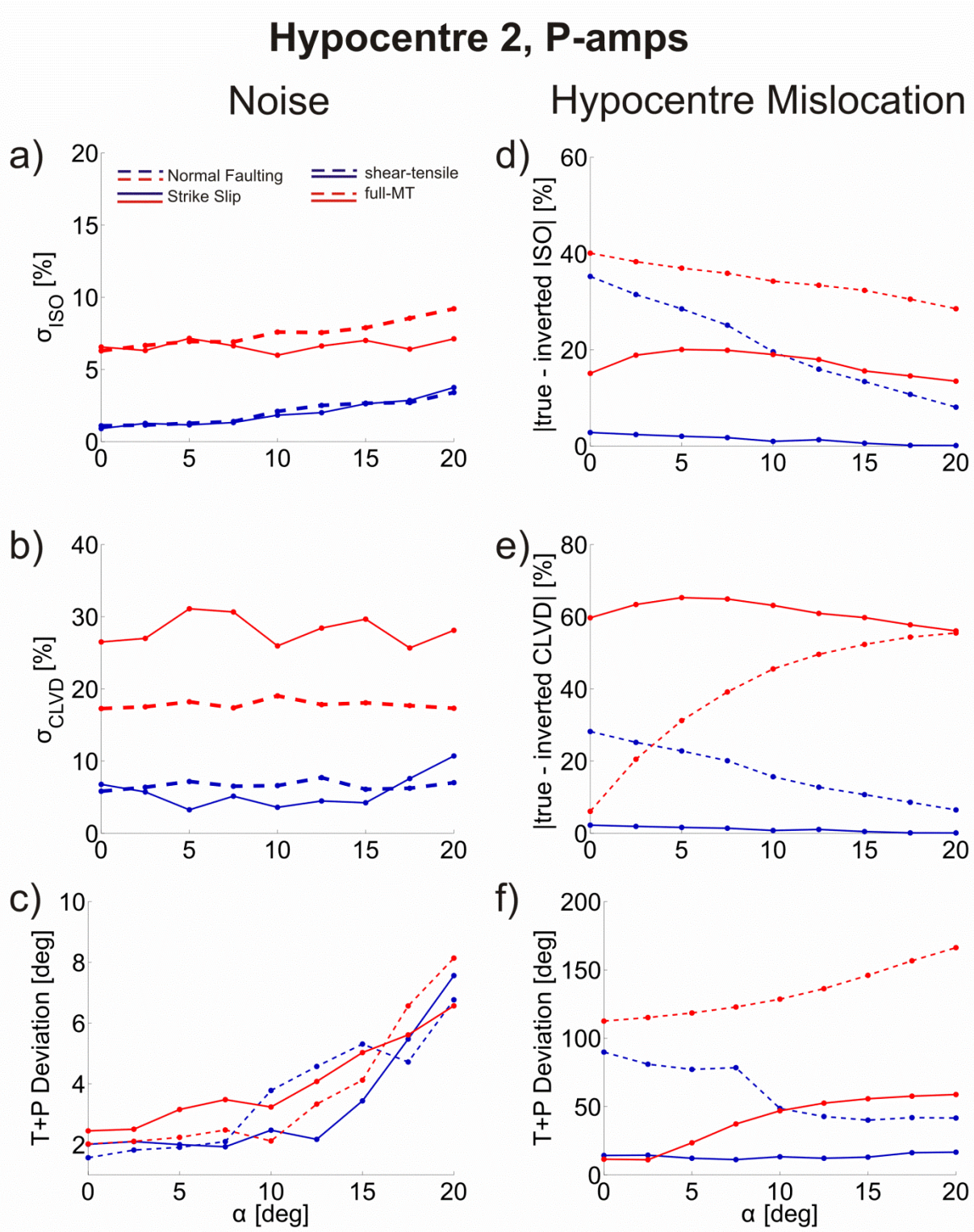

Figure 3.5: Moment tensor inversion for noisy amplitudes (left-hand side) and hypocentre mislocation (right-hand side) for the inversion of P-wave amplitudes only at Hypocentre 2. Errors are shown as a function of slope α. Red lines—the linear full moment tensor inversion, blue lines—the non-linear inversion constrained to a shear-tensile source model. We further distinguish between strike-slip mechanism (solid lines) and normal faulting mechanisms (dashed lines). Plots (a) and (b) show standard deviations of the ISO and CLVD components, respectively, determined from 100 inversions of noise contaminated amplitudes. Plots (d) and (e) present the difference between the retrieved and true percentages of ISO and CLVD components, respectively. The deviation between the retrieved and true P- and T-axes are displayed in plots (c) and (f).

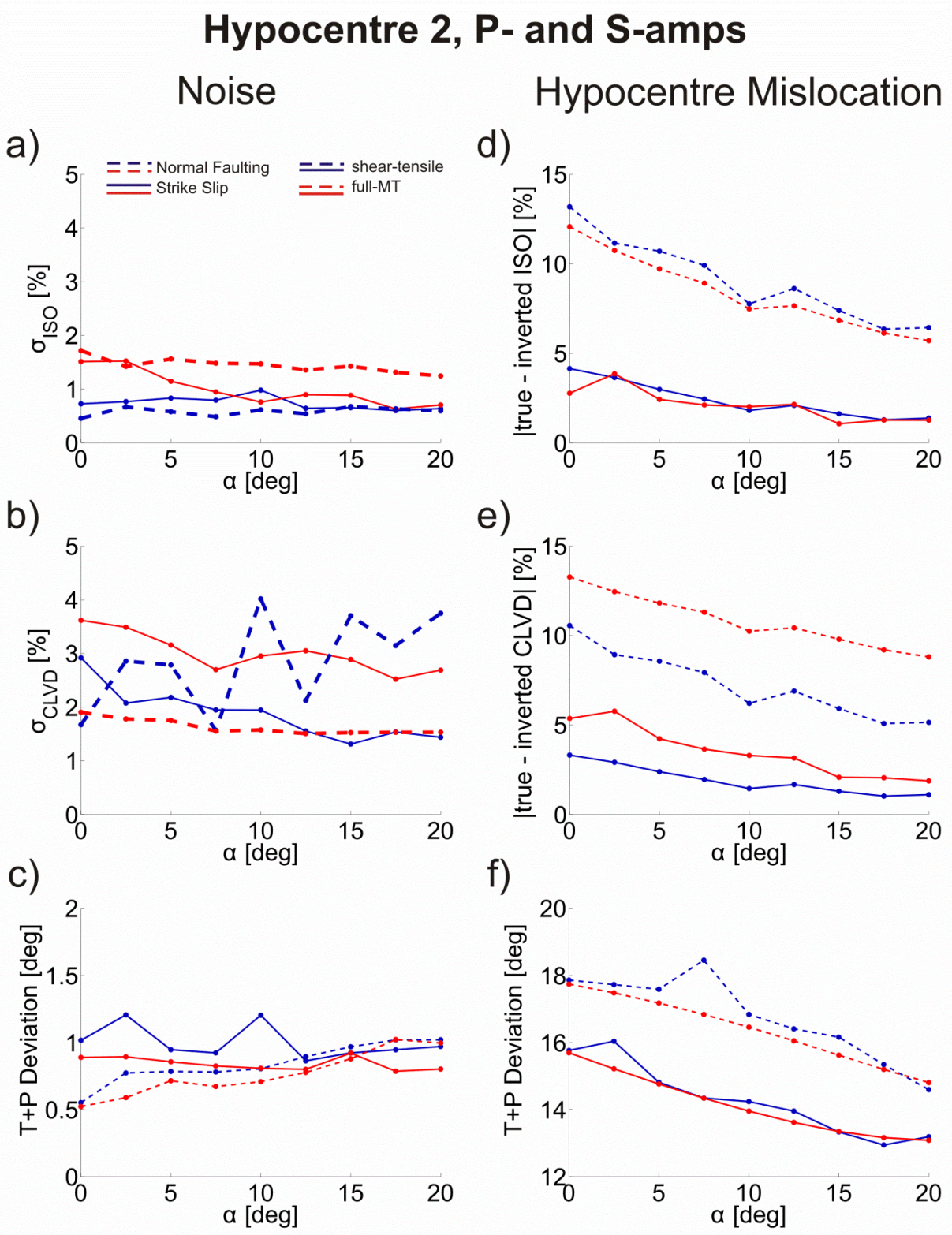

Figure 3.6: Moment tensor inversion for noisy amplitudes (left-hand side) and hypocentre mislocation (right-hand side) for the inversion of P- and S-wave amplitudes at Hypocentre 2. For details, see the caption of Figure 3.5.

Next, we incorporated errors in the hypocentre location. Results are shown in Figure 3.5(d)–(f) and Figure 3.6(d)–(f) for the inversion of P-wave amplitudes only and of P- and S-wave amplitudes, respectively. Although we were able to achieve good fits between theoretical and inverted amplitudes with an RMS error less than 0.25 the influence on the resolution of non-DC components is considerable. Errors in the non-DC components can be up to 15 per cent when P- and S-wave amplitudes are inverted. When inverting only P-wave amplitudes, the errors are two to three times larger. Thus, real non-DC components can easily be masked by spurious non-DC components. Here, including the S-wave amplitudes is very important to obtain sufficiently small errors in the non-DC components in order to be able to discriminate between spurious and real non-DC components.

Furthermore, we observed that normal faulting mechanisms are more sensitive to modelling errors reflecting higher errors in the ISO and CLVD components than strike-slip mechanisms. The reason for this is the unfavourable distribution of stations on the focal sphere for the EW-extensional normal faulting mechanism, because most stations are located close to nodal lines (Figure 3.4). Consequently, the P-wave amplitudes are small and thus more sensitive to errors. The orientations of P- and T-axes show rotations of about 20° for both inversion methods applied to P- and S-wave amplitudes (Figure 3.6f). Inverting only P-wave amplitudes, rotations of P- and T-axes are quite significant and normal faulting mechanisms might even be misinterpreted as a strike-slip mechanism (Figure 3.5f). This confirms again that including S-wave amplitudes is very important for the accurate determination of the orientation of P- and T-axes.

Finally, we simulated inaccuracies in the velocity structure. First, model 1, representing stations on sediments, and model 2, used for stations on hard rock, were used to represent weak errors in the velocity structure. Observed RMS errors are around 0.1 and results for the inversion of P-wave amplitudes only and of P- and S-wave amplitudes are shown in Figure 3.7 and Figure 3.8, respectively. Here, we found small errors in non-DC components being up to ±6 per cent for the inversion of P- and S-wave amplitudes. Deviations for P- and T-axes are 2° or smaller. The errors in the non-DC components significantly increase when only P-wave amplitudes are inverted and also the fault plane can considerably rotate. We further found that the constrained inversion is substantially more stable than the full moment tensor inversion especially when only the P-wave amplitudes are inverted.

Secondly, we further incorporate higher errors in the velocity structure by using only one velocity model common for all stations (model 3, Figure 3.3). This leads to RMS errors around 0.2. As expected, errors in the non-DC components are higher being up to ±13 per cent for the inversion of P- and S-wave amplitudes and up to ±80 per cent for the inversion of only P-wave amplitudes. However, the orientation of P- and T-axes is stable when the P- and S-wave amplitudes are inverted with a rotation smaller than 10°. Here, the errors in the non-DC components and in the deviation of the P and T-axes are similar to the errors introduced by the hypocentre mismodelling. However, inverting only the P-wave amplitudes is resulting in rotations of the P- and T-axes as high as 100°.

Interestingly, we further observe significant variations of errors in dependence on source mechanisms. Errors in the non-DC components of normal faulting mechanisms are at least two to three times higher than those for the strike-slip mechanisms. Furthermore, the errors are decreasing when the percentage of non-DC components is increasing so that tensile normal faulting mechanisms are less sensitive to errors in the velocity structure than pure shear mechanisms. This may be explained by the radiation pattern. The radiation pattern is quadrant for a pure shear source but axially symmetric for a pure tensile source, which is therefore less dependent on directions. Errors in the velocity structure imply ray

deviations, which are less damaging for the tensile crack than for the shear slip. Although the radiation pattern of a shear-tensile slip with slope of 20° is still far from an axial symmetry, it is less sensitive to ray deviations than shear slip sources.

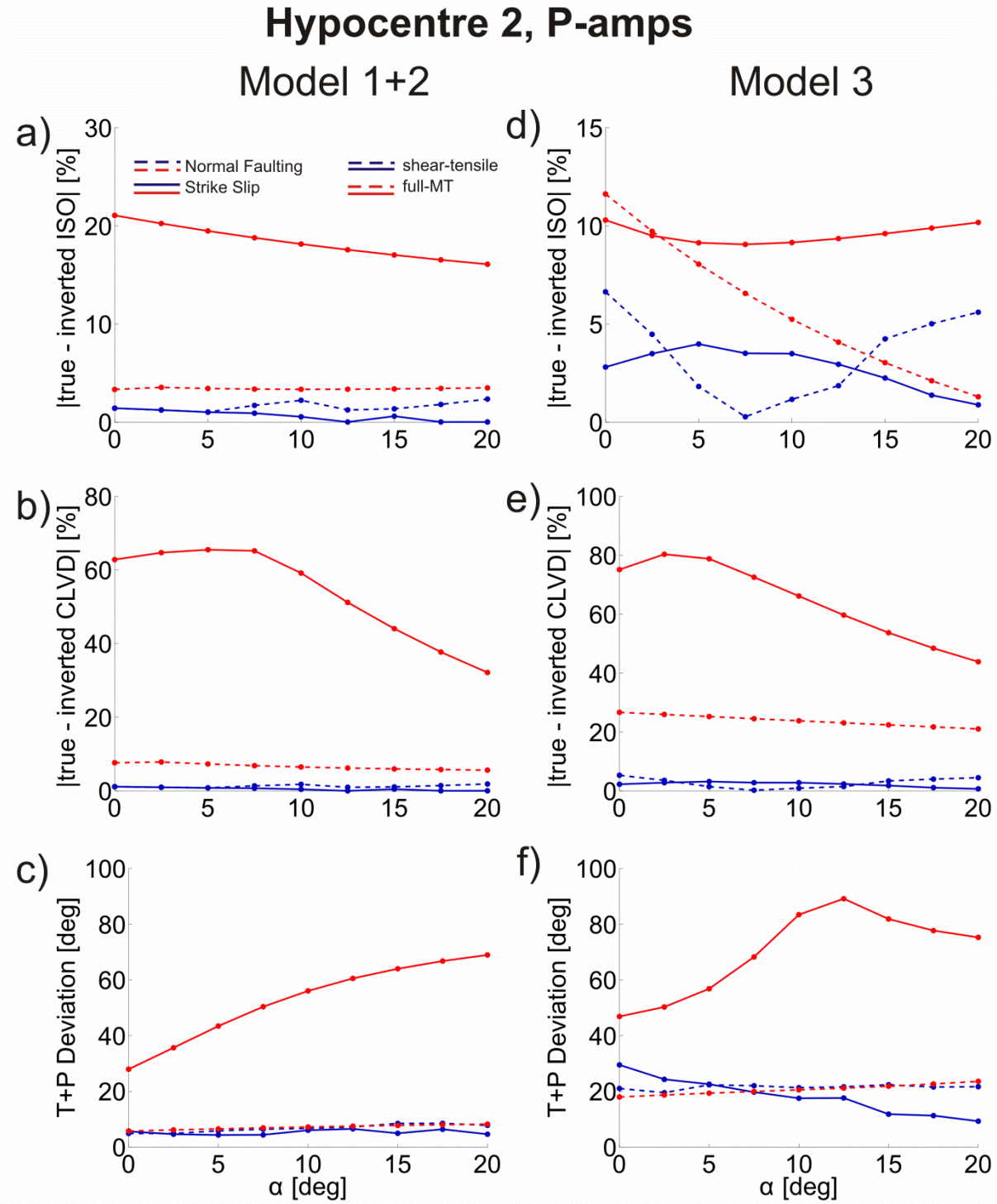

Figure 3.7: Moment tensor inversion for weak (left-hand side) and strong (right-hand side) velocity mismodelling using P-wave amplitudes only at Hypocentre 2. Plots (a) and (b) show the difference between the retrieved and true percentages of ISO and CLVD components, respectively, using model 1+2. Plots (d) and (e) show the same for model 3. The deviations between the P- and T-axes of the retrieved and true fault planes are displayed in plots (a) and (f) for models 1+2 and model 3, respectively.

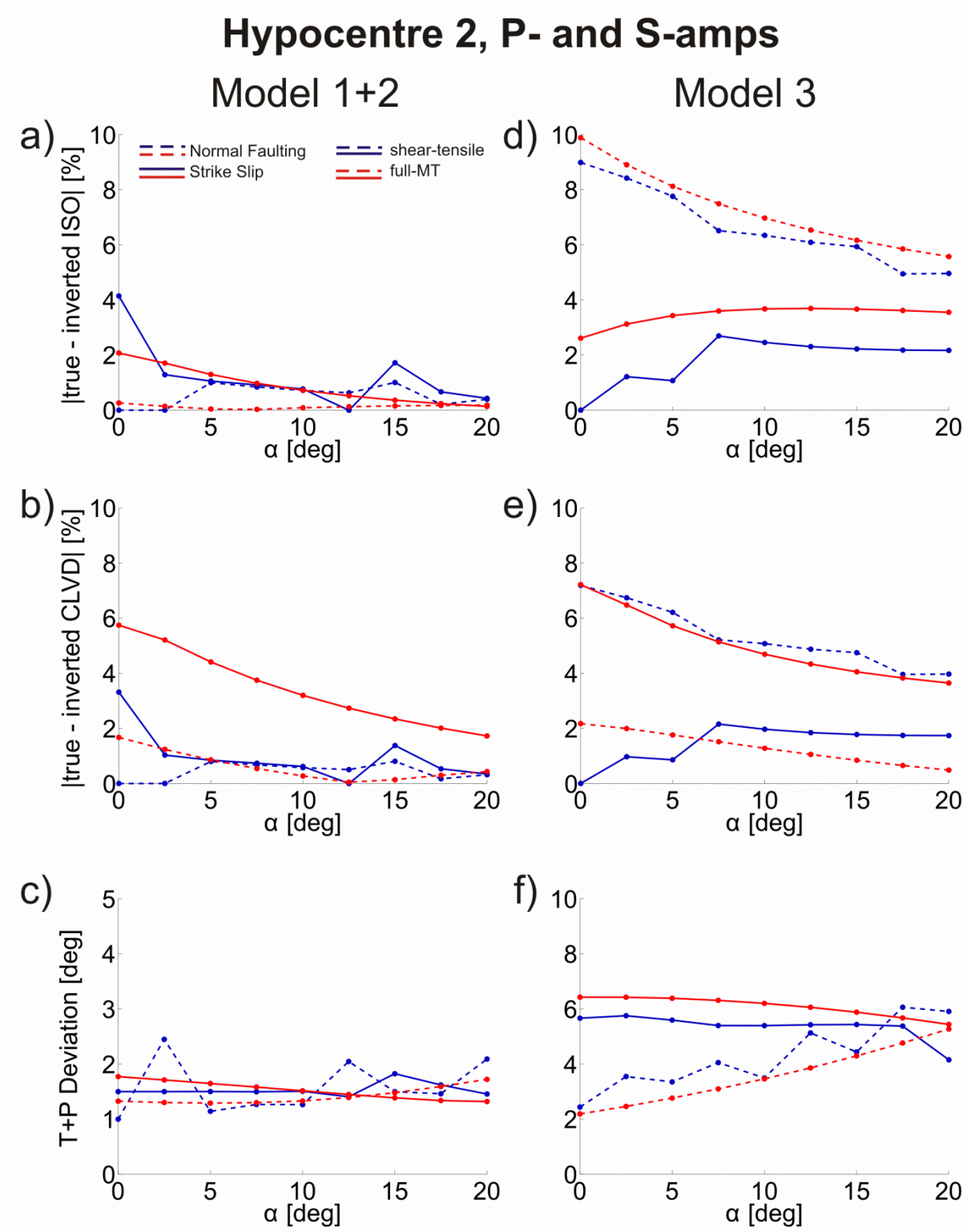

Figure 3.8: Moment tensor inversion for weak (left-hand side) and strong (right-hand side) velocity mismodelling using P- and S-wave amplitudes at Hypocentre 2. For details, see the caption of Figure 3.7.

Finally, we performed tests combining noise contamination, errors in the hypocentre location and inaccuracies in the velocity structure. Noise and errors in the hypocentre location were realized as described above and for simulating the errors in the velocity structure we used model 3 (Figure 3.3) for all stations. We found that the errors remain below ±15 per cent. Thus, the errors do not cumulate, but remain below the error limits, which are observed when the hypocentre mislocation, velocity mismodelling and noise are considered separately.

3.4 CONCLUSIONS

We tested two different moment tensor inversions to analyse their ability to resolve source related non-DC components in regional network data: a linear full moment tensor inversion, and a non-linear inversion constrained to a shear-tensile source model. Adopting a shear-tensile source model, we simulated seismic observations from a regional 35-station seismic network deployed along the rupture of the 1999 Mw = 7.4 Izmit earthquake for monitoring its aftershocks. Based on this synthetic experiment, we arrived at the following conclusions:

- (i) The constrained inversion yields smaller errors in non-DC components especially for the CLVD component. Here, the errors are two to 15 times smaller than for the full moment tensor inversion. The full moment tensor might be a too detailed description of a tectonic source and therefore it can be unstable, if the data quality is low or the velocity structure is poorly known. Constraining the parameter space by the shear-tensile source model reduces the number of possible source mechanisms and non-physical solutions such as explosions or implosions are excluded from the beginning. This makes the inversion much more stable and robust against errors. When real observations of tectonic events are consistent with the shear-tensile source model, such as, for example, aftershocks of the 1999 Izmit earthquake (Stierle et al., 2014a), we recommend applying the non-linear inversion constrained to the shear-tensile source model, since the errors in the non-DC components can clearly be reduced.
- (ii) Retrieving non-DC components from regional seismic networks equipped by short-period stations with apertures in the range of 200–300 km and with station spacing of 20–30 km is particularly difficult due to the lack of observations from stations at epicentral distances less than 15–20 km. This causes irregular focal sphere coverage where near vertical directions are missing.
- (iii) The inversion of P-wave amplitudes alone is not, in general, sufficient for a reliable determination of the non-DC components when using data from regional networks. Therefore, it is necessary to incorporate both, P- and S-wave amplitudes into the inversion.
- (iv) The ISO component is usually less sensitive to errors than the CLVD component when the full moment tensor inversion is applied. This is well explained by properties of the moment tensor decomposition: the ISO component is a linear function while the CLVD component is a non-linear function of eigenvalues of the moment tensor. In contrary, the inversion constrained to a shear-tensile source model links the ISO and CLVD components and the CLVD errors are reduced and thus determined more precisely than for the full moment tensor inversion.
- (v) Even for a network geometry as good as that used for observing the Izmit aftershocks the error bounds of retrieved non-DC components remain considerable. Assuming realistic errors in the modelling procedure, we are able to detect only

significant source related ISO and CLVD components (larger than ±15 per cent). Smaller non-DC components cannot be resolved since the amount of spurious non-DC components can be up to ±15 per cent. However, the expected non-DC components in Izmit aftershocks might be substantially larger given, for example, the extensional settings below the Akyazi Plain.

- (vi) Deviations of P- and T-axes between retrieved and modelled mechanisms are smaller than 15° when P-and S-wave amplitudes are inverted. Thus, the orientation of P- and T-axes can be determined precisely even when errors in modelling procedures are high.
- (vii) When aiming at detecting potential non-DC components by a regional seismic network, we suggest carrying out studies as this one prior to the deployment. Šílený (2009), for example, showed that the network geometry is in particular important when aiming to resolve spurious non-DC components. A carefully designed geometry of seismic network can significantly increase the potential of the network to analyse the DC and non-DC components in the seismic moment tensors and thus bring new information on seismic source processes in the region of interest.

4 Resolution of Non-Double-Couple Components in The Seismic Moment Tensor using Regional Networks: 2. Application to Aftershocks of the 1999 M_w 7.4 Izmit Earthquake[2]

SUMMARY

We study potential non-double-couple (non-DC) components in aftershocks of the 1999 Izmit earthquake. The Izmit earthquake ruptured a ∼140 km long segment of the North Anatolian Fault Zone in north western Turkey and was followed by the M_w = 7.1 Düzce earthquake that extended the rupture further to the east. Focal mechanisms of Izmit aftershocks clearly indicate a segmentation of the rupture into several segments, one of which is the Akyazi Plain, a pull-apart structure, where significant non-DC components might be observed. The analysed earthquake catalogue contains waveforms of more than 4000 accurately located events observed at 35 three-component short-period seismic stations. To ensure high-quality data with good focal coverage, we apply strict quality criteria to the aftershock catalogue reducing the number of events to only 33 aftershocks for which stable moment tensors were calculated using P- and S-wave amplitudes. The moment tensors of the 33 analysed aftershocks display significant differences in the percentage of the non-DC components for the three distinct fault segments: the Izmit-Sapanca, Karadere-Düzce and the Akyazi segments. Events located in the Izmit-Sapanca and Karadere-Düzce segments exhibit only small percentages of the non-DC components and if existent they are mainly positive. This correlates well with the predominant strike-slip stress regime along this segment and also with the main shock rupture being right lateral strike-slip. In contrary, we found a substantial percentage of non-DC components for events below the Akyazi Plain where the Sapanca Fault splits into the Mudurnu and Karadere faults. There, the observed non-DC components are entirely positive indicating a tensional regime and ranging from 20 to 48 per cent, clearly exceeding the defined error bounds found in a synthetic study. This observation is in accordance with the post-seismic setting following the Izmit main shock that left a remarkable slip deficit of 3.5 m below the Akyazi bend.

[2] This article has been published in the Geophysical Journal International: E. Stierle, M. Bohnhoff, and V. Vavryčuk (2014). Resolution of Non-Double-Couple Components in The Seismic Moment Tensor using Regional Networks: 2. Application to Aftershocks of the 1999 Mw 7.4 Izmit Earthquake. 196(3), 1878-1888, doi: 10.1093/gji/ggt503.

4.1 INTRODUCTION

The seismic moment tensor has become one of the most efficient tools for describing and investigating earthquake source processes. It contains information on the orientation of a fault, slip direction and type of faulting. It is capable to describe shear faulting on a planar rupture surface by its double-couple (DC) component but it may reveal also deviations from pure shear faulting if non-double-couple (non-DC) components are present in the moment tensor (Julian et al., 1998; Miller et al., 1998). The origin of non-DC components can be either in the source process itself ('real' non-DC) reflecting specific physical properties of the source (Foulger et al., 2004) or in the medium in the focal area (Vavryčuk, 2005). Furthermore, non- DC components can be artefacts of data processing ('artificial' or 'spurious' non-DC components) produced by errors in the velocity structure, hypocentre location or noise in the data (Šílený, 2009). The most common origins of the real non-DC components are: (1) volumetric changes in the source area resulting in tensile faulting with crustal fluids playing an important role (Vavryčuk, 2002) or (2) a complex fault geometry (Julian et al., 1998). Here, we focus on detecting potential non-DC components in aftershocks of the 1999 M_w = 7.4 Izmit. The Izmit earthquake ruptured a ~140-km-long segment of the North Anatolian Fault Zone (NAFZ) in north western Turkey and it was followed by another main shock, the M_w =7.1 Düzce earthquake, 3 months later extending the rupture further to the east (Tibi et al., 2001; Gülen et al., 2002).

A 35-station seismic network covering the entire Izmit rupture with an average spacing of about 15 km was completed only 4 days after the main shock allowing to record a unique data set of Izmit aftershocks (Baumbach et al., 2003; Bulut et al., 2007; Figure 4.1). Analysis of Izmit aftershock focal mechanisms allowed to identify a strong partitioning of deformation and stress along the rupture (Bohnhoff et al., 2006). While focal mechanisms of

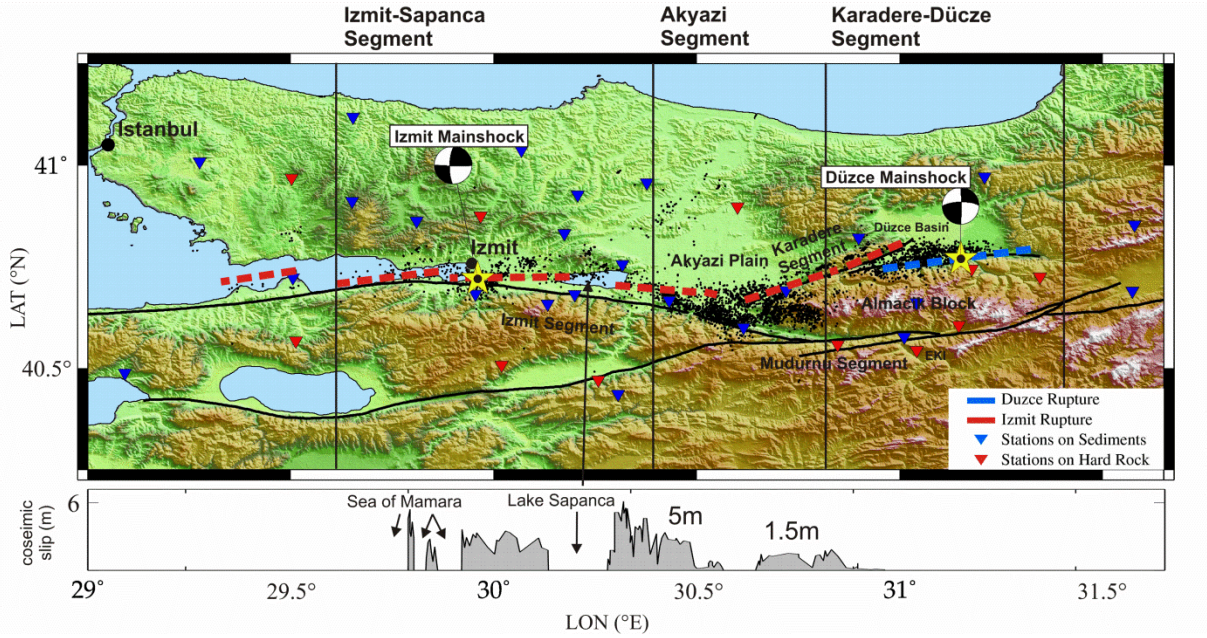

Figure 4.1: Seismotectonic setting of the Izmit section of the North Anatolian Fault Zone (NAFZ) with major mapped faults and surface ruptures of the 1999 Izmit and subsequent Düzce earthquakes (after Barka et al., 2002). Black dots represent relocated aftershocks from Bulut et al. (2007) and triangles denote locations of stations. The segmentation along the Izmit rupture is based on lateral changes of aftershock focal mechanisms (after Bohnhoff et al., 2006). Fault lines are taken from the Turkey General Directorate of Mineral Research and Exploration. Lower plot: Lateral distribution of coseismic surface slip during the Izmit earthquake (after Barka et al., 2002).

the Izmit and subsequent Düzce main shock indicate right-lateral strike-slip faulting, about 40 per cent of all Izmit aftershock focal mechanisms were EW extensional normal faulting, pinpointing to an extensional structure below the Akyazi Plain (Akyazi Segment in Figure 4.1). This area reflects a local topographical depression subsided by ∼500 m with respect to the surrounding region representing a small pull-apart structure similar to the Sea of Marmara (Armijo et al., 2002) but in a more juvenile state (Bohnhoff et al., 2006). The occurrence of normal faulting mechanisms below the Akyazi Plain is well explained by the coseismic slip deficit of ∼3.5 m (Tibi et al., 2001; Barka et al., 2002). The slip deficit activated pre-existing NS-oriented normal faults (Bulut et al., 2007) suggesting strong tensional components, which is abetting the occurrence of non-DC components of moment tensors. Therefore, we selected the Izmit rupture as an ideal site to study the occurrence of non-DC components in aftershock moment tensors during a post-seismic scenario. For a comparison, we also include the Izmit-Sapanca and Karadere-Düzce segments of the Izmit rupture where dominantly strike-slip mechanisms are observed (Figure 4.1).

Note that reliably detecting potential non-DC components in moment tensors is not an easy task but a rather demanding procedure which needs: high-quality data observed by a dense network of stations, accurate locations and good knowledge of the medium. Obviously, in most cases, it is not possible to fully satisfy such strict criteria and thus to completely exclude the presence of spurious non-DC components. Therefore, any proper analysis of observed non-DC components should include a resolution study revealing detection capability of the given network. Such a study for the Izmit aftershocks is presented in the companion paper by Stierle et al. (2014b). This paper shows that the given regional network configuration is, in principal, capable to detect the real non-DC components provided, if (1) the real non-DC components are higher than ±15 per cent, (2) the moment tensors are inverted using P- as well as S-wave amplitudes, (3) absolute errors in hypocentre location are smaller than 2.5 km (Bulut et al., 2007) and (4) at least basic characteristics of the velocity model are known when computing the Green's functions (e.g. whether the analysed station is deployed on the sediments or hard rock). The synthetic study also reveals that the retrieved isotropic (ISO) percentage is more reliable than the compensated linear vector dipole (CLVD) percentage and that the constrained moment tensor inversion for a shear-tensile model is preferable over the full moment tensor inversion with no constraints.

4.2 *Data and Method*

Aftershocks of the 1999 Izmit earthquake were recorded by a 35-station seismic network covering the entire rupture zone. Stations were equipped with three-component sensors of 1 Hz natural frequency. Waveform recordings are simple and generally show good signal-to-noise ratios with clear P- and S-wave onsets (Figure 4.2). The seismograms are sufficiently broadband for local events with magnitudes between 1 and 4, so they do not need to be corrected for the instrument response. Waveforms of events with a greater magnitude (>4) might by distorted in the low frequency range and the scalar seismic moment can be underestimated.

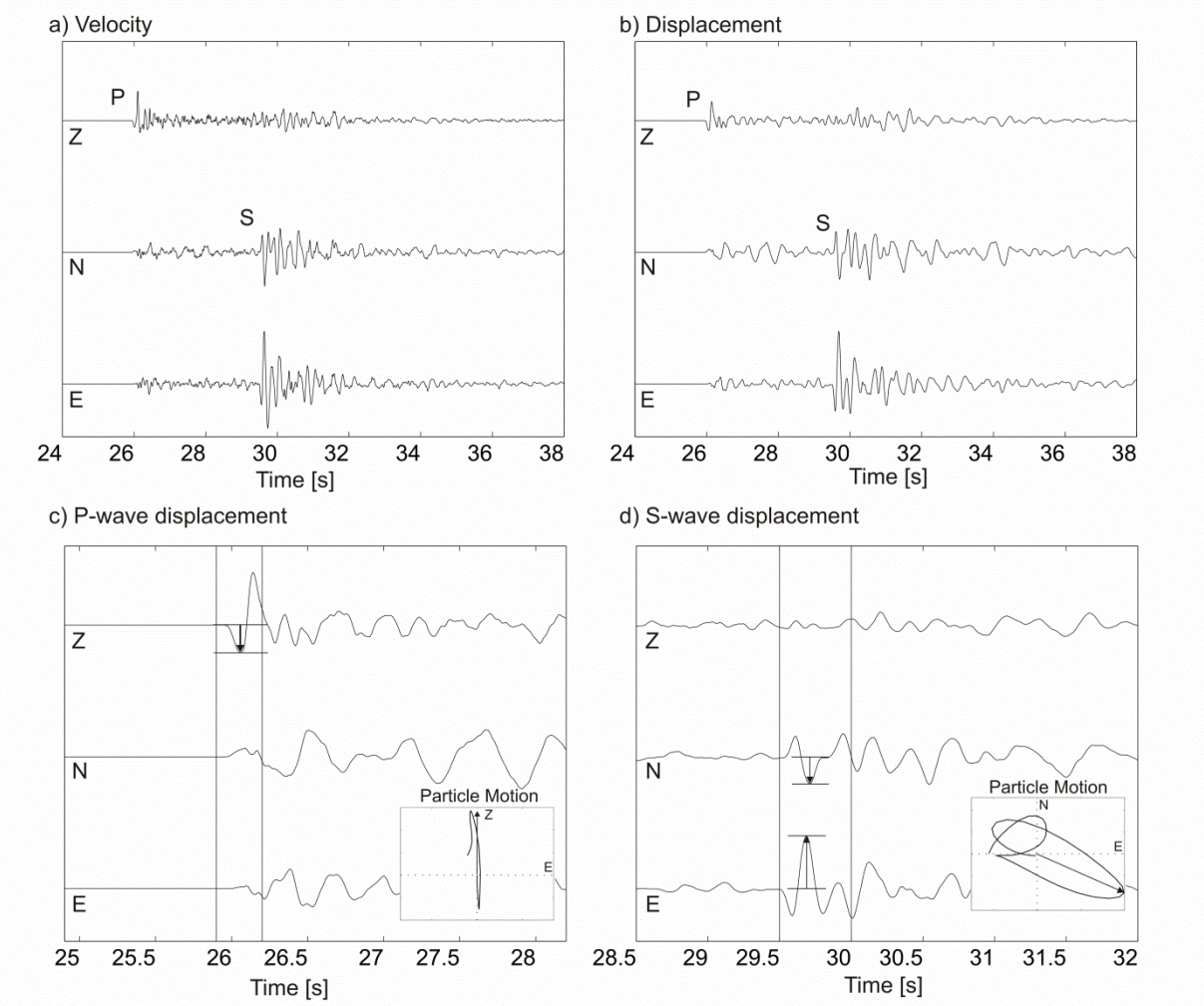

Figure 4.2 Velocity and displacement recordings of M_w=3.4 1999 Izmit aftershock (event ID 28) recorded at station EKI (Figure 4.1) and located at an epicentral distance of 27 km. a) Velocity recordings. b) Displacement recordings, filtered with a band pass filter between 0.5 and 35 Hz. c) and d) P-wave and S-wave displacement respectively. Black lines denote the time frame used for the particle motion plot indicating the direction of the incoming P- and S-waves, respectively.

Since waveforms at all stations are distorted in the same way, the absolute values of the moment tensors are affected, but the relative values of the moment tensors should remain correct. Since we invert only for the relative moment tensors, our results are not affected by the instrument response. The network recorded more than 10 000 events of which 4600 events were relocated with an internal precision of less than 400 m. The aftershocks delineate the entire rupture zone and focal depth extends down to 16 km (Bulut et al., 2007).

Strict selection criteria are needed to fulfil requirements for reliable characterization of potential non-DC components in the moment tensors Stierle et al. (2014b). To ensure high-quality data, we selected events by applying the following criteria: (1) The event was recorded at a minimum of 15 stations; (2) The magnitude of the events must fall in the range between 2 and 4.5 and (3) The hypocentral depth is between 5 and 16 km. Applying these constraints to the catalogue of located aftershocks, the number of events decreased from 4500 to 667. Of these, 140 were located along the Izmit-Sapanca Segment, 368 along the Akyazi Segment and 159 along the Karadere-Düzce Segment, respectively (see Figure 4.1).

a) Stations on sediments

v_P (km/s)	Depth (km)	v_P/v_S	Q_P	Q_S
2.90	0.00	1.75	150	75
4.70	1.00	1.75	400	200
5.30	7.00	1.75	550	275
6.06	11.00	1.75	700	350
7.20	15.00	1.75	800	400
8.06	35.00	1.75	1000	500

b) Stations on hard rock

v_P (km/s)	Depth (km)	v_P/v_S	Q_P	Q_S
4.70	0.00	1.75	400	200
5.30	7.00	1.75	550	275
6.06	11.00	1.75	700	350
7.20	15.00	1.75	800	400
8.06	35.00	1.75	1000	500

Table 4.1: 1D velocity models of the crust. v_P is the P-wave velocity (modified after Bulut et al., 2007), v_P/v_S is the ratio of P- and S-wave velocities, Q_P and Q_S are the quality factors of P and S-waves, respectively.

The P- and S-wave amplitudes were measured on the displacement records filtered with a Butterworth bandpass filter with corner frequencies 0.5 and 35 Hz to reduce noise effects. Since the incidence angle of arriving waves is near vertical at most stations because of the uppermost soft-sedimentary layer, we picked the P-wave amplitudes on the vertical components and the S-wave amplitudes on the horizontal components, respectively (Figure 4.2). The amplitudes were picked manually, where the maximum S-wave amplitudes were further constrained by visual inspection of particle motion plots (Figure 4.2). Since the S waves were usually more complicated and difficult to interpret, we measured only clear S-wave amplitudes mostly from stations with small epicentral distances. Measurements of the S waves which displayed any anomalies such as shear wave splitting (Hurd & Bohnhoff, 2012; Eken et al., 2013) were excluded. As a result, we were able to include up to six S-wave amplitudes per event. Nevertheless, information on the S-wave amplitudes was important in the inversion and considerably stabilized the resultant moment tensors (Stierle et al., 2014b).

The Green's functions are determined using ray theory (Červený, 2001). Since the modelling of Pn waves is complicated and cannot easily be calculated with standard ray theory, recordings for epicentral distances larger than 80 km were excluded. The effect of the flat free Earth's surface is incorporated in the Green's functions. As in Stierle et al. (2014b), we used two smoothed velocity models (Table 4.1) in order to be able to distinguish between stations on hard rock and stations on a shallow sediment layer. Stations on hard rock are defined as suggested by Parolai et al. (2004). The remaining stations are considered to be situated on sediments. Since attenuation is different for hard rock and sediments (Bindi et al., 2006) we corrected theoretical amplitudes for the effect of attenuation after Červený (2001) using a dissipative filter, which yields the frequency-dependent traveltime perturbations along rays. The attenuation parameters QP and QS are listed in Table 4.1. We tested also some other values of attenuation and evaluated errors due to an inaccurate attenuation model and found that these errors are insignificant.

We started with inverting the P- and S-wave amplitudes for the full moment tensors using a linear inversion scheme. Results are shown in Table 4.2. We found that the moment tensors display a rather high scatter, in particular, in the CLVD component, which was about three times larger than in the ISO component. To stabilize the inversion, we decided to invert for the shear-tensile source model using a non-linear inversion as described in Stierle et al. (2014b). Before applying this constrained inversion, we tested whether the shear-tensile source model is consistent with the data and thus suitable for the data interpretation. According to Vavryčuk (2011, his equation 21), we determined the consistency coefficient for the analysed events. The coefficient can range from −1 to 1;

positive values indicate that the data are consistent with the shear-tensile model, and negative values are a measure of the inconsistency. The closer the value is to −1 the stronger is the inconsistency. We obtained values between −0.3 and 0.8, where the most events yield positive consistency factors (Table 4.2). This indicates that the shear-tensile source model is appropriate to be adopted in the inversion. A detailed description of individual steps of the inversion constrained to a shear-tensile source model can be found in Stierle et al. (2014b).

ID	Strike	Dip	Rake	DC [%]	CLVD [%]	ISO [%]	Consistency factor
1	80.1	61.4	124.0	48	31	20	0.5
2	136.2	79.4	-12.1	88	-2	11	-0.1
3	328.4	78.7	20.2	66	22	12	0.3
4	242.0	74.1	-139.9	58	38	4	0.4
5	149.1	79.0	7.3	61	39	0	0.4
6	80.0	68.6	168.8	96	-4	0	0.0
7	351.4	45.2	-35.6	83	16	-1	-0.2
8	207.5	76.4	-168.5	56	43	2	0.4
9	262.7	67.8	-72.3	72	23	5	0.3
10	201.6	58.2	-36.9	75	-7	17	-0.2
11	348.4	50.9	-139.1	79	0	20	0.2
12	335.3	55.1	-149.8	77	-1	22	-0.2
13	355.4	48.8	-102.9	66	16	18	0.3
14	191.4	43.1	-88.1	89	-9	2	-0.1
15	187.8	66.4	-66.7	80	2	18	0.2
16	329.0	60.0	-144.0	51	8	41	0.5
17	335.2	65.2	-139.4	23	45	32	0.8
18	8.1	44.1	-79.3	54	24	22	0.5
19	230.8	59.8	-53.9	66	16	18	0.3
20	161.6	44.0	-148.1	80	-6	14	-0.2
21	136.7	69.6	115.9	24	44	33	0.8
22	201.2	33.0	-33.6	76	16	7	0.2
23	1.6	48.5	-109.4	76	15	9	0.2
24	224.8	67.5	-47.4	66	-13	21	-0.3
25	143.8	85.1	146.9	57	13	30	0.4
26	181.5	49.3	43.1	80	6	14	0.2
27	80.3	85.1	157.3	66	-23	11	-0.3
28	300.5	77.7	141.9	75	-16	8	-0.2
29	175.6	88.7	-14.6	84	9	7	0.2
30	12.3	88.4	-5.1	42	57	2	0.6
31	156.1	76.6	6.6	73	13	14	0.3
32	243.7	64.3	138.5	29	53	17	0.7
33	153.6	86.3	-6.6	70	-16	14	-0.3

Table 4.2: Focal mechanisms and non-DC components obtained by the full moment tensor inversion, and their consistency factor determined after Vavryčuk (2011) for 33 selected events.

The decomposition of the moment tensor into the percentages of DC and non-DC components was performed after Vavryčuk (2001), where the non-DC component consists of the ISO and CLVD components. The reliability of the moment tensor solution was assessed by the misfit of theoretical and observed amplitudes and by inverting data contaminated by random noise and by Jackknife tests. The misfit was calculated by the normalized root-mean-square (RMS) difference between theoretical and observed amplitudes (Stierle et al., 2014b, her equation 5).

RMS Values close to zero represent a good fit of amplitudes whereas RMS values close to one indicate no fit of amplitudes. Solutions were classified as reliable if the misfit was smaller than 0.3. Furthermore, to assess the stability of the retrieved moment tensor, we repeated the inversion with randomly generated noisy input data as well as we inverted subsets of available data (Jackknife test). The noise is uniformly distributed with a maximum noise level reaching 25 per cent of the observed amplitude at the respective station. For each event, 100 realizations were performed. For the Jackknife test, we run several inversions in which one station was excluded. Thus the number of realizations equals the number of stations recording the respective event minus 1. The resulting errors in terms of standard deviations are similar to the errors obtained by noise tests. Figure 4.3 shows the best-fitting moment tensor solution as well as the results for the noise test of one event in each segment using constrained and full moment tensor inversion techniques. The scatter of compressional (P) and tensional (T) axes and errors in the non-DC components are higher when using full moment tensor inversion. Thus, the constrained moment tensor inversion reveals much more stable results with smaller errors in the non-DC components, which is in a good correspondence with our observations in the synthetic case study (Stierle et al., 2014b).

The large scatter of P- and T-axes of the retrieved moment tensors as well as high variations in non-DC components are indicators of unstable and thus unreliable mechanisms. We defined an event to be stable if the mean deviation of the P- and T-axes was less than 10◦ and if the standard deviation of the percentage for the ISO and CLVD components was less than ±15 per cent, respectively, according to the retrieved error bounds of Stierle et al. (2014b). Furthermore, we also compared the moment tensor solution constrained to the shear-tensile source model to the solution of the full moment tensor inversion. For stable solutions, the P- and T-axes deviated with angles less than ±10◦.

4.3 Results and Discussion

We analysed 667 events from the Izmit aftershock catalogue fulfilling the constraints described earlier. Applying strict stability conditions to ensure only high-quality moment tensors, the number of events was further reduced to a total of 33. This decrease is drastic but well explained by applying profound quality criteria as pointed out above and based on the synthetic study for the Izmit aftershock network (Stierle et al., 2014b). Note that a similar reduction of events was also reported for the study of non-DC components for induced seismic events at the Geysers geothermal field in California (Ross et al., 1996). We found that including S-wave amplitudes in the moment tensor inversion is essential in most cases for stabilizing the moment tensors. Even including a few S-wave amplitudes was important and reduced errors in the non-DC components. Especially for rather poor focal sphere coverage, the inversion of P-wave amplitudes can be unstable and not reliable. Here, including the S-wave amplitudes is essential for improving the moment tensor solutions.

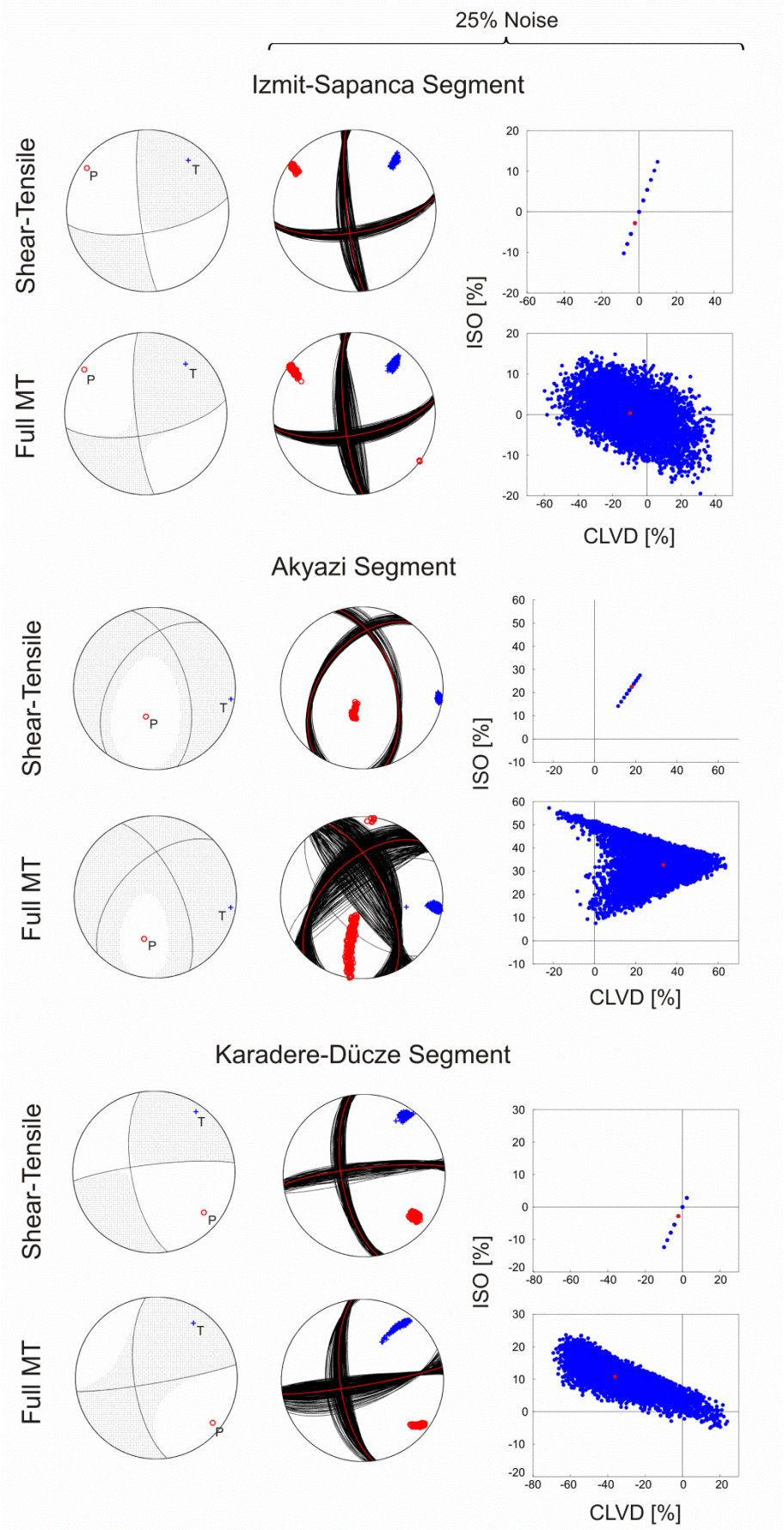

Figure 4.3 Results of the inversion for selected events from each of the three segments along the Izmit rupture (Izmit-Sapanca Segment: Event 6, Akyazi Segment: Event 17, Karadere-Düzce Segment: Event 27). Stable results obtained by constrained (top row) and full (bottom row) moment tensor inversion are shown. Left column shows the best-fit solution, middle and right columns show the scatter of nodal lines, P- and T-axes and distribution of non-DC components, respectively, computed by adding random noise with a level of 25% to analysed amplitudes.

Of the 33 events, nine are located along the Izmit-Sapanca Segment, 17 along the Akyazi Segment and seven along the Karadere-Düzce Segment. The magnitudes of the events range from 2.5 to 4.3. The strike, dip and rake as well as the RMS values of the analysed events are listed in Table 4.3; the retrieved non-DC contents of moment tensors are listed in Table 4.4. Furthermore, the standard deviations of the ISO and CLVD components are given as a result of the noise and Jackknife tests. We obtained misfits ranging from 0.04 to 0.28. Standard deviations of the ISO and CLVD components are similar for the noise and Jackknife test being up to ±9 per cent.

The full moment tensor solutions for all 33 stable events are plotted on the lower hemisphere in Figure 4.4. Figure 4.5 shows the epicentre locations of the events along the Izmit rupture together with the beach balls showing the full moment tensor solutions. Events along the Izmit-Sapanca Segment are predominantly strike-slip mechanisms being well represented by simple shear on a planar surface. Events 2, 3, 4, 5 and 8 are pure shear strike-slip mechanisms which occurred off the main fault with a strike rotated by about 40◦ on average with respect to the EW strike of the main fault. These events might indicate reactivation of secondary Riedel-type faults (Tchalenko, 1970) developed in early stages of the evolution of the North Anatolian Fault and currently being located within a few kilometres to the principal slip zone to either side of the fault. This observation is in a good agreement with Izmit aftershocks being generally located off-fault (Bulut et al., 2007). For the remaining events along the Izmit-Sapanca Segment (some of them include substantial normal faulting components), one of the possible fault planes roughly follows the strike of the main fault. These results correspond with the transtensional tectonic setting at this part of the Izmit rupture (Bohnhoff et al., 2006).

Along the Akyazi Segment, we retrieved stable moment tensors of 17 events. Almost all events show pure EW-extensional normal faulting mechanisms with significant positive non-DC components. These events are located below the Akyazi Plain, an area of a local topographic depression subsided by 500 m with respect to the surrounding formations. In the Akyazi Plain north of the Izmit surface rupture, almost no aftershocks are observed since no strain was released here during the main shock. Towards the east, the main fault splits into the NE-trending Karadere Fault and the ESE-trending Mudurnu Segment. While the Karadere Fault was activated during the Izmit event the Mudurnu section that hosted an M7.1 earthquake in 1967 (Ambraseys & Zatopek, 1969) remained inactive during the Izmit rupture and even did not host a single aftershock. This indicates that it is still early in its seismic cycle.

The scatter of event locations below the Akyazi Plain as well as the fragmentation of the formation into several small-scale NS-trending faults (Bulut et al., 2007) indicates complex structures, where the released strain from the main shock is distributed over several subsidiary faults. Here, a significant slip deficit of approximately 3.5 m was accumulated during the Izmit main shock resulting in pronounced aftershock activity with predominantly EW-extensional normal faulting mechanisms (Bohnhoff et al., 2006) promoting tensional components in the source mechanism manifested by significant positive non-DC components. We identified only one event out of 17 events located along this segment reflecting a strike-slip mechanism (Event 26 in Table 4.3 and Table 4.4). This pure shear event occurred 17 days after the main shock. Approximately 12–16 days after the main shock, when most of the 3.5 m slip deficit below the Akyazi Plain seemed to have been adjusted, the extensional normal faulting regime deceased and migrated towards the Düzce Basin where the Düzce event nucleated 87 days after the Izmit earthquake. The strike-slip event below the Akyazi Plain with insignificant non-DC components thus supports the

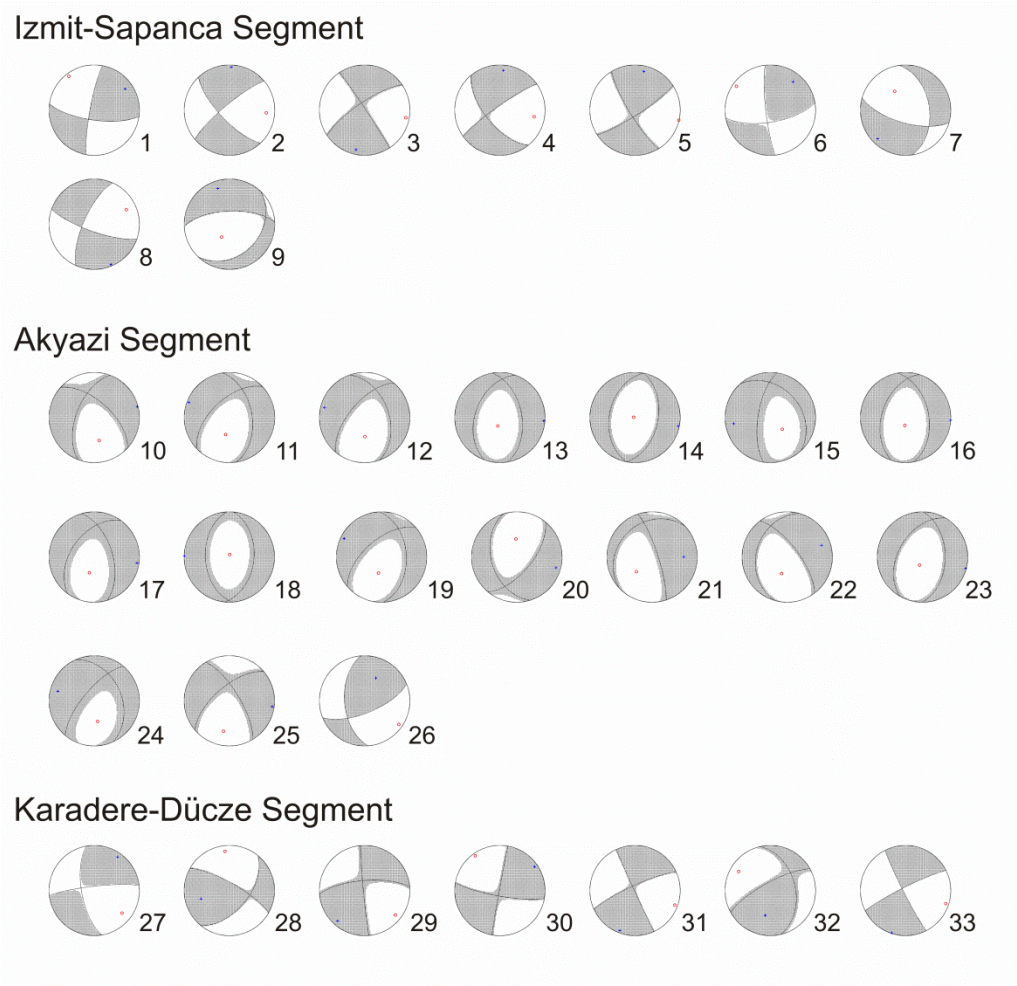

Figure 4.4: Full moment tensor solutions for the 33 stable events determined using the moment tensor inversion constrained to a shear-tensile source model. The lower-hemisphere equal-area projection is used. Compression zones are grey-shaded and red and blue dots indicate resulting P and T axes, respectively.

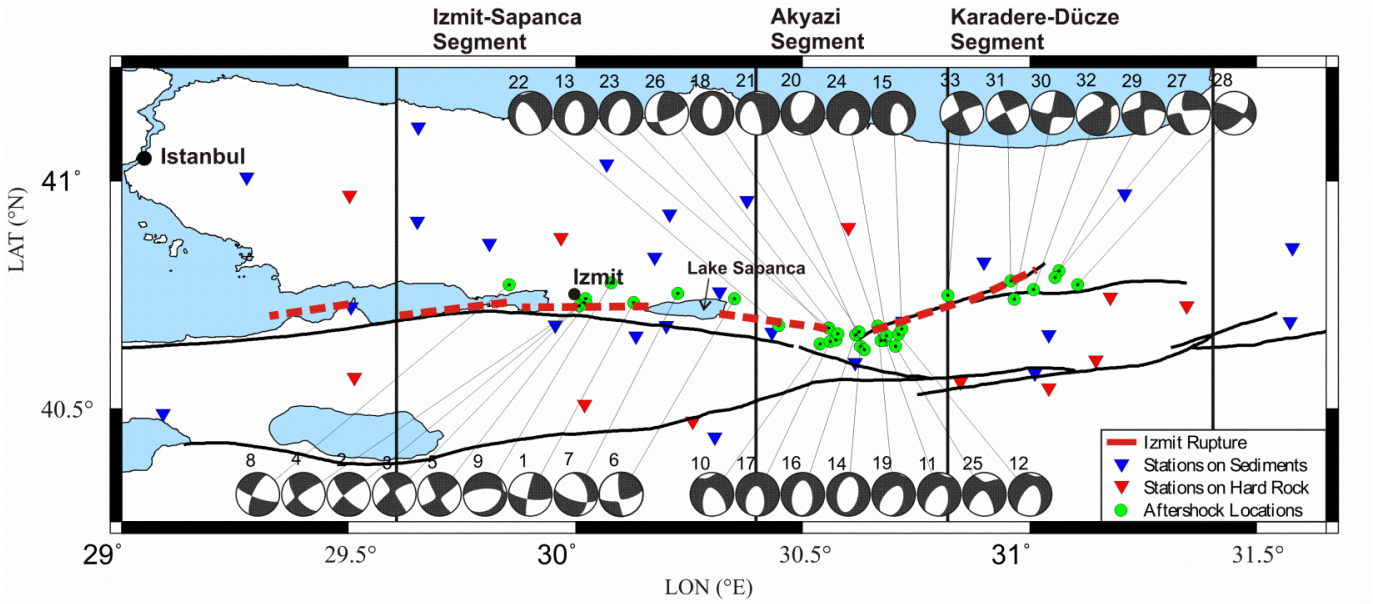

Figure 4.5: Map view of the lower-hemisphere projection of the 33 stable aftershock fault plane solutions. The ID of each event is plotted above the beach ball. Black lines are fault lines taken from the Turkey General Directorate of Mineral Research and Exploration and red lines are surface rupture of the 1999 Izmit earthquake observed by Barka et al. (2002).

ID	Month	Day	Hour	Min	Sec	Lat [°]	Lon [°]	Dep [km]	M_L	# P Amp	# S Amp	RMS	Strike [°]	Dip [°]	Rake [°]
1	8	27	15	40	30.6	40.73	30.13	15.0	3.5	19	3	0.13	190	82	18
2	8	28	8	28	36	40.73	30.02	10.9	3.8	19	5	0.11	230	80	-162
3	9	2	19	33	33.2	40.74	30.02	10.0	2.8	18	3	0.12	327	88	14
4	9	4	10	31	43.3	40.73	30.01	9.8	4.3	18	5	0.20	141	63	-8
5	9	4	10	45	51	40.73	30.02	11.2	3.2	14	5	0.15	149	80	9
6	9	4	18	28	33.9	40.74	30.35	11.0	3.9	13	8	0.12	80	68	171
7	9	24	13	45	41.6	40.74	30.28	13.0	4.1	14	2	0.05	106	67	-131
8	10	5	4	10	53.8	40.77	29.85	9.6	3.7	16	2	0.23	204	71	-166
9	10	9	21	33	36.9	40.78	30.08	8.7	3.3	12	6	0.25	43	32	-130
10	8	30	4	1	2.4	40.64	30.54	11.1	2.7	19	3	0.28	201	57	-36
11	8	30	19	22	48.4	40.65	30.68	11.1	2.5	21	1	0.16	226	57	-52
12	9	1	2	54	31.1	40.66	30.71	11.1	2.6	21	1	0.16	220	63	-52
13	9	1	4	3	44.5	40.68	30.56	11.1	2.8	21	6	0.07	350	50	-110
14	9	1	19	9	27.9	40.64	30.63	10.5	2.5	17	5	0.18	191	43	-90
15	9	1	21	39	7.5	40.67	30.72	13.0	2.6	15	4	0.11	189	68	-65
16	9	3	14	23	24.5	40.66	30.62	11.1	2.9	19	1	0.14	350	47	-110
17	8	30	18	0	50.1	40.65	30.56	11.1	2.7	17	6	0.20	343	57	-126
18	9	2	18	39	41.2	40.67	30.62	11.1	3.1	16	2	0.28	6	45	-84
19	9	1	1	0	15.2	40.68	30.67	11.0	2.8	17	5	0.26	229	59	-57
20	9	2	11	19	4.3	40.65	30.67	10.9	3.3	16	7	0.24	163	43	-138
21	8	30	4	35	16	40.63	30.64	15.4	3.2	17	3	0.16	342	79	-112
22	9	1	17	15	29.1	40.68	30.45	11.3	2.6	20	3	0.24	196	32	-42
23	9	2	7	0	42.3	40.65	30.57	11.1	2.9	14	7	0.23	0	48	-111
24	9	2	7	10	15.6	40.66	30.68	10.9	2.8	15	4	0.28	220	70	-55
25	9	2	14	21	4.6	40.64	30.70	13.7	2.7	16	3	0.16	230	64	-20
26	9	3	7	26	53.6	40.66	30.58	11.1	2.8	18	4	0.26	68	68	140
27	8	30	0	57	3.3	40.80	31.06	7.0	3.1	16	1	0.09	263	82	-157
28	9	2	4	18	23.1	40.77	31.11	7.2	3.4	16	6	0.24	39	55	17
29	10	2	2	47	52.7	40.79	31.06	7.7	3.1	14	4	0.12	175	88	-18
30	9	1	7	58	1.8	40.74	30.97	7.0	3.0	14	2	0.18	190	89	10
31	10	13	11	11	36.2	40.78	30.96	7.0	3.4	12	3	0.04	155	89	-9
32	9	12	14	34	53.8	40.76	31.01	5.7	3.3	14	2	0.15	241	76	132
33	8	30	21	14	5.8	40.75	30.82	12.9	3.4	18	2	0.20	243	84	-176

Table 4.3: Focal mechanisms in terms of strike, dip, and rake of 33 selected events obtained by the inversion constrained to the shear-tensile source model. Furthermore the origin time, local magnitude (M_L), number of P- and S-wave amplitudes inverted and the RMS are shown.

ID	DC [%]	CLVD [%]	ISO [%]	Noise σ_{ISO} [%]	Noise σ_{CLVD} [%]	Jackknife σ_{ISO} [%]	Jackknife σ_{CLVD} [%]
1	100	0	0	3.3	2.6	3.3	2.6
2	100	0	0	3.9	3.1	2.6	2.0
3	90	4	6	2.7	2.1	2.5	2.0
4	95	2	3	2.6	2.1	2.9	2.3
5	90	4	6	3.3	2.7	3.5	2.8
6	95	-2	-3	4.5	3.6	1.8	1.5
7	100	0	0	4.5	3.6	3.4	2.8
8	100	0	0	4.4	3.5	5.7	4.5
9	95	2	3	6.8	5.4	5.3	4.2
10	74	12	14	5.2	4.1	7.4	5.9
11	71	13	16	6.9	5.5	5.5	4.4
12	74	12	14	8.1	6.5	6.7	5.4
13	68	14	18	6.2	5.0	1.7	1.4
14	78	10	12	5.9	4.8	3.1	2.5
15	57	19	24	5.3	4.3	2.9	2.3
16	74	12	14	2.8	2.2	1.8	1.4
17	59	18	23	2.5	2.0	2.1	1.7
18	65	15	20	2.8	2.3	2.3	1.8
19	68	14	18	7.4	5.9	6.6	5.2
20	78	10	12	3.1	2.5	2.0	1.6
21	74	12	14	1.0	0.8	6.9	5.6
22	82	8	10	8.7	7.0	6.5	5.2
23	78	10	12	3.3	2.6	3.7	2.9
24	52	22	26	2.6	2.1	3.4	2.7
25	78	10	12	3.1	2.5	1.6	1.3
26	100	0	0	3.0	2.4	3.1	2.5
27	95	-2	-3	3.8	3.1	2.7	2.2
28	95	2	3	2.7	2.1	5.1	4.1
29	86	6	8	5.7	4.6	2.0	1.6
30	90	4	6	6.9	5.5	3.4	2.7
31	95	2	3	4.5	3.6	3.6	2.9
32	82	8	10	6.3	5.0	0.9	0.7
33	100	0	0	3.2	2.6	1.4	1.1

Table 4.4: Non-DC components of the moment tensors obtained by the inversion constrained to the shear-tensile source model and their stability for the 33 selected events.

findings that this part of the Izmit rupture released the coseismic slip deficit within the first 2 weeks after the main shock then turning back to its pre-Izmit strike-slip, pure shear setting (Ickrath et al., 2013).

East of the Akyazi Plain, we retrieved stable moment tensors for seven events that were located along the Karadere-Düzce Segment. Since this segment is situated at the eastern end of the network (and the Izmit rupture) the azimuthal coverage is rather poor compared to the remaining segments and therefore it was particularly difficult to obtain

stable results despite the high number of aftershocks in this region. Fault plane solutions for these events are dominantly strike-slip, which is in agreement with the observations of Orgülü & Aktar (2001) and Görgün et al. (2010). The percentage of non-DC components is insignificant. Events 31 and 33 are located on the N65◦-trending, steeply NW-ward dipping Karadere Fault and one of the nodal planes of both mechanisms matches well the trend and dip of the Karadere Fault. The strike of the events further to the east coincides with the trend of the Düzce Fault except for event 28 being inclined by approximately 30◦. Seeber et al. (2000) observed that focal mechanisms in this area are highly diverse reflecting normal faulting as well as strike-slip mechanisms. They suggest that many of the aftershocks originate from secondary faults, straddling the volume between main strands. In our case, we did not observe any normal faulting or thrust event.

The seismic moment tensors of the 33 analysed events display significant differences in the percentage of the non-DC components for the three distinct fault segments (Figure 4.6). Events located in the Izmit-Sapanca and Karadere-Düzce segments exhibit only small percentages of the non-DC components and if existent they are mainly positive. The non-DC components are generally smaller than 10 per cent except for events 32 and 29 located in the Karadere-Düzce Segment with a non-DC content of 18 and 14 per cent, respectively. These values are still within or close to the error bounds derived in Stierle et al. (2014). Therefore, we conclude that these events might be even pure shear and the non-DC components are negligible. This correlates well with the predominant strike-slip stress regime along these segments and also with the main shock rupture being right-lateral strike-slip. In contrary, we found a substantial percentage of non-DC components for events below the Akyazi Plain where the Sapanca Fault splits into the Mudurnu and the Karadere faults. The observed non-DC components are entirely positive indicating a tensional regime and ranging from 20 to 48 per cent, clearly exceeding the defined error bounds found in the synthetic study (see Stierle et al. 2014). Furthermore it is notable that all tensile events occurred within 4 days approximately 2 weeks after the main shock, whereas the remaining events occurred 10–57 days after the main shock. Figure 4.7 shows a schematic sketch of the tectonic settings along the Akyazi Segment illustrating the interaction of the activated fault segments during the main shock. In this segment, the Sakarya and the Karadere faults slipped during the Izmit main shock with right-lateral motions. However, the observed distribution of surface displacement at the Sakarya Fault decreases linearly from over 5 m in the western part of the branch down to 0–0.1 m at the Akyazi strand (Langridge et al., 2002), whereas the observed right-lateral surface displacement at the Karadere Fault is generally much lower being 1–1.5 m and uniformly distributed along the fault. In between, there is a lack of surface displacement over more than 6 km. Consequently, a slip deficit of approximately 3.5 m was generated below the Akyazi Plain coseismically resulting in purely normal faulting aftershock activity with high aftershock energy release and a high potential for tensional source mechanisms. We clearly observe a substantial amount of non-DC components in the seismic moment tensors (Figure 4.6) related to tensile fracturing on pre-existing faults. We propose that the high amount of non-DC components is a strong indicator for extensional components in the source mechanism and, therefore, emphasizes the hypothesis of a tensional tectonic setting below the Akyazi Plain during the early post-seismic phase promoting large-scale fluid motion within the crust.

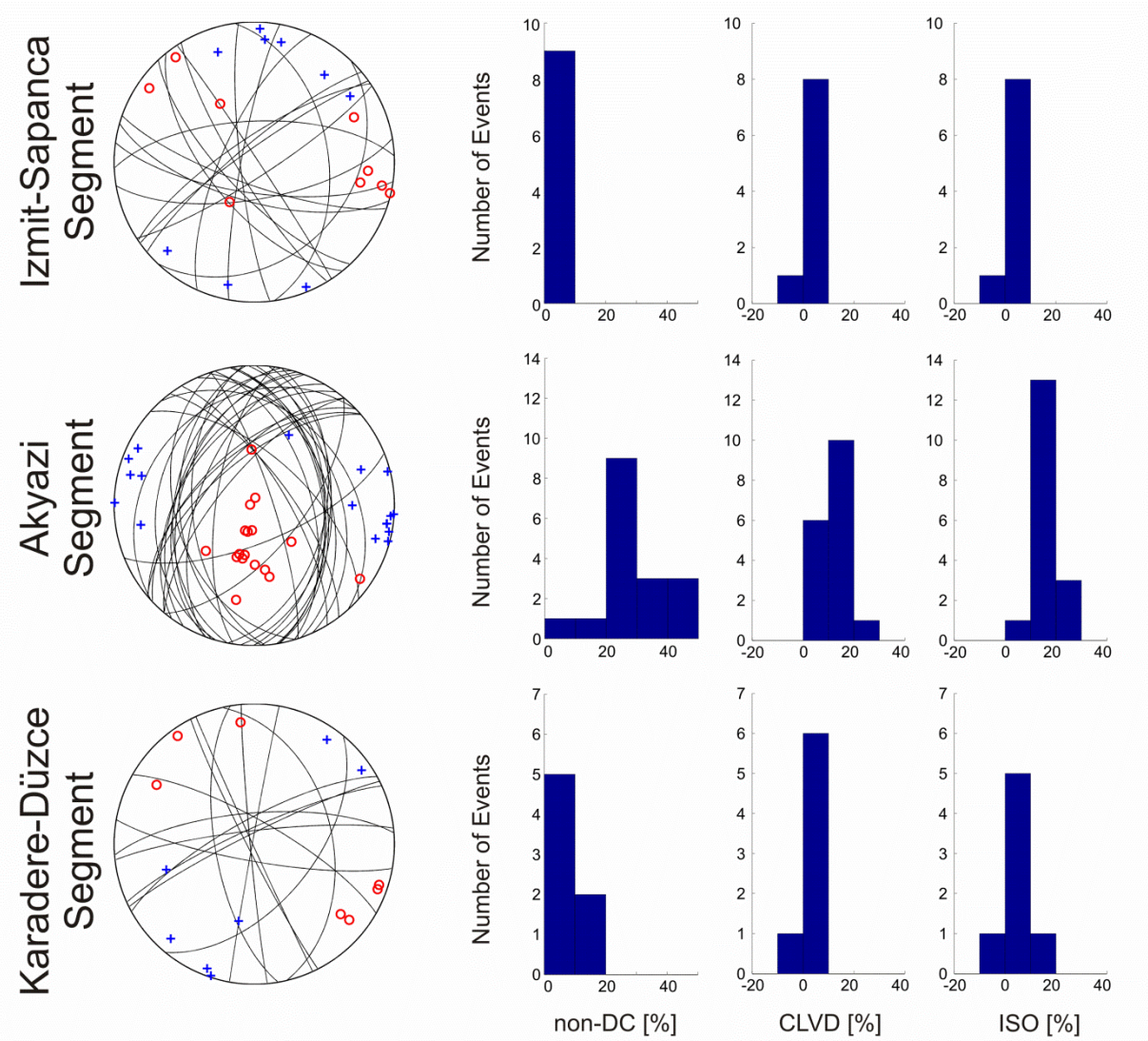

Figure 4.6: Moment tensors of the 33 selected aftershocks. *Left:* Nodal lines and P- and T-axes for events located in the respective segment. *Right*: Histograms of the non-DC, CLVD and ISO component observed in the corresponding segment.

Miller et al. (2004) found that large earthquakes can create potential liquid path by hydraulically connecting the upper crust at hydrostatic pore pressure with the lower crust at near lithosphere pore pressure. The increased fluid pressure triggered subsequent earthquakes and aftershocks by significantly reducing the effective normal stress on pre-existing faults. The subsequent flow is fast, high-pressured and propagates readily into the new fractures created by the main event thereby promoting tensile fracturing. Thus, this theory may provide a link between the large Izmit earthquakes, its tensile aftershocks and earthquake-triggered large-scale fluid flow. Roux & Ben-Zion (2013) further monitored the fault zone environment of the Düzce event with the correlation of earthquake waveforms. They observed a significant co-main shock change in correlation coefficients of groups of Düzce aftershocks, which indicates interplay between generation and healing of rock damage and permeability in the fault zone combined with a prominent fluid motion. We therefore find our observation of tensile fracturing in an extensional setting such as below the Akyazi Plain after the Izmit earthquake to be another indicator for a large-scale fluid motion in the crust to compensate the accumulated slip deficit.

Interestingly Hearn et al. (2009) observed even 2.5 years after the Izmit main shock a residual component of fault-normal (north– south) extension next to the Akyazi Plain at the Lake Sapanca using post-seismic deformation modelling techniques. They argue that coseismic reduction occurred in effective viscosity of lower crust and upper mantle causing the transfer of background tectonic stress to the upper crust and driving the observed extension on the long-term scale.

4.4 CONCLUSIONS

We studied potential non-DC components in aftershocks of the 1999 Izmit earthquake. To ensure high-quality data with good focal coverage, we applied strict quality criteria to the aftershock catalogue reducing the number of events from more than 10 000 to only 33 events for which stable moment tensors were obtained. Such a drastic reduction of events would not be necessary if broadband observations of earthquakes were available. While events along the Izmit-Sapanca and Karadere-Düzce segments host mostly strike-slip events with no or insignificant non-DC components, we identified EW-extensional normal faulting events with significant positive non-DC components of up to 48 per cent below the extensional Akyazi Plain. This observation is in accordance with the post-seismic setting following the Izmit main shock that left a remarkable slip deficit of 3.5 m below the Akyazi bend (Figure 4.7). We conclude that the tension throughout the seismogenic layer might have allowed fluids to migrate upwards thereby reducing effective normal traction or friction on coseismically stressed normal faults and accelerating the compensation of the slip deficit.

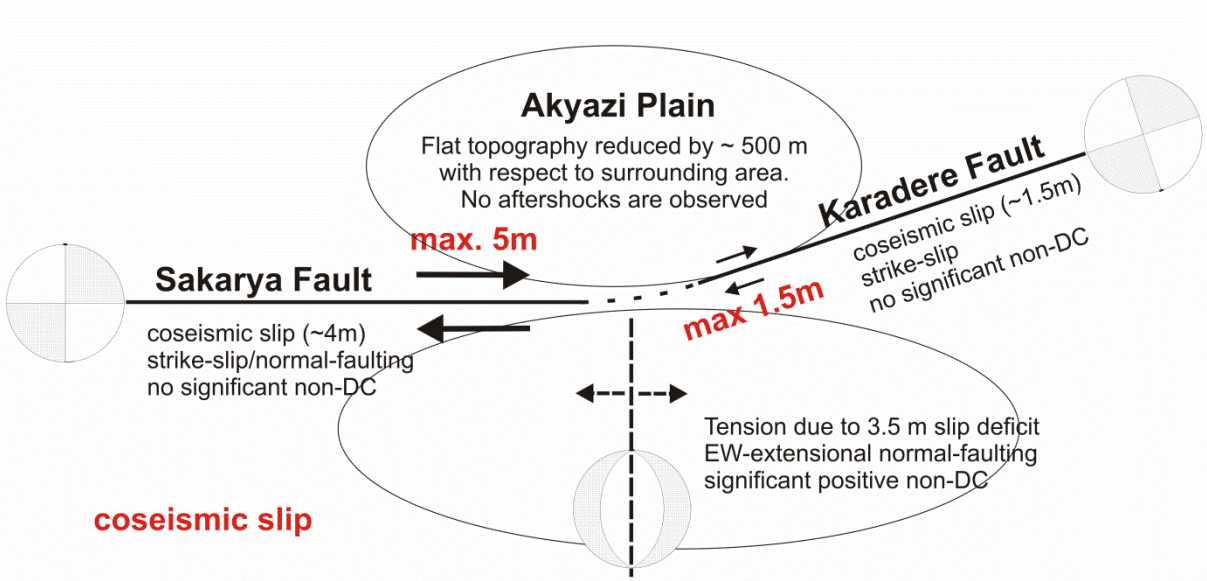

Figure 4.7: Schematic map view of the Akyazi Segment.

5 Seismic Moment Tensors of Acoustic Emissions Recorded During Laboratory Rock Deformation Experiments: Sensitivity to Attenuation and Anisotropy[3]

SUMMARY

This paper reports a new approach of moment tensor inversion of Acoustic Emissions (AEs) recorded during rock deformation experiments in the laboratory. The seismic moment tensors, widely used in earthquake seismology, can provide information on the size and orientation of fractures producing AEs and on the stress conditions in the sample. The moment tensor inversion of AEs is, however, a demanding procedure which requires carefully calibrated sensors and an accurate knowledge of the velocity model. In the standard moment tensor inversion in field experiments, the velocity model is usually isotropic and time independent. In laboratory experiments, the velocity model is, however, often anisotropic, attenuating and time dependent due to opening or closure of microcracks in the sample caused by loading. In this paper, we study the sensitivity of the moment tensor inversion to anisotropy of P-wave velocities and attenuation of the rock sample. We show that neglecting attenuation and anisotropy of P-wave velocities in the moment tensor inversion can produce significant uncertainties in the retrieved moment tensors and lead to misinterpretations of the source mechanisms. Interestingly, the sensitivity depends on the fracturing mode of AEs: the tensile events are more sensitive to anisotropy of the P-wave velocity and attenuation of the sample than the shear events. We show that geometry of faulting in anisotropic rock samples should be studied using the source tensors, since the P and T axes of the moment tensors are affected by anisotropy of the P-wave velocity and deviate from the true orientation of faulting. The stronger the anisotropy is, the higher the deviations are. Finally, we prove that the moment tensor inversion applied to a large dataset of AEs can be utilized to provide information on the attenuation parameters of the rock sample. The resolution of the method is high enough even for distinguishing anisotropic attenuation of P waves. The method is capable to measure differences between P-wave attenuation in the horizontal and vertical directions in the sample and allows detecting the effects of dilatant cracking according to the stress regime.

[3] This article has been submitted to be considered for publication in the Geophysical Journal International: E. Stierle, V. Vavryčuk, G. Kwiatek, E. Charalampidou, and M. Bohnhoff. Seismic moment Tensors of Acoustic Emissions During Laboratory Rock Deformation Experiments: Sensitivity to Attenuation and Anisotropy.

5.1 INTRODUCTION

During rock deformation experiments usually thousands of Acoustic Emissions (AEs) are recorded. They are caused by the radiated energy coming from micro fracturing inside the rock sample and display similar source mechanisms to natural earthquakes. The size of AEs is, however, different. AEs are much smaller and therefore radiate much higher frequencies. The rock deformation experiments in the laboratory are conducted under controlled boundary conditions in contrast to the deformation processes in the field scale. Therefore, AEs are an ideal tool for studying spatio-temporal generation and evolution of fractures and can substantially help in understanding earthquake nucleation and propagation. Since processing and evaluation of AE data is similar to those of earthquake observations, many methods developed in seismology have been successfully transferred to and adopted by AEs (Zang et al., 2000; Graham et al., 2010; Goebel et al., 2014; Charalampidou et al., 2015). Aside from accurate location of AE hypocentres it is also possible to determine fault-plane solutions, to construct and investigate the magnitude-frequency relation and to evaluate the b-value, or to perform spatial and temporal analysis of waveforms (Zang et al., 1998; Kwiatek et al., 2014b). The kinematics of source processes of AEs can be determined by means of the moment tensor inversion, which is widely used in earthquake seismology, and provides valuable information on the size and orientation of micro fractures producing AEs, the sense of displacement in micro-seismic source and ultimately the stress conditions in the sample.
First attempts to apply the moment tensor inversion to AE data were made in hydrofracture tests (Ohtsu, 1991) and in studies of fracture of concrete (Shigeishi & Ohtsu, 2001; Finck et al., 2003). Graham et al. (2010) further compared the moment tensor inversion with the polarity methods developed by Zang et al. (1998) and found a concurrent set of results from both methods, similar to what was also observed by Charalampidou et al. (2015). However, the moment tensor inversion provides more detailed information about the kinematic processes occurring in the seismic source. In particular, the potential occurrence of non-double-couple (non-DC) components of the moment tensors can provide information on type of fracturing and the physical properties of the rocks (Aker et al., 2014). The non-DC components comprise the isotropic (ISO) as well as the compensated linear vector dipole (CLVD) components (Vavryčuk, 2005).

The moment tensor inversion is a powerful tool. However, a concise application requires high-quality and well-calibrated data. For this reason, adequate laboratory experiments should be well designed and proper attention is required to determine the amplifications of the AE sensors and the coupling effects between the sensors and the rock specimen. Since measuring correct amplitudes is the key factor in determining accurate moment tensors, this issue should be addressed and solved in all studies of AEs involving moment tensor inversions. Recently, two new approaches for the sensor calibration were proposed by (Davi & Vavryčuk, 2012) and Kwiatek et al. (2014a). The method by Davi and Vavryčuk (2012) and Davi et al. (2013) is based on a joint inversion of a family of seismic events for their moment tensors and for sensor amplifications. Kwiatek et al. (2014a) use ultrasonic transmission data for assessing the coupling and the sensitivity of the AE sensors as a function of the incidence angle of each ray. Both methods have proven to be efficient in determining or correcting for the sensor amplifications in order to retrieve highly accurate moment tensors.

Progressive deformation in rock samples results in changes in P-wave velocities and attenuation, as this is revealed by continuous measurements of the P-wave velocities and amplitudes (Stanchits et al., 2006; Hamiel et al., 2009). This stress-induced attenuation and

velocity anisotropy increases with increasing differential stress and is generated by the crack formation. If anisotropy is neglected, the moment tensors are less accurate and can be wrongly interpreted (Šílený & Vavryčuk, 2000, 2002). For example, shear faulting on planar faults produces DC moment tensors in isotropic media, but apparent non-DC moment tensors may be obtained in anisotropic media (Vavryčuk, 2015b). The amount of the ISO and CLVD components depends on the strength and symmetry of anisotropy and on the orientation of faulting. The complexity of moment tensors in anisotropic media prevents their direct interpretation, and the decomposition of moment tensors must be substituted by that of the source tensors (Vavryčuk, 2015b), which are directly related to the geometry of faulting.

In this study, we present a new method, that allows for accounting for the P-wave velocity and attenuation anisotropy is considered in the moment tensor inversion. Based on moment tensor inversion techniques we further develop a method for deriving the attenuation parameters of the medium. This approach is based on a joint inversion of a set of AE events for their moment tensors and for the P-wave attenuation anisotropy of the sample. The method is tested on synthetic data and then it is applied to AEs. The AE data were obtained during a triaxial compression experiment on a granite sample described in Stanchits et al. (2006). The retrieved attenuation anisotropy is compared with that measured using the ultrasonic data. Finally, the moment tensors are used for calculating the source tensors, and the DC and non-DC components of the source tensors are interpreted.

5.2 THEORY

5.2.2 MOMENT TENSOR INVERSION

Displacement **u** generated by a seismic point source is calculated using the representation theorem

$$u_i = M_{kl} * G_{ik,l} \tag{5.1}$$

where $M_{kl} = M_{kl}(t)$ is the seismic moment tensor, $G_{ik,l}$ is spatial derivative of the Green's tensor amplitudes, and symbol '*' means the time convolution. Since we invert amplitudes, the convolution integral in equation 5.1 reduces to multiplication and the moment tensor is obtained as (Lay & Wallace, 1995):

$$\mathbf{m} = \mathbf{G}^{-g}\mathbf{u} \text{ with } \mathbf{G}^{-g} = \left[\mathbf{G}^T\mathbf{G}\right]^{-1}\mathbf{G}^T \ , \tag{5.2}$$

where $\mathbf{G}^{-g}$ means the generalized linear inversion of **G**. The matrix **G** is the *N*x6 matrix of the spatial derivatives of the Green's function amplitudes,

$$\mathbf{G} = \begin{bmatrix} G_1^{(1)} & G_2^{(1)} & G_3^{(1)} & G_4^{(1)} & G_5^{(1)} & G_6^{(1)} \\ G_1^{(2)} & G_2^{(2)} & G_3^{(2)} & G_4^{(2)} & G_5^{(2)} & G_6^{(2)} \\ \cdots & \cdots & \cdots & \cdots & \cdots & \cdots \\ G_1^{(N)} & G_2^{(N)} & G_3^{(N)} & G_4^{(N)} & G_5^{(N)} & G_6^{(N)} \end{bmatrix}, \tag{5.3}$$

m is the moment vector composed of 6 components of moment tensor **M**,

$$\mathbf{m} = \left[M_{11} \quad M_{22} \quad M_{33} \quad M_{23} \quad M_{13} \quad M_{12} \right]^T, \tag{5.4}$$

and **u** is the vector of amplitudes observed at *N* sensors,

$$\mathbf{u} = \left[u^{(1)} \quad u^{(2)} \quad \ldots \quad u^{(N)} \right]^T. \tag{5.5}$$

The spatial derivatives of the Green's function $G_l^{(i)}$ are calculated for the *i*th sensor in the following way:

$$\begin{gathered} G_1 = g_{1,1},\ G_2 = g_{2,2},\ G_3 = g_{3,3}, \\ G_4 = g_{2,3}+g_{3,2},\ G_5 = g_{1,3}+g_{3,1},\ G_6 = g_{1,2}+g_{2,1} \end{gathered} \tag{5.6}$$

where g_k is the synthetic amplitude generated by the point force directed along the x_k axis. The amplitude is calculated for the direction along the sensor axis. The superscript (i) identifying the sensor is omitted in equation 5.6.

5.2.3 Green's Function in Homogeneous Anisotropic Attenuating Media

In order to determine moment tensor **M** using equation 5.2, we have to know the Green's function and particularly its spatial derivative $G_{ik,l}$. For anisotropic attenuating media, the Green's function can be calculated using a model of viscoelastic anisotropy. This model describes jointly velocity anisotropy and attenuation by introducing complex-valued, frequency-dependent, viscoelastic parameters (Auld, 1973; Carcione, 2007; Vavryčuk, 2007a, 2007c, 2015a). The real part of the parameters controls the propagation velocity and their imaginary part controls the wave attenuation. All formulas for wave quantities in viscoelastic media are formally identical as in elastic media except for being complex.

The Green's function in homogeneous anisotropic viscoelastic media reads (Vavryčuk, 2007c):

$$G_{kl}(\mathbf{x},\omega) = \frac{1}{4\pi\rho} \frac{g_k g_l}{v\sqrt{|K|}} \frac{1}{r} \exp\left(i\sigma_0 + i\omega \mathbf{p}_0 \cdot \mathbf{x}\right), \tag{5.7}$$

and its spatial derivative is (Vavryčuk, 2007c):

$$\frac{\partial}{x_m} G_{kl}(\mathbf{x},\omega) = \frac{i\omega}{4\pi\rho} \frac{g_k g_l p_{0m}}{v\sqrt{|K|}} \frac{1}{r} \exp\left(i\sigma_0 + i\omega \mathbf{p}_0 \cdot \mathbf{x}\right), \tag{5.8}$$

where

$$\sigma_0 = -\frac{1}{2}(\varphi_1 + \varphi_2), \quad -\frac{3}{2}\pi \le \varphi_1 < \frac{1}{2}\pi, \quad -\frac{3}{2}\pi \le \varphi_2 < \frac{1}{2}\pi$$

and $\mathbf{p}_0$ is the stationary slowness vector (see Vavryčuk, 2007a, 2007c). Quantity $K = K_1K_2$ is the Gaussian curvature of the slowness surface, $K1$ and $K2$ are the principal curvatures, and

$\varphi_1$and φ_2 are their phase angles. All quantities dependent on p in equations 5.7 and 5.8 are taken at stationary point $\mathbf{p}_0$. Position vector $\mathbf{x} = r\mathbf{N}$, distance r, ray vector N, frequency ω, phase angles $\varphi_1$and φ_2, and density ρ are real-valued; but polarization vector g, Gaussian curvature K, principal curvatures $K1$ and $K2$, energy velocity v and slowness vector $\mathbf{p}_0$ are complex-valued.

5.2.4 *Elliptic Viscoelastic Anisotropy*

The wave quantities in equations 5.7 and 5.8 depend generally on 21 complex-valued viscoelastic parameters. If we assume P waves propagating in an elliptic viscoelastic anisotropy media, the problem is simplified and we can parameterize the medium just by two complex-valued density-normalized viscoelastic parameters a_{11} and a_{33}. The stationary slowness vector $\mathbf{p}_0$, energy velocity vector $\mathbf{v}$ and the Gaussian curvature of the slowness surface K can be expressed as follows (Vavryčuk & Yomogida, 1996):

$$\mathbf{p} = \frac{1}{\sqrt{a_{33}N_1^2 + a_{33}N_2^2 + a_{11}N_3^2}} \left[N_1 \frac{a_{33}}{a_{11}},\, N_2 \frac{a_{33}}{a_{11}},\, N_3 \frac{a_{11}}{a_{33}} \right]^T, \tag{5.9}$$

$$\mathbf{v} = \left[a_{11}p_1,\, a_{11}p_2,\, a_{33}p_3 \right]^T, \tag{5.10}$$

$$K = \frac{a_{11}^2 a_{33}}{v^4} \left[a_{11}p_1,\, a_{11}p_2,\, a_{33}p_3 \right]^T, \tag{5.11}$$

where subscript 0 at slowness vector $\mathbf{p}$ is for simplicity omitted, $\mathbf{N}$ is the real ray direction vector and v is the complex energy velocity calculated as

$$v = \sqrt{v_i v_i}\,. \tag{5.12}$$

For simplicity the polarization vector of direct P waves is identified with the ray direction. The information on phase σ_0 is not important, because we will not analyse phase shifts but only the amplitudes of direct P waves.

Hence, we succeeded in expressing all needed wave quantities using real ray direction N and two complex parameters a_{11} and a_{33} describing the elliptic anisotropy. These parameters can be determined in a laboratory experiment from measurements of propagation velocities and Q-factors (or attenuations) in the horizontal and vertical directions of the medium. Since the ray and phase quantities (velocities and Q-factors) coincide in the horizontal and vertical directions in the elliptic anisotropy, the complex viscoelastic parameters a_{11} and a_{33} can be calculated from real ray velocities Vv and V_H, and ray Q-factors Q_V and Q_H as follows (see Vavryčuk, 2015a, his equation 21):

$$a_{11} = V_H^2 \left(1 - \frac{i}{Q_H} \right), \quad a_{33} = V_V^2 \left(1 - \frac{i}{Q_V} \right). \tag{5.13}$$

The vertical and horizontal *Q*-factors can be determined from measurements of the horizontal and vertical attenuations A_H and A_V, which control amplitude decay of waves along the vertical and horizontal rays (Vavryčuk, 2008, his equations 51 and 59)

$$Q_H = \frac{1}{2A_H V_H}, \quad Q_V = \frac{1}{2A_V V_V}. \tag{5.14}$$

5.2.5 Moment and Source Tensors

A straightforward interpretation of moment tensors in terms of the faulting geometry in the source is possible in isotropic media only. In anisotropic media the problem is more complicated. The moment tensor of a fracture source is affected not only by the geometry of faulting but also by the properties of the material in the focal zone. Depending on these properties, the moment tensors can take a general form with non-zero isotropic (ISO), double-couple (DC) and compensated linear vector dipole (CLVD) components even for simple shear faulting on a planar fault (Vavryčuk, 2004, 2015a). For this reason, physical interpretations of AEs (i.e., shear-tensile dislocation sources) in anisotropic media should be based on the decomposition of the source tensor. The source tensor is directly related to the geometry of the fracture at the source, while the moment tensor represents stresses involved in this fracturing (Ben-Zion, 2003; Vavryčuk, 2005):

$$D_{kl} = \frac{uS}{2}\left(s_k n_l + s_l n_k\right), \tag{5.15}$$

and

$$M_{ij} = c_{ijkl} D_{kl}, \tag{5.16}$$

where unit vectors **n** and **s** denote the crack normal and the direction of the slip vector, *u* is the slip, *S* is the crack size, and c_{ijkl} are elastic parameters describing an anisotropic medium. In an isotropic medium, equation 5.2 reads:

$$M_{ij} = \lambda D_{kk}\delta_{ij} + 2\mu D_{ij}, \tag{5.17}$$

where λ and μ are the Lame's parameters. While the source and moment tensors diagonalize in anisotropic media in different systems of eigenvectors and thus their relation is complicated, the eigenvectors of the source and moment tensors are the same in isotropic media.

5.3 Setup of the Experiment

We analyse AE data obtained by Stanchits et al. (2006) during triaxial compression experiments on a granite sample in the laboratory. Here, we present the main parts of the experiment that are relevant to our study. A more explicit description of this experiment can be found in Stanchits et al. (2006). The cylindrical sample (diameter 50 mm, length 100 mm) was subjected to three differential stress cycles at decreasing confining pressure of 60, 40

and 20 MPa, respectively. During the lower confining pressure cycle the sample was loaded up to the macroscopic failure, while during the two previous stress cycles the sample was loaded up to a maximum differential stress of 500 MPa. AE activity and velocity changes were monitored throughout the experiments by twelve P-wave and eight S-wave piezoelectric sensors (Figure 5.1) with a sampling frequency of 10 MHz. In our study, we analysed the P-wave data only, since the S-wave data were complex being contaminated by strong coda waves. The axial loading rate was servo-controlled using the AE control. For periodic elastic P-wave velocity measurements, six P-sensors and four S-sensors were used as emitters by applying 100 V pulses every 30–40 seconds during loading and the remaining sensors were recording the transmitted signals. Two pairs of strain gages were glued directly onto the sample surface for calculating the volumetric strain (global measurement). The ultrasonic measurements confirmed that the observed P-wave velocity was highly anisotropic and time dependent. It displayed a strong decrease in the horizontal direction with respect to the vertical direction while the axial loading was increasing (Figure 5.2). Furthermore, Stanchits et al. (2006) distinguished between the T- (tensile), C- (compaction) and S-type (shear) events according to the observed polarities of the P waves. With increasing axial stress T-type events are dominant and close to failure S-type events become increasingly important.

Herein, we present results for the differential stress loading cycle at 40 MPa confining pressure. During this loading cycle, the rock sample remained homogeneous and was only weakly damaged. Consequently, the P-wave velocity field was not too disturbed by fractures existing/generated in the rock. Nevertheless, the strength of anisotropy caused by deformation was sufficiently high to produce detectable effects in the wave field. When

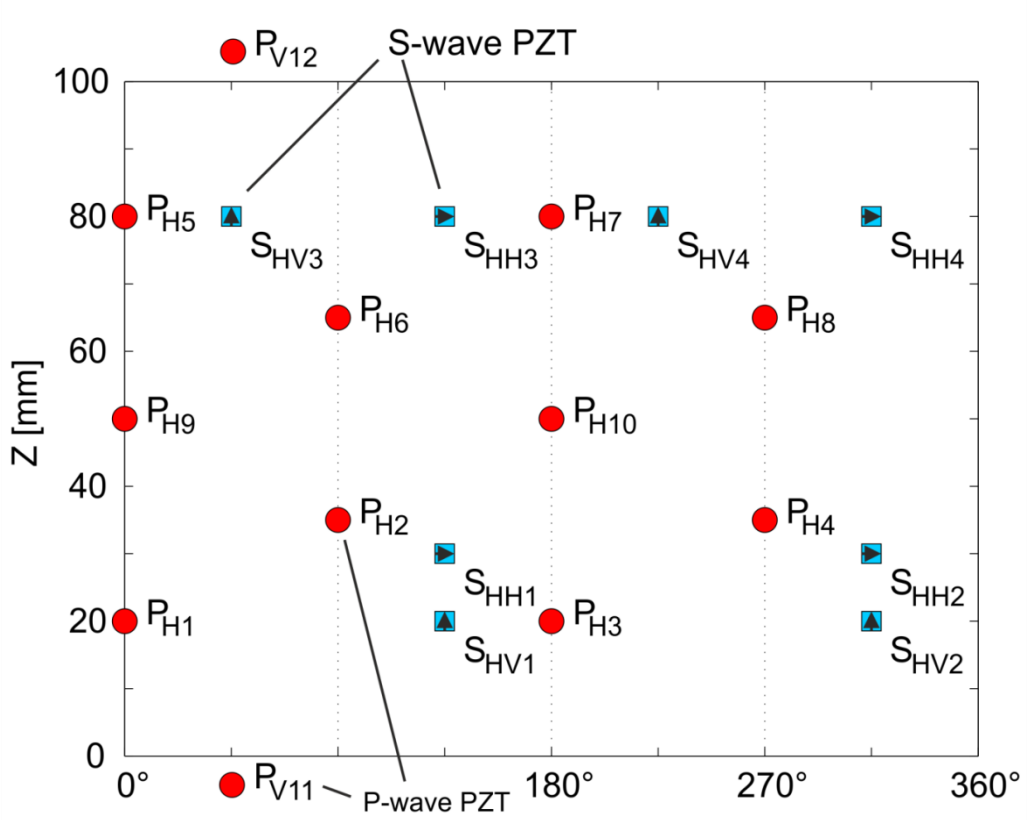

Figure 5.1: Projected sample surface showing the position of 20 ultrasonic sensors. PH and PV are piezoelectric sensors measuring P-wave velocity in horizontal and vertical directions. SHH are shear sensors polarized in horizontal direction, SHV are shear sensors polarized in vertical direction.

loading came to macroscopic failure at a stress loading cycle at 20 MPa, the rock sample became highly damaged and inhomogeneous. The complex structure with extensive fracture systems produced a complicated scattered wave field difficult to be interpreted and inverted for moment tensors.

Stanchits et al. (2003, their equation 3) presented an equation for determining the P-wave attenuation from ultrasonic measurements of the P-wave amplitudes. We applied this method to ultrasonic transmission data and derived the attenuations in vertical and horizontal directions in the sample. We selected sensors PV11 and PV12 for estimating the vertical attenuation and sensors PH9 and PH10 for estimating the horizontal attenuation (Figure 5.1). The measurements do not allow estimating absolute values of attenuation. However, we were able to determine the temporal evolution of the relative values of

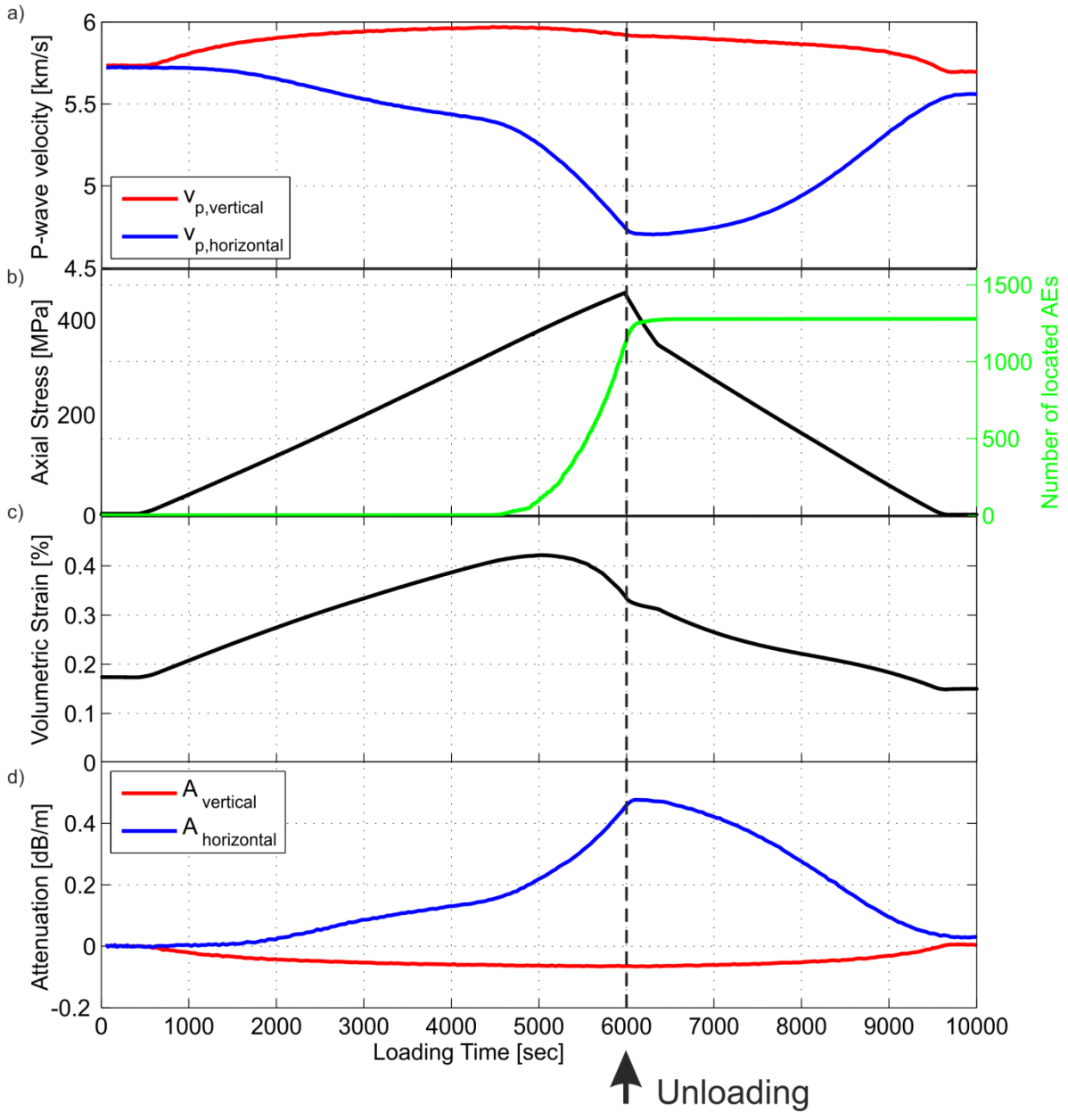

Figure 5.2 Vertical (measured by sensor 11-12) and horizontal (measured by sensor 9-10) P-wave velocities (a), applied axial stress and acoustic emission rate (b), and volumetric strain (c) obtained by Stanchits et al. (2006). Plot (d) shows the relative horizontal (measured by sensor 9-10) and vertical (measured by sensor 11-12) attenuation derived from ultrasonic transmission data after Stanchits et al. (2003, their equation 3).

attenuation from repeating measurements. The vertical attenuation (parallel to maximum compression) was decreasing due to the closure of the horizontal micro cracks and the compacted pore space, while the horizontal attenuation was increasing due to the opening of vertically oriented, dilatant micro cracks (Figure 5.2d).

5.4 Synthetic Tests

5.4.2 Sensor Configuration and Model of the Medium

We performed synthetic tests of the sensitivity of moment tensor solutions of AEs to anisotropy of P-wave velocity and attenuation. The P-wave velocity model, the sensor configuration and the AE event locations were retrieved from the laboratory experiment (Figure 5.1 and Figure 5.2). We selected a subset of 429 events, all located in the centre of the sample, to ensure good azimuthal coverage of sensors on the focal sphere (Figure 5.3b). Synthetic amplitudes were determined for the P waves only. The amplitudes of the P-wave Green's function were calculated according to Section 5.2.3 assuming a time-dependent elliptic anisotropy model with horizontal and vertical velocities shown in Figure 5.2a. The horizontal attenuation parameter (equation 5.14) is set to be higher (0.019) while the vertical is lower (0.0009) according to the ultrasonic measurements performed in the real experiment (Figure 5.2d).

In order to test the sensitivity of the retrieved moment and source tensors to anisotropy and attenuation of the medium, we additionally run the inversion assuming two other types of the medium. First, we assumed a viscoelastic isotropic medium. We modified the viscoelastic anisotropic model by neglecting the velocity anisotropy and assumed a constant directionally independent P-wave velocity of 5.2 km/s. Second, we assumed an

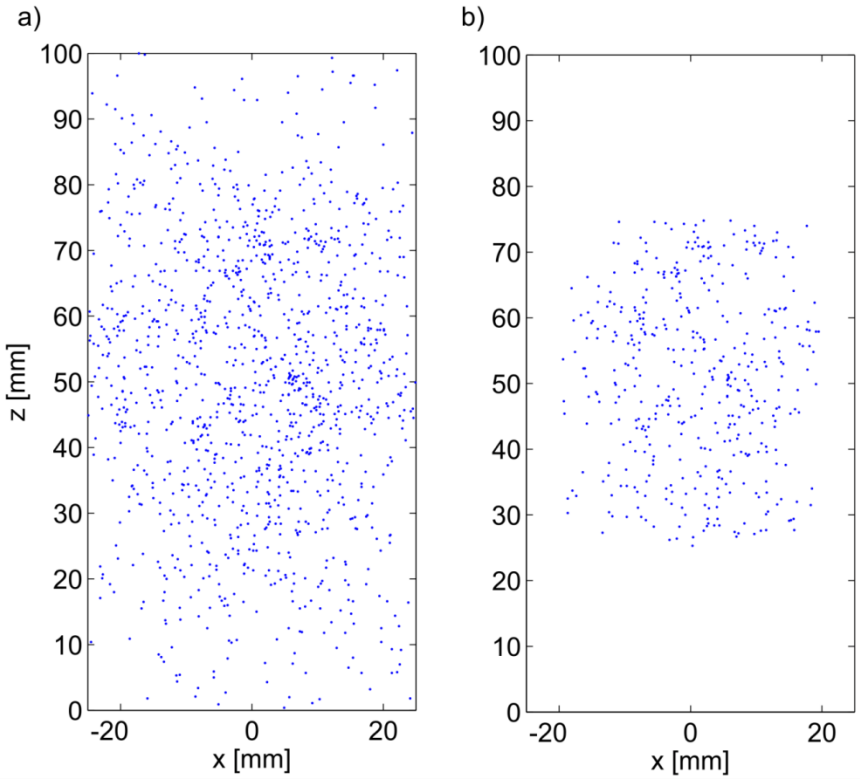

Figure 5.3: AE event locations plotted in the x-z perpendicular projection: a) all 1278 events; b) selected subset of 429 events, covering the mid-height of the sample.

elastic anisotropic medium. In this case, the viscoelastic anisotropic model was modified by neglecting attenuation and the parameters of the velocity anisotropy remained unchanged.

The AE sources were calculated using the shear-tensile source model (Vavryčuk, 2011). This model assumes that cracks are opening or closing during fracturing. The inclination of the slip vector from the plane of a crack is called the slope angle. It is positive for tensile events and negative for compressive events. We setup two datasets: one contains pure shear events and the other pure tensile events. To model the source mechanisms representative for the triaxial loading experiments we chose dips in the range from 30° to 60°, rakes in the range from -120° to -60° and random strikes. The slope angle is 0° for shear events and between 25° and 26° for tensile events. The non-DC content of moment tensors of tensile events is about 60%. The synthetic P-wave amplitudes at each sensor were calculated from prescribed moment tensor **M** and the spatial derivatives of the Green's function **G** using equation 5.1. The synthetic amplitudes served as the input data for the moment tensor inversion (see Section 5.2.2).

5.4.3 Analysis of Shear AEs

We started with analysing the dataset containing pure shear events. The P-wave amplitudes were inverted for the moment and source tensors and Figure 5.4 shows the results assuming the viscoelastic anisotropic medium (a), the viscoelastic isotropic medium (b), and the elastic anisotropic medium (c). The results are represented by the distribution of the P and T axes and the non-DC components (ISO and CLVD). To assess the quality of the retrieved moment tensors the normalized root-mean-square (RMS) error between theoretical and observed amplitudes is determined using the following formula:

$$RMS = \frac{\sqrt{\sum_{i=1}^{N}\left(A_i^{obs} - A_i^{theo}\right)^2}}{\sqrt{\sum_{i=1}^{N}\left(A_i^{obs}\right)^2}}, \qquad \textbf{5.18}$$

where A_{obs} and A_{theo} are the observed and theoretical amplitudes, respectively, subscript i is the sequential number of the station, and N is the total number of stations at which the amplitudes were recorded for the respective event. The root-mean-squares (RMS) between the synthetic and inverted P-wave amplitudes for each inversion are shown in Figure 5.5a and b.

Figure 5.4a shows the results if the true anisotropic viscoelastic medium is assumed in the inversion. As expected, the inversion yields correct results and the RMS is zero. The P and T axes derived from the source tensors correspond to true geometry of faulting. In general, we found that the P and T axes derived from the source and moment tensors are similar and thus the orientation of faulting is described adequately by both tensors regardless of the velocity and attenuation model considered in the inversion. However, the content of the non-DC components for both tensors is different. Since we modelled pure shear events, the non-DC components of the source tensors are zero as shown in Figure 5.4a. But the moment tensors contain non-DC components up to 55% related to the velocity and attenuation anisotropy in the focal zone. This can lead to misinterpretations of the source mechanisms, if the effect of anisotropy is not known.

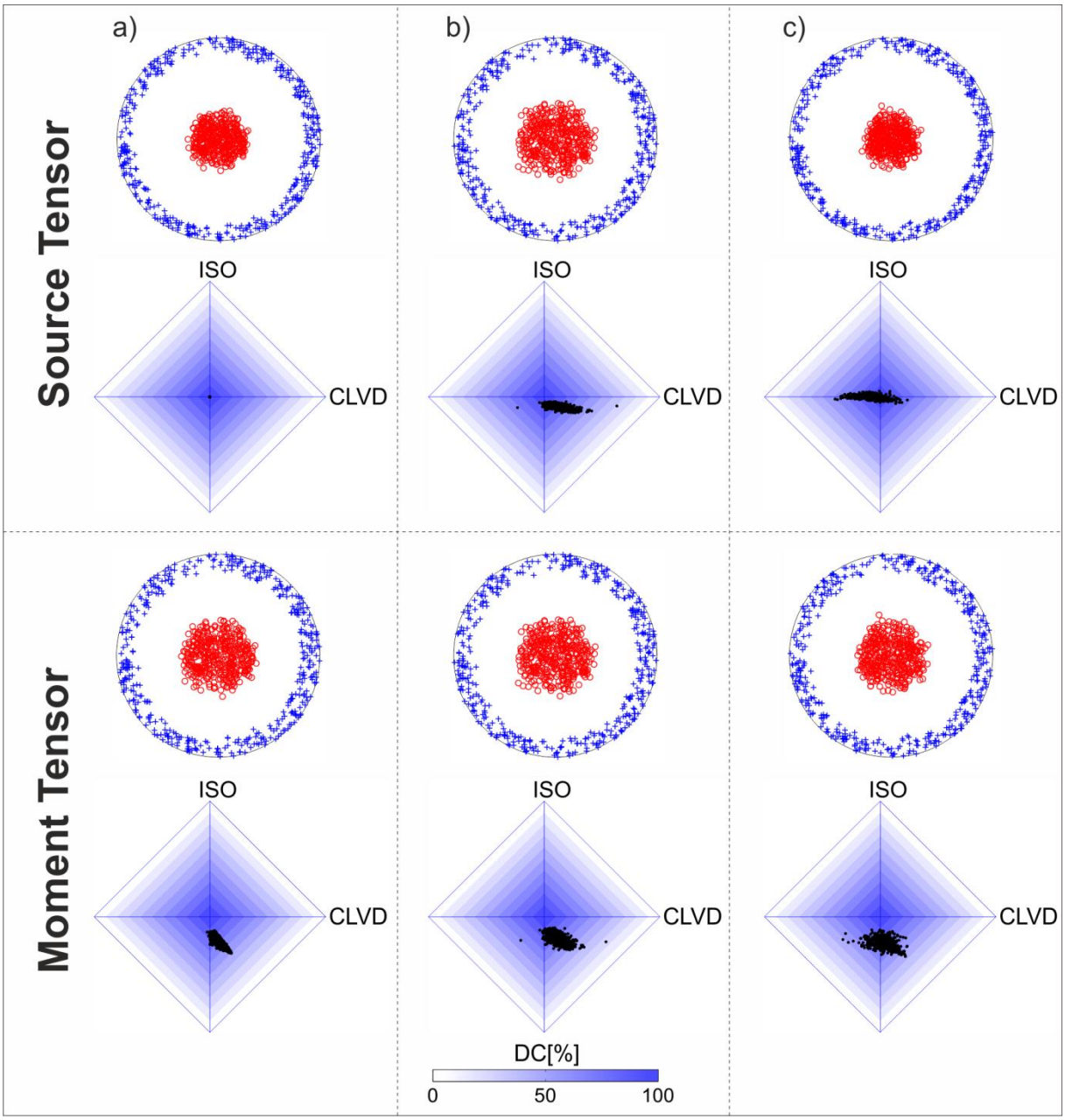

Figure 5.4: Synthetic tests simulating pure shear AE events in anisotropic viscoelastic media: the P axes (red circles) and T axes (blue plus signs) and non-DC components for source and moment tensors obtained in the viscoelastic anisotropic medium (a), the viscoelastic isotropic medium (b), and the elastic anisotropic medium (c).

If anisotropy is neglected (Figure 5.4b), the non-DC components become also present in the source tensors being produced by the velocity mismodelling. Here, especially the CLVD component is affected and the errors are about three times larger than those of the ISO component. Both types of tensors reveal negative ISO and positive CLVD components. The RMS and the non-DC components are increasing with time, because anisotropy is increasing with time and the assumption of an isotropic medium becomes incorrect (Figure 5.5a). Similar results are obtained when the attenuation is neglected in the inversion (Figure 5.4c). The ISO components of the source tensors are close to zero, which is the true value of modelled source mechanisms. But the CLVD components are mostly negative and reach values up to -45%. In contrary, the CLVD components of the moment tensors are close to zero, but the ISO components are negative and reach values up to -45%.

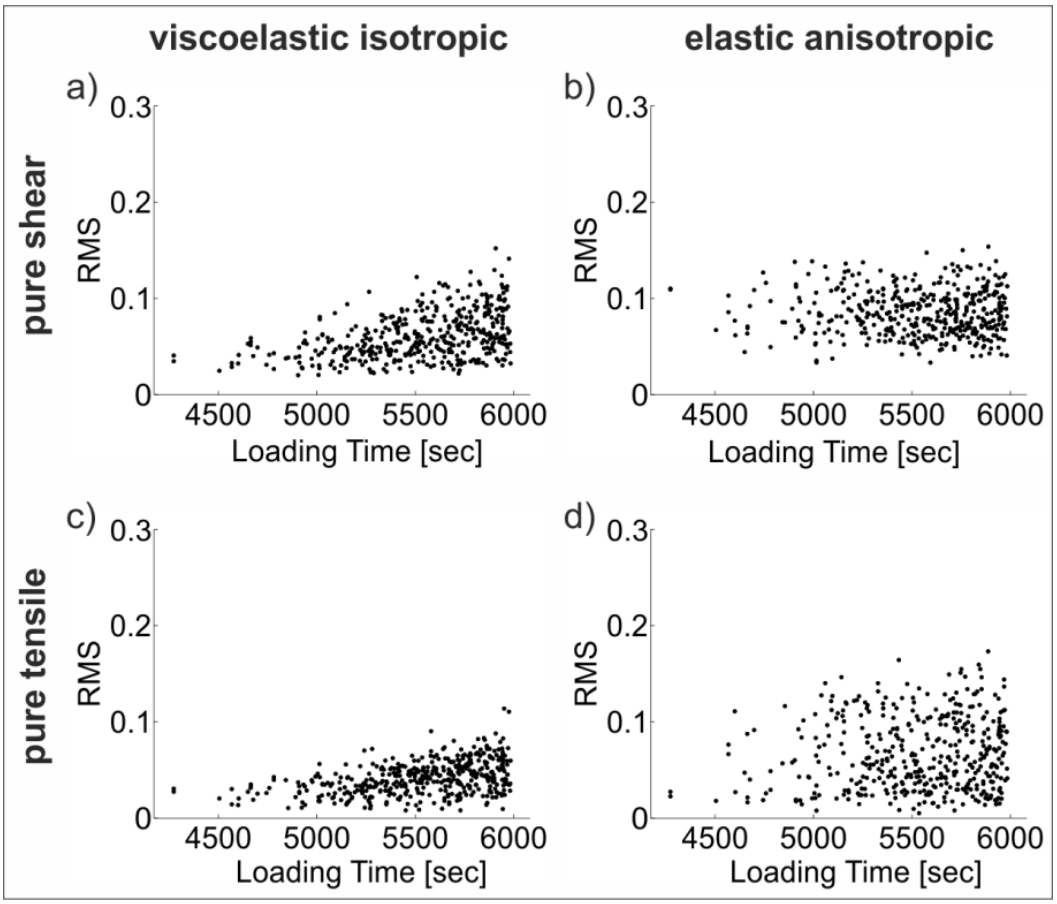

Figure 5.5: Root-mean-square (RMS) values of the moment tensor inversion of synthetic AE data with different source mechanisms (pure shear (a,b) and pure tensile (c,d)) simulating errors in the velocity and attenuation parameters of the medium: assuming the viscoelastic isotropic medium (a,c) and the elastic anisotropic media (b,d).

5.4.4 Analysis of Tensile AEs

In the second part of the synthetic tests, we analysed a dataset of tensile events with non-DC components of 60% (20% of ISO and 40% of CLVD). Analogously to the tests of shear events, Figure 5.6 shows the moment and source tensors in viscoelastic anisotropic media (a), viscoelastic isotropic media (b) and in elastic anisotropic media (c). Again, the source tensors in Figure 5.6a represents the true faulting geometry of the modelled events. The distribution of P and T axes shows that moment tensors of tensile events are more sensitive to anisotropy than those of shear events. The P and T axes of the moment tensors are remarkably different from those of the source tensors and thus they cannot be easily interpreted in terms of geometry of faulting.

If the P-wave amplitudes are inverted assuming the isotropic velocity model, the clustering of the P and T axes of the source tensors is lost due to velocity mismodelling (Figure 5.6b). The uncertainties are significantly high and the interpretation of faulting parameters from the source tensors becomes impossible. In contrary, the influence of the attenuation model on the directions of the P and T axes of the source tensors is minor (Figure 5.6c). Their deviations from the original directions are negligibly small. Since the true orientation of faulting cannot be derived from moment tensors of tensile events even if the true medium is assumed, it is difficult to quantify mismodelling errors. However, we observe that the scattering (especially of P axes) is even higher when anisotropy is neglected in the inversion.

Focussing on the non-DC components, the sensitivity to the velocity model as well as to attenuation is similar in both types of tensors. The non-DC components are shifted and more scattered. Especially, the CLVD component is affected by mismodelling of the medium, because the errors are about three times larger than those of the ISO (Figure 5.6b and c). In general, the sensitivity of the non-DC components of tensile events is comparable to that of shear events

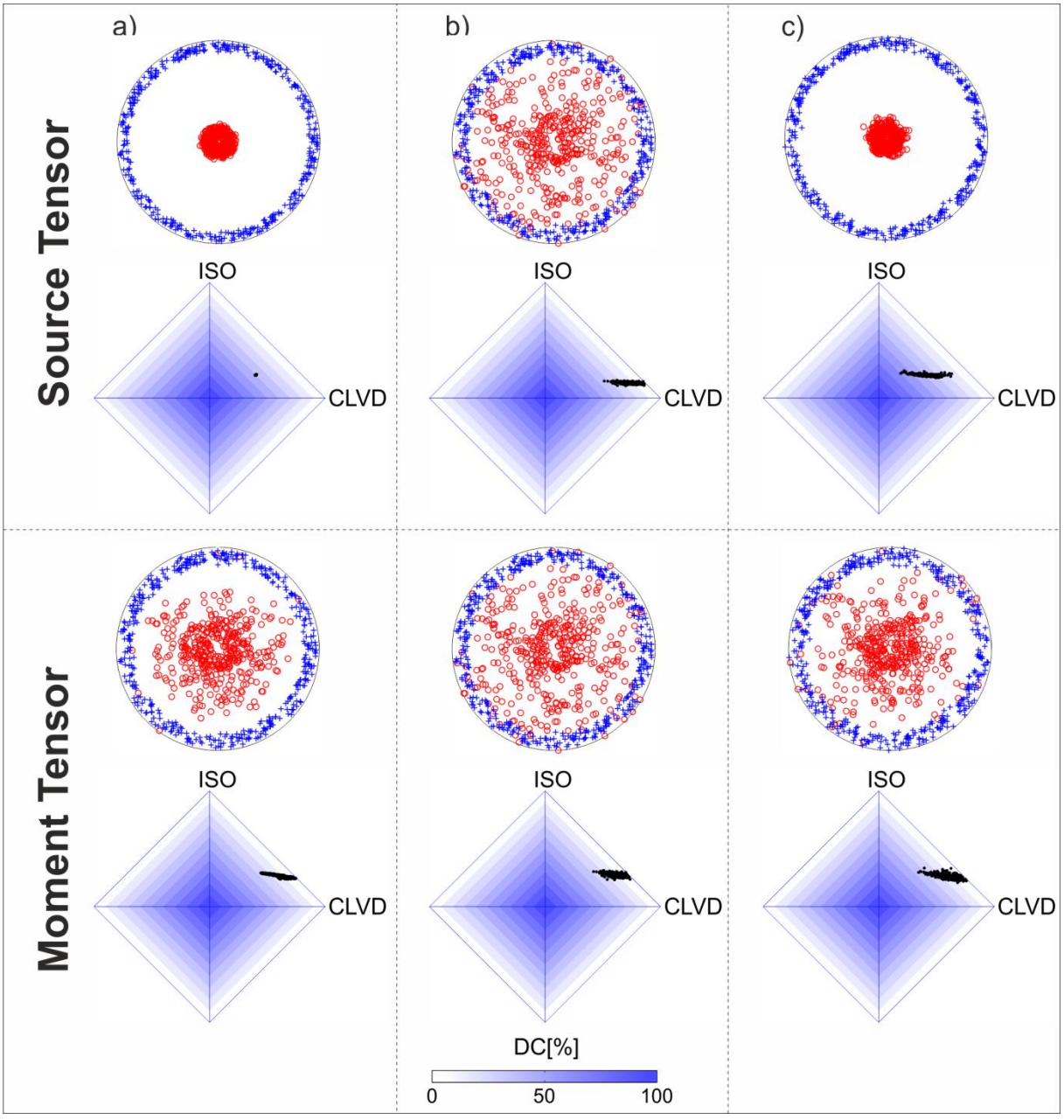

Figure 5.6: Synthetic tests simulating tensile AE events in anisotropic viscoelastic media, where the slope angle is ranging from 0 to 25°: the P axes (red circles) and T axes (blue plus signs) and non-DC components for moment and source tensors obtained in the viscoelastic anisotropic medium (a), the viscoelastic isotropic medium (b), and the elastic anisotropic medium (c).

5.4.5 *Inversion for Anisotropic Attenuation*

We inverted a set of synthetic tensile events for attenuation of the medium. We inverted the data repeatedly with various values of attenuations and studied the behaviour of the average RMS of the total dataset. The optimum attenuation parameters have been found by minimizing the RMS in a grid search scheme. The synthetic dataset was created analogously to the previous datasets, except for the value of the slope angle, which describes the shear-tensile source model. While the slope angle was zero for pure shear events and 90° for pure tensile events, here the slope angle ranged from -10° to 25°. These values were found for the AE data in the laboratory. The true vertical attenuation parameter was 0.0034 and the horizontal parameter was 0.0056. To simulate realistic observations of AEs we contaminated synthetic amplitudes with uniformly distributed, random noise with a noise level up to 30% of the amplitude at the respective sensor. The results of the inversion are shown in Figure 5.7. The RMS function is smooth ranging between 0.069 and 0.348. The minimum RMS is found for a vertical attenuation parameter of 0.0032 and for a horizontal attenuation parameter of 0.0058. A good correspondence of the results with the true values indicates that the inversion is sufficiently robust and thus applicable to real observations.

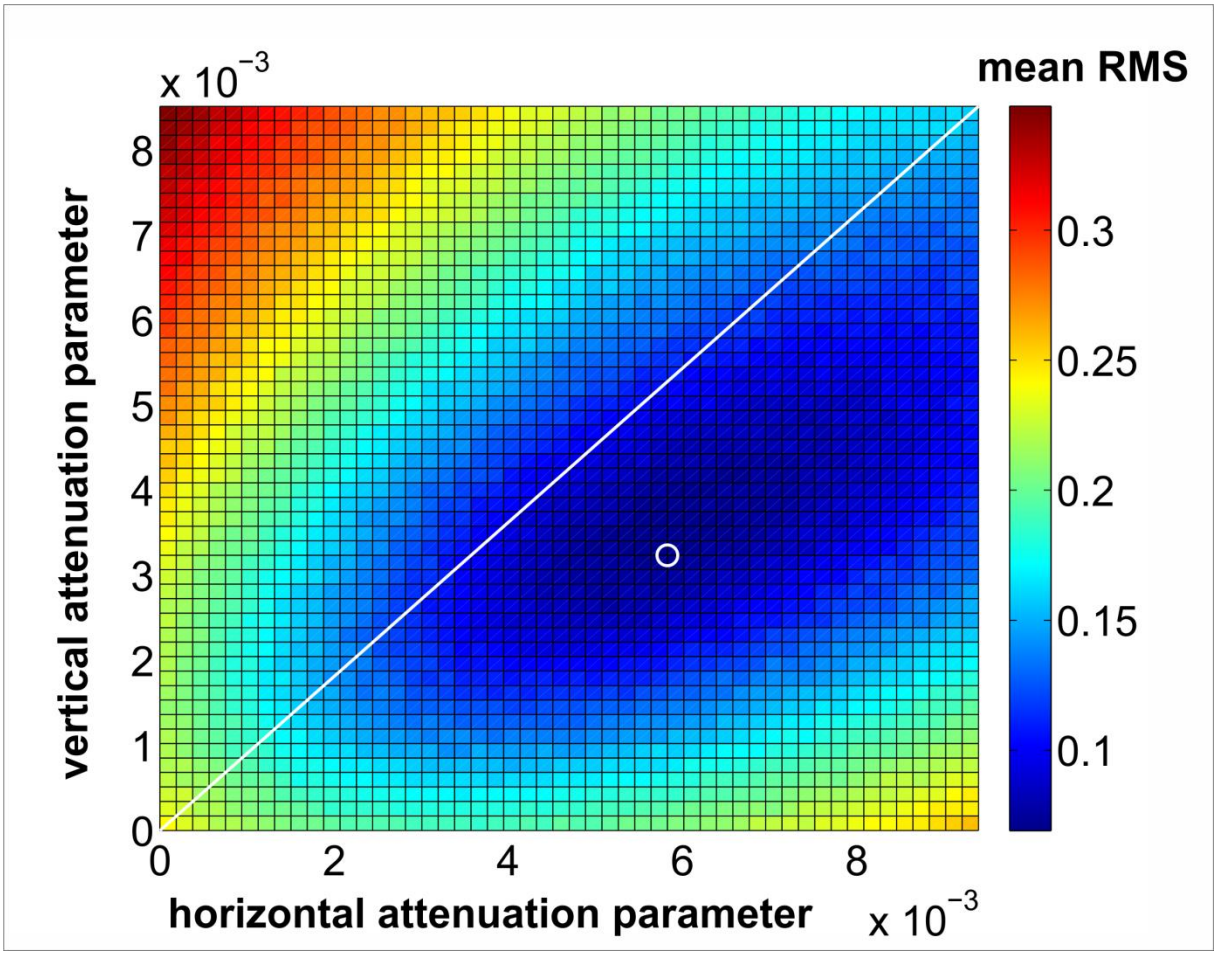

Figure 5.7: Synthetic test of the inversion for anisotropic attenuation. The mean RMS value characterizes the mean fit of amplitudes in the moment tensor inversion for the analyzed dataset of synthetic AEs. The RMS values are color coded. The optimum solution is marked by the white circle. The optimum RMS is 0.069 with the horizontal attenuation of 0.0058 and the vertical attenuation of 0.0032.

5.5 APPLICATION TO LABORATORY DATA

5.5.2 SENSOR CALIBRATION

The analysis of AE recordings is difficult because of inaccurate sensors calibration and unknown coupling effects. Since measuring correct amplitudes is a key factor in determining accurate moment tensors, this problem has to be solved in all studies of AEs. Here, we apply two methods for calibrating the sensors: first, the method of Kwiatek et al. (2014a), which uses ultrasonic transmission data for evaluating sensor amplifications and coupling effects, and second, the network sensor calibration proposed by Davi and Vavryčuk (Davi & Vavryčuk, 2012; Davi et al., 2013) based on a joint inversion of many AE events for moment tensors. Both methods yielded similar amplification factors and detected no problems with coupling effects. The only exception was sensor 12. The calibration revealed that this sensor has a flipped polarity and anomalously low amplitudes of waveforms. Therefore, we decided to exclude sensor 12 from the analysis.

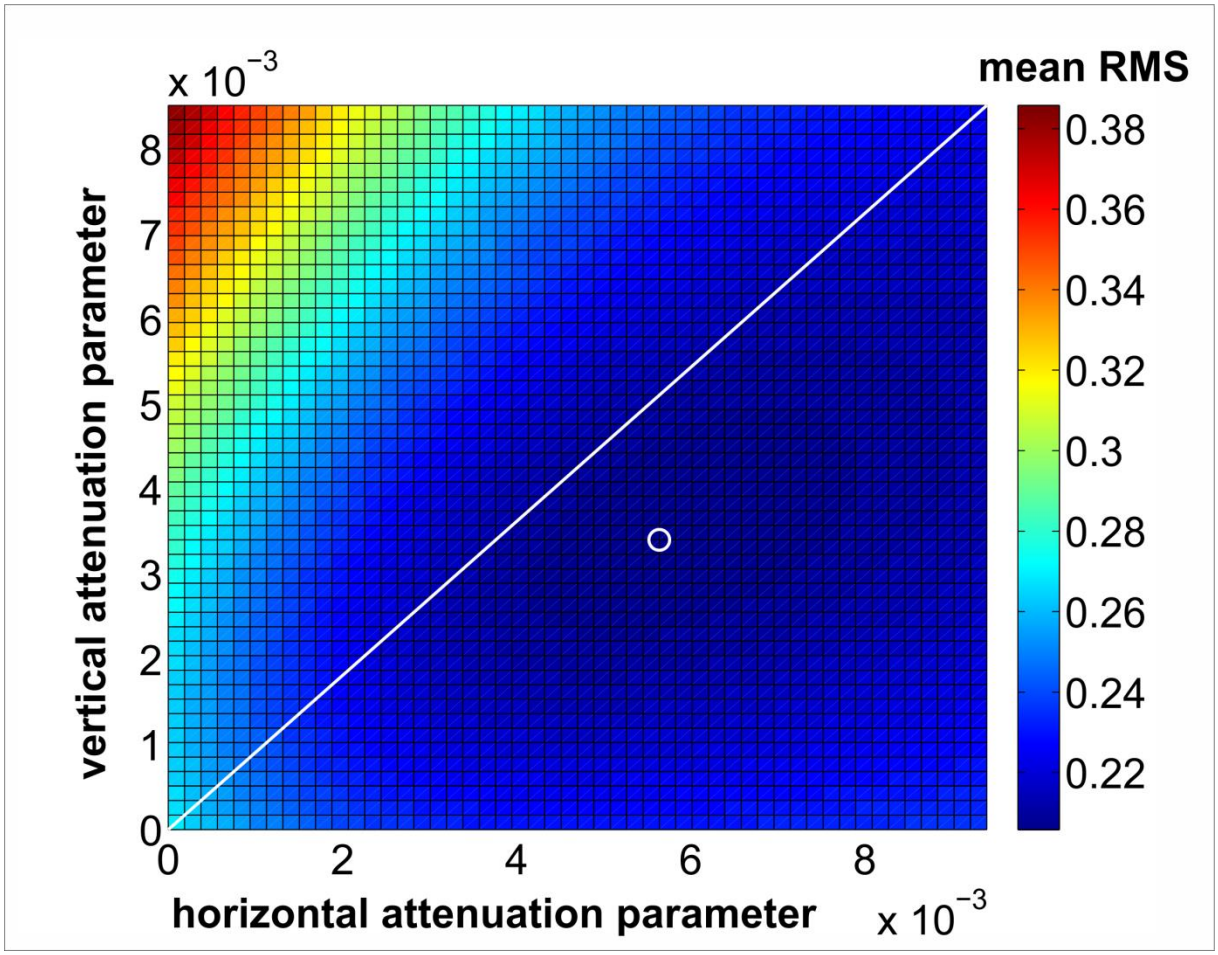

Figure 5.8: Inversion for anisotropic attenuation. The mean RMS value characterizes the mean fit of amplitudes in the moment tensor inversion for the analyzed dataset of observed AEs. The RMS values are color coded. The optimum solution is marked by the white circle. It corresponds to the RMS of 0.21 with the horizontal attenuation of 0.0056 and the vertical attenuation of 0.0034.

5.5.3 Inversion for Anisotropic Attenuation

We started with the inversion for the attenuation parameters of the rock sample. We selected a subset of 429 events out of 1277 events, which occurred in the centre of the sample, to ensure good coverage of sensors on the focal sphere. Amplitudes were picked using an automatic picking algorithm based on the Akaike information criterion (Leonard & Kennett, 1999). The amplitudes were repeatedly inverted for the moment tensors in a grid search scheme assuming horizontal and vertical attenuation parameters ranging from 0 to 0.0094 in steps of 0.0002. For each combination of attenuation parameters, we calculated the average RMS for the analysed dataset of AEs. We obtained a smooth 2-D RMS function with its minimum of 0.21 for the horizontal attenuation of 0.0056 and for the vertical attenuation of 0.0034 (Figure 5.8).

Since the attenuation is also changing with time (increasing load) we only obtain rough estimates of attenuation parameters averaged over time. But nevertheless, we clearly observe a higher value of the attenuation in the horizontal direction compared to the vertical direction. This is in good correspondence to the retrieved attenuation from ultrasonic transmission data. During the differential compression of the rock specimen, the horizontal cracks are closing and the pore space is compacted in the vertical direction. Consequently, elastic waves travelling in the vertical direction are less attenuated and the P-wave velocities increase. The granite sample had an initial pore density of 1.3% demonstrating a small pore space (Stanchits et al., 2006). Thus, the increase in the P-wave velocity as well as the decrease in attenuation is small in the vertical direction (Figure 5.2). In contrary, vertical cracks are opening causing a significant reduction of the P-wave velocity in the horizontal direction together with an increase in attenuation in the direction parallel to the crack normal (Hudson, 1981). Also strain measurements show that dilatant cracking becomes increasingly important in the horizontal direction (Stanchits et al., 2006). In summary, we successfully derived the attenuation parameters of the specimen in the horizontal and vertical directions using moment tensor inversion techniques.

5.5.4 Sensitivity of Moment and Source Tensors to Anisotropy and Attenuation

Similarly as in the synthetic tests of the sensitivity of the moment and source tensors to anisotropy and attenuation, we run the inversion using three medium models: the viscoelastic anisotropic medium, the viscoelastic isotropic medium and the elastic anisotropic medium. The parameters of anisotropy of the sample are determined from ultrasonic measurements (see Section 5.3). For attenuation, we adopted values obtained from the attenuation inversion described in Section 5.5.3.

The results of the inversion can be summarized as follows (see Figure 5.9 and Figure 5.10). First, all three inversions yield the RMS that increased with time up to 0.5. This probably reflects the fact that continuously increasing axial load introduced fracturing of the sample, which is not fully adequately described by the adopted homogeneous medium models. Second, neglecting the velocity anisotropy has a significant impact on focal mechanisms. A high scatter of the P and T axes of the source tensors indicates significant errors in focal mechanisms and a low resolution of geometry of faulting. In contrary, if anisotropy is considered and its effect is correctly removed by calculating the source tensors, the P axes are close to the vertical direction and the T axes are nearly horizontal. This behaviour is physically reasonable and in good correspondence to the applied stress regime.

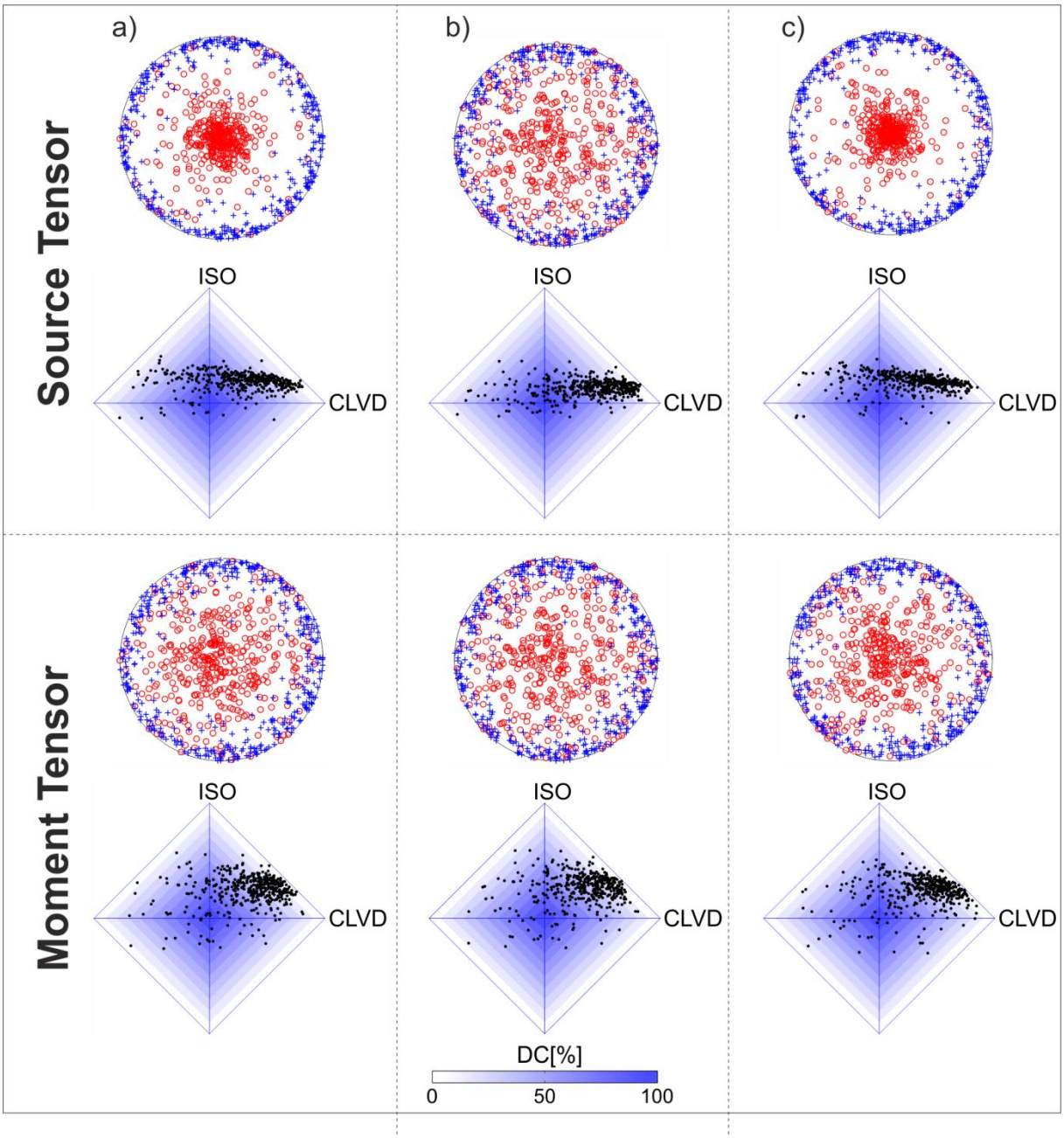

Figure 5.9: The P axes (red circles) and T axes (blue plus signs) and the non-DC components of AE events determined from the source and moment tensors in the viscoelastic anisotropic medium (a), the viscoelastic isotropic medium (b), and the elastic anisotropic medium (c).

Here, analysing only the moment tensors is not representative for the geometry of faulting since the influence of anisotropy on the moment tensors is high yielding high scatters of P and T axes. Third, the non-DC components are rather stable in all three inversions (Figure 5.9). The ISO and CLVD components are predominantly positive for the moment as well as source tensors. This indicates that mainly tensile cracks were activated. The scatter of the CLVD component is higher than that for the ISO component, which is also a general observation from the synthetic tests presented in this article. This implies that errors in the modelling procedure mainly affect the CLVD component by producing a high scatter of their values. Furthermore, the non-DC components of the source tensors are better clustered than the non-DC components of the moment tensors. Especially, the scatter in the ISO component is reduced.

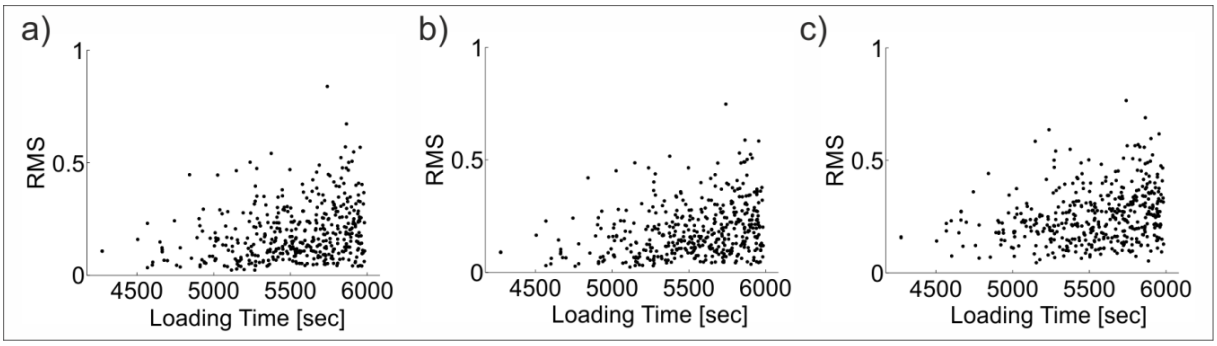

Figure 5.10: Root-mean-square (RMS) values of the moment tensor inversion of AE data assuming the viscoelastic anisotropic medium (a), the viscoelastic isotropic medium (b) and the elastic anisotropic medium (c).

5.6 DISCUSSION AND CONCLUSIONS

The seismic moment and source tensors are important tools for characterizing the source processes generating AEs prior the macroscopic failure. Differential loading in rock samples usually generates stress induced anisotropy and attenuation in the rock sample, which also affects the moment and source tensors. Therefore, it is important to study the sensitivity of these tensors to anisotropy and attenuation of rocks.

The laboratory experiments are advantageous for the analysis of sensitivity of source and moment tensors to anisotropy and attenuation since they are carried out under controlled conditions and the physical parameters of the rock sample can be accurately monitored. In addition, the sensors can be more optimally distributed over the focal sphere than in field experiments. The rock samples can be selected to display various levels of anisotropy and attenuation depending on the load applied to the specimen. Finally, the loading of the rocks samples usually produces thousands of AEs needed for a robust analysis with a statistical relevance. The determination of the moment and source tensors of AEs, however, is also challenging in several aspects. The sensors should be carefully calibrated and the AE sensor coupling problems should be eliminated. The number of sensors should be high and the recordings should have a sufficient dynamic range.

Based on the synthetic tests and on the laboratory tests (real measurements) we proved that the moment and source tensors of AEs are quite sensitive to anisotropy and attenuation of the rock sample. Interestingly, the sensitivity depends on the fracturing mode of AEs. We found that tensile events are more sensitive to anisotropy and attenuation of the sample than shear events. Neglecting anisotropy or attenuation of the sample, while performing the moment tensor inversion, results in significant errors in the retrieved moment and source tensors. These errors appear in the DC components, which describe the focal mechanisms, but also in the non-DC components. We showed that geometry of faulting in anisotropic rock samples should be studied using the source tensors, since the P and T axes of the moment tensors are affected by anisotropy and deviate from the true orientation of faulting. The stronger the anisotropy is, the higher the deviations are. The source tensors are free of this undesirable effect. Furthermore, we found that errors in the velocity model due to neglecting anisotropy are mainly projected into the CLVD component resulting in high scatter of the retrieved values. In comparison, the influence on the ISO component is low.

Finally, we proved that the moment tensor inversion applied to a large dataset of AEs could be utilized to provide information on parameters of the rock sample. Here, we applied this method to determining P-wave attenuation of the sample. The resolution of the

method was high enough for distinguishing between values of attenuation in the horizontal and vertical directions. We further retrieved anisotropy in attenuation by analysing ultrasonic measurements. The results support our finding that the horizontal attenuation is higher than the vertical attenuation. The anisotropic attenuation was produced by presence of tensile cracks in the sample aligned along the axial load applied to the specimen.

6 Conclusions and Perspectives

Reliable determination and interpretation of non-double-couple (non-DC) components of seismic moment tensors is a challenging task that has triggered many discussions among seismologists. This thesis presents a comprehensive study addressing the resolvability and interpretation of the non-DC components on laboratory and field scales. Several aspects of the non-DC component analysis are particularly highlighted and new methods for an accurate determination of the non-DC components are introduced.

On the field scale, the aftershock sequence of the M_w=7.4 1999 Izmit earthquake in northwestern Turkey was analysed. Prior to the analysis of the waveform recordings, an extensive synthetic case study was performed in order to assess the network's capability for detecting source-related non-DC components. The tests revealed that the error bounds for both, the ISO and the CLVD component, remain considerably high at ±15%. The orientation of the faulting mechanisms, however, remains stable even when the errors in the modelling procedure are significant. Here, the deviation of the P- and T-axes due to the errors in the modelling procedure was observed not to exceed 15°. The study further revealed that constraining the moment tensor to the shear-tensile source model during the inversion yields significantly smaller errors in the non-DC components than inverting for the full moment tensor, provided that the data reflect shear-tensile source mechanisms. Constraining the parameter space by allowing only physically reasonable source mechanisms, such as the shear-tensile source model, stabilizes the inversion and reduces the uncertainties of the non-DC components, particularly for the CLVD component. Despite an excellent dataset and good coverage of the rupture zone, the focal sphere coverage of the aftershock recordings has been found to lack observations at near-vertical incidence, which causes irregularities and gaps in the focal sphere coverage. This led to insufficient stability in the inversion of the moment tensor. Here, including even a few S-wave amplitudes into the moment tensor inversion significantly helped to find stable moment tensor solutions.

The application of the moment tensor inversion to aftershock recordings of the 1999 Izmit earthquake revealed only 33 stable high-quality moment tensor solutions although the analysed event catalogue contained more than 4,000 relocated events. This drastic reduction is justified by the strict selection criteria, which were applied to the catalogue to ensure high-quality data with sufficient focal sphere coverage. In particular, the lack of observations with near-vertical incidence angles leads to unstable moment tensor solutions. Among the set of the 33 selected moment tensors, nine are located in the Izmit-Sapanca segment and seven in the Karadere-Düzce segment, reflecting shear strike-slip events with no or negligible non-DC components in the seismic moment tensor. Since the non-DC components are smaller than the defined error bounds achieved from the synthetic case study, it is not possible to discriminate between source-related and artificial non-DC components generated by errors in the modelling procedure. Therefore, these events might even be pure shear, which correlates well with the outcome of other studies reporting a predominantly shear strike-slip stress regime along these segments (Bohnhoff et al., 2006; Bulut et al., 2007). In contrary, the 17 events located below the Akyazi plain show normal faulting mechanisms with significant positive non-DC components of up to 48%. Here, a slip

deficit of approximately 3.5 m was accumulated during the main shock and the release of the main shock was distributed over several small-scale NS-trending faults. However, the observed non-DC components clearly exceed the defined error bounds of the synthetic case study and thereby suggest a tensional component in source mechanisms, which might indicate large-scale fluid flow in the study area's crust. It is known that large earthquakes, such as the Izmit earthquake, can facilitate pressure-driven fluid flow within the crust, by creating hydraulic pathways, which connect segments of the upper and lower crust with their different pore pressure levels. Increased fluid pressure reduces the effective normal stress on pre-existing faults and can trigger a subsequent high aftershock activity promoting tensile source mechanisms. Therefore, the observation of the positive non-DC components in the Akyazi segment can explain the accelerated compensation of the slip deficit through the upward migration of fluids, which reduce the effective normal traction (or friction) on coseismically stressed normal faults in the pull-apart structure.

On the laboratory scale, acoustic emissions (AEs) recorded during a triaxial loading experiment of a granite sample in the laboratory were analysed. Direct measurements of P-wave velocities and amplitudes during the experiments show that the P-wave velocities become highly anisotropic with increasing load and the attenuation of waves propagating in the horizontal direction increases. Therefore, a new moment tensor inversion algorithm in viscoelastic anisotropic media was implemented and validated. Using synthetic tests it was found that moment tensors are less suitable for interpreting source parameters in strongly anisotropic media, since they are significantly influenced by the elastic parameters of the medium surrounding the fault. In this case, the source tensor proved to accurately determine the faulting parameters. The source tensor is independent of the elastic parameters of the medium and therefore directly related to the faulting parameters even in anisotropic media. It was further shown that the moment and source tensors of tensile events are more sensitive to attenuation and anisotropy than those of shear events. This can be explained by differences in the radiation pattern. While the radiation pattern of a shear event is formed by four lobes, the radiation pattern of a tensile event is axially symmetric with two lobes only and therefore providing less directional variation. The synthetic tests further showed that the CLVD component is more sensitive to anisotropy and attenuation than the ISO component. As a consequence, the CLVD values displayed a high scatter, if anisotropy or attenuation was neglected. The application of the developed inversion algorithm to a large dataset of AE waveform recordings supported the findings drawn from the synthetic tests. The faulting parameters derived from the source tensors cluster in accordance to the applied stress regime, while the source parameters derived from the moment tensors are diverse and scattered. Finally, the algorithm was applied to a large dataset of AEs to determine the attenuation parameter of the medium in a grid search scheme. The resolution of the method was sufficiently good to discriminate attenuation values for the horizontal and vertical directions.

Studying the datasets on these two distinct scales provided the opportunity to analyse various aspects of the non-DC components. On the regional scale, the focus was rather on the uncertainty assessment and tectonic interpretation of the non-DC components. On the laboratory scale, the study focused on the improvement and validation of the moment tensor inversion algorithm and on effects of anisotropy and attenuation on the interpretation of the non-DC components. Based on the results of both types of studies, the following general conclusions can be drawn.

Firstly, it was shown on both scales that a profound analysis of uncertainties by performing extensive synthetic tests is inevitable for any estimation of reliable non-DC

components. The tests made it possible to study the resolution capability of the given network in order to detect the source-related non-DC components under certain boundary conditions. This provides a confidence level for the analysis of real data, which forms a reliable basis for the interpretation of the non-DC components, while avoiding misinterpretations. Moreover, the synthetic tests are useful for designing future networks aimed at detecting reliable potential non-DC components. The determination and interpretation of the non-DC components in aftershock recordings demonstrated serious difficulties in obtaining credible non-DC components using network geometry, which was considered to be very good by today's standards. A drastic reduction of events was necessary to meet the quality criteria to ensure high-quality moment tensors when analysing the Izmit aftershocks. A similar reduction was also reported in the study of the non-DC components for induced seismic events at the Geysers geothermal field in California (Ross et al., 1996). Thus, regional networks with similar geometry as for the Geysers or Izmit are not optimum, and better strategy for designing regional networks should be developed. Nevertheless, this exemplary study showed that despite all difficulties in obtaining the non-DC components, their analysis substantially contributes particularly to the understanding of the source mechanism and, in particular, to the knowledge of the seismotectonic settings of the study area in a postseismic scenario in a broader context.

Since Brace and Byerlee (1966) suggested that laboratory stick-slip friction experiments may be useful analogues for understanding tectonic earthquakes, considerable research has been undertaken to understand whether observations obtained from laboratory experiments can be extrapolated to larger scales (Aki & Richards, 2002; Abercrombie & Rice, 2005; Ben-Zion, 2008; McGarr et al., 2010). Since most studies support the idea of self-similarity of earthquakes (Lockner et al., 1991; Yoshimitsu et al., 2014), laboratory experiments are deemed to be a highly effective tool for simulating faulting processes under controlled boundary conditions. The physical parameters of the rock sample can be accurately monitored and the sensors can be optimally distributed over the focal sphere, which is rather difficult in field experiments. The boundary conditions such as the confining pressure, the axial load and the fluid content can be controlled to simulate observations at the field scale. Finally, especially relevant for the moment tensor analysis, rock deformation experiments in the laboratory usually produce thousands of AEs needed for a robust analysis with a statistical relevance. The determination of the moment and source tensors of AEs recorded in the laboratory, however, is also challenging in several aspects. The sensors must be carefully calibrated in order to eliminate coupling problems. Furthermore, the number of sensors should be large and the recordings should have a sufficient dynamic range.

Although seismic observations confirm that rocks are anisotropic and attenuating (Barton, 2007; Carcione, 2007) in most tectonic environments, so far these effects have largely been neglected in the moment tensor inversion and in the determination of the non-DC components. However, the study of the source and moment tensors of AEs revealed that seismic anisotropy and attenuation cannot be ignored as commonly assumed at present. Direct ultrasonic measurements of physical properties of a rock sample during a loading experiment provided a unique opportunity to assess how attenuation and anisotropy affects the retrieved moment and source tensors. Interestingly, the effects are quite strong, particularly, in the shear-tensile faulting regime. This finding has serious consequences for studying moment and source tensors on the field scale and underlines the fundamental importance of AE studies for developing accurate moment tensor inversions.

In conclusion, both the performed laboratory and field-scale investigations demonstrate the practical challenges associated with the moment tensor analysis and in determining the non-DC components. Both further contribute to a better understanding of the driving mechanisms and the influence of the medium parameters on the non-DC components, which allows more detailed information on the geometry of fractures, the fracture processes and on the properties of the fractured rock to be obtained.

6.1 PERSPECTIVES

The investigations performed within this thesis constitute the following perspectives, which may be addressed in forthcoming research projects. The examination of these questions is expected to have significant potential to improve the understanding of the driving mechanisms that produce the non-DC components. The most relevant topics for future research are:

- The extension of the moment tensor inversion for viscoelastic anisotropic media in order to invert for the P- and S-wave amplitudes simultaneously and/or constraining the moment tensor to the shear-tensile source model. This is especially relevant when this inversion scheme is applied to field data, because clear S-waves are prevalent and their consideration is likely to enhance the stability of the moment tensor inversion.
- The application of the moment tensor inversion in viscoelastic anisotropic media to aftershock recordings of the 1999 Izmit earthquake. In the presented study, S-wave amplitudes are included in the inversion only if they do not show polarization related splitting. Thus, many events were excluded from the analysis. If the inversion algorithm considers anisotropy, more data can be included in the inversion and the number of possible stable moment tensor solutions can be increased, thereby providing more information for statistical relevance.
- The application of the moment tensor inversion in viscoelastic and anisotropic media to induced seismicity in hydrocarbon or geothermal reservoirs to study the velocity anisotropy and attenuation in the focal zone and related physical processes. Martínez-Garzón et al. (2013) reported on stress changes due to fluid injection in a geothermal reservoir, which might be an indicator for changes in the velocity field supporting the occurrence of stress-induced anisotropy.
- The stress-induced anisotropy generated and measured in the laboratory provides optimum conditions for testing the simultaneous inversion of moment tensors and anisotropy parameters, similar to the inversion scheme presented in the thesis for a simultaneous inversion of moment tensors and attenuation parameters.

A. Appendix

Supplementary results for synthetic hypocentres 1 and 3 as described in Chapter 3.

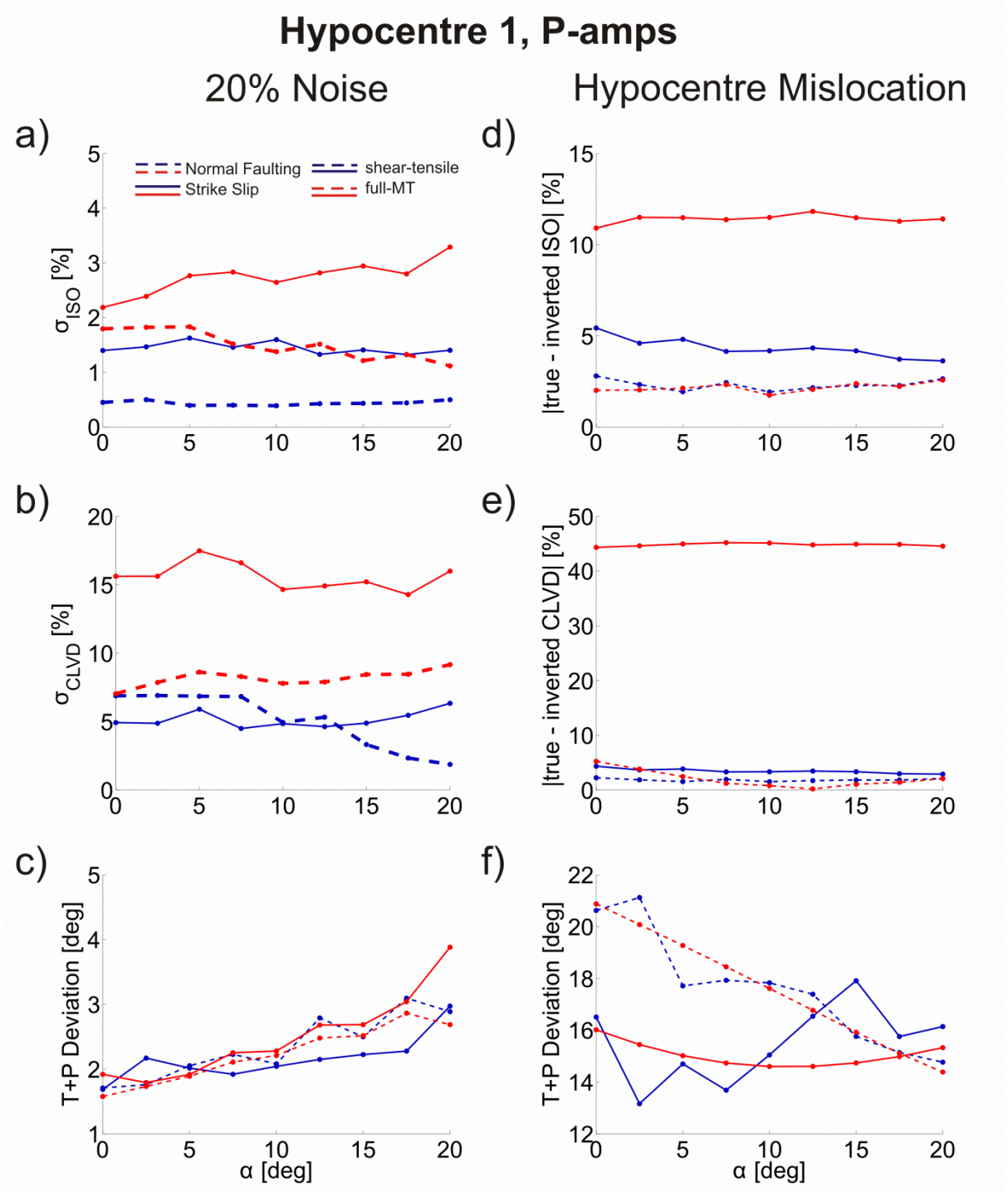

Figure A.1: Moment tensor inversion for noisy amplitudes (left) and hypocentre mislocation (right) for the inversion of P-wave amplitudes only at Hypocentre 1. Errors are shown as a function of slope α. Red lines - the linear full moment tensor inversion, blue lines - the non-linear inversion constrained to a shear-tensile source model. We further distinguish between strike-slip mechanism (solid lines) and normal faulting mechanisms (dashed lines). Plots a) and b) show standard deviations of the ISO and CLVD component, respectively, determined from 100 inversions of noise contaminated amplitudes (noise level is 20% of the amplitude of each station). Plots d) and e) present the difference between the retrieved and true percentages of ISO and CLVD component, respectively. The deviation between the retrieved and true P- and T-axes are displayed in plots c) and f).

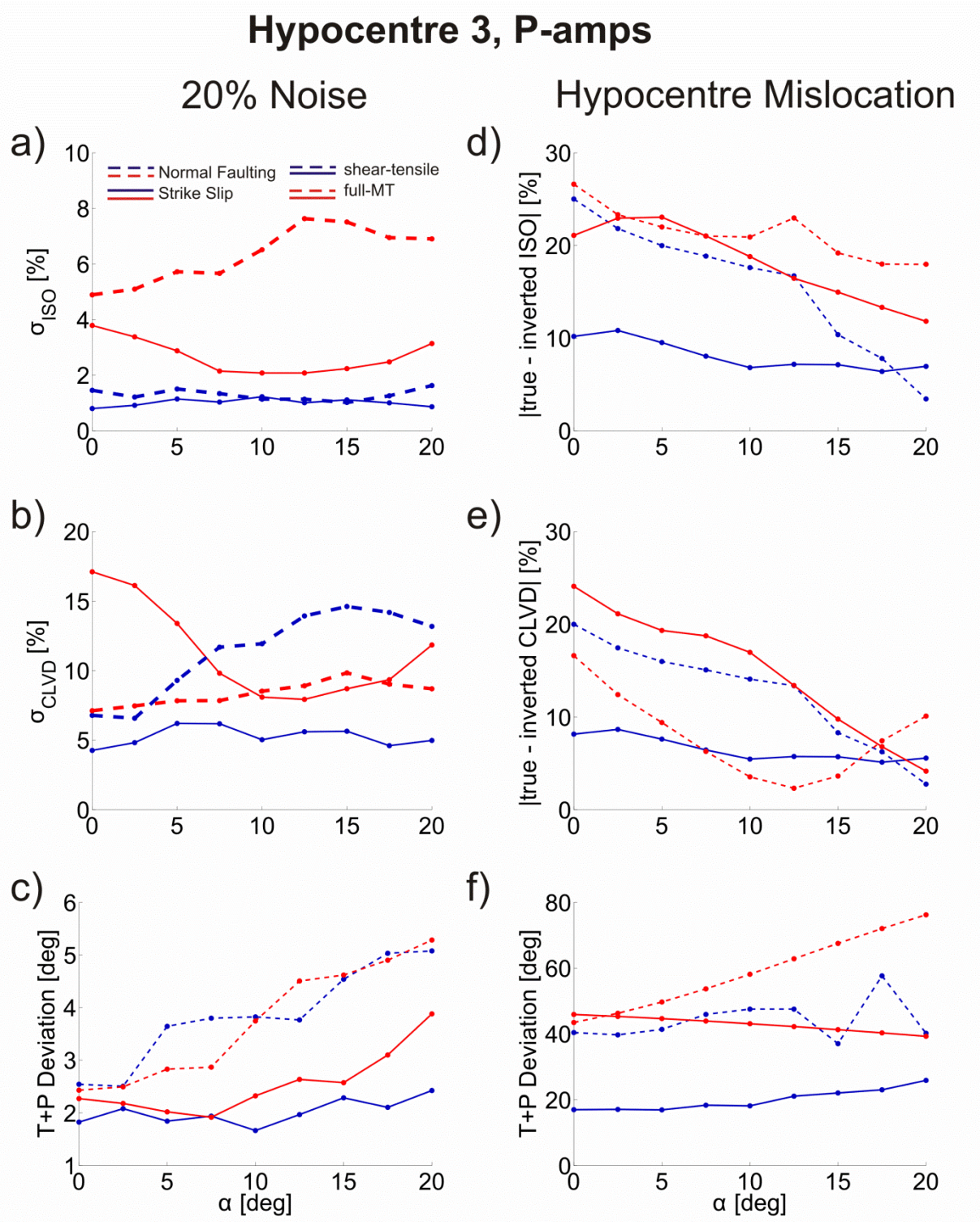

Figure A.2: Moment tensor inversion for noisy amplitudes (left) and hypocentre mislocation (right) for the inversion of P-wave amplitudes only at Hypocentre 3. For details, see the caption of Figure A.1**.**

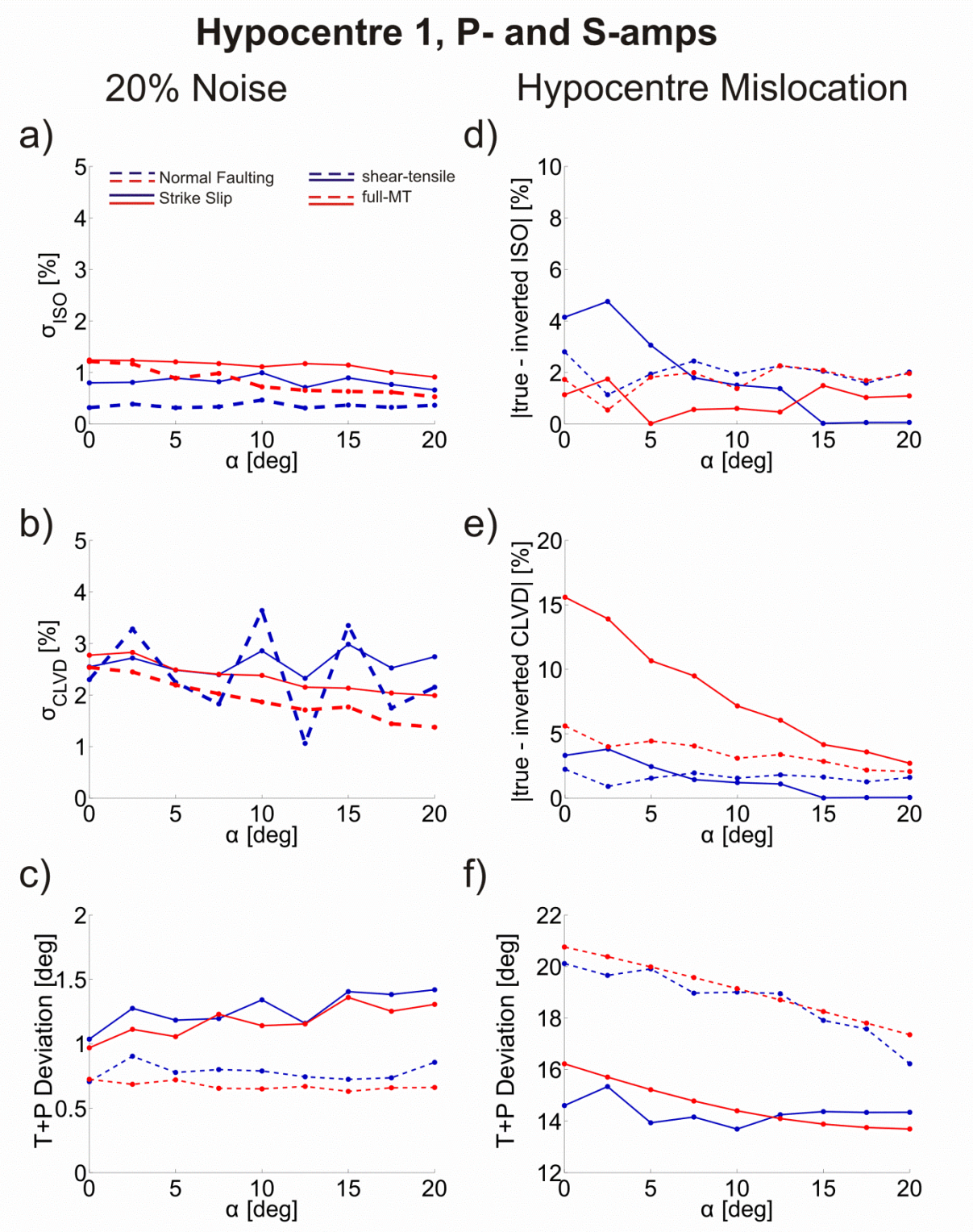

Figure A.3: Moment tensor inversion for noisy amplitudes (left) and hypocentre mislocation (right) for the inversion of P- and S-wave amplitudes at Hypocentre 1. For details, see the caption of Figure A.1**.**

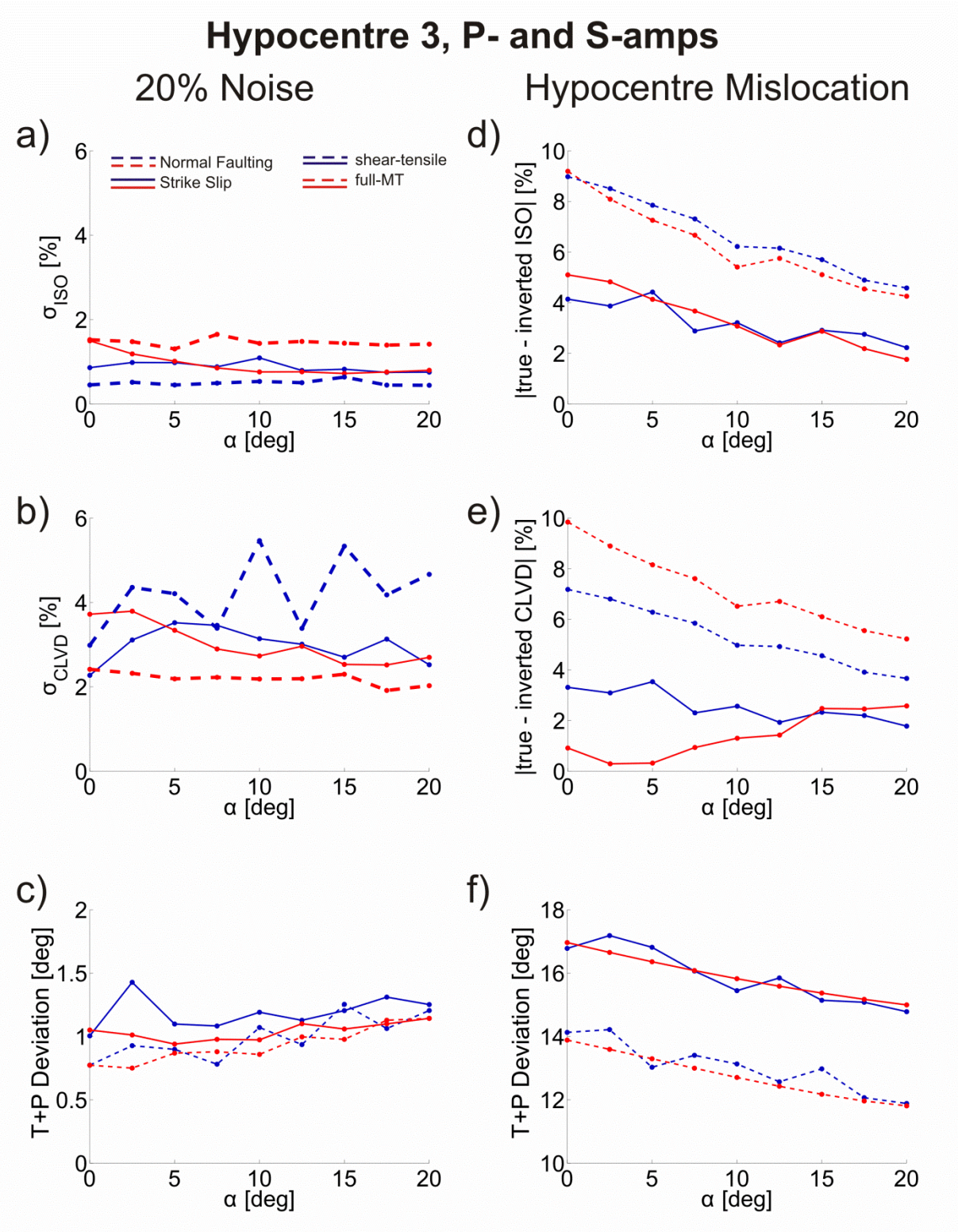

Figure A.4: Moment tensor inversion for noisy amplitudes (left) and hypocentre mislocation (right) for the inversion of P- and S-wave amplitudes at Hypocentre 3. For details, see the caption of Figure A.1**.**

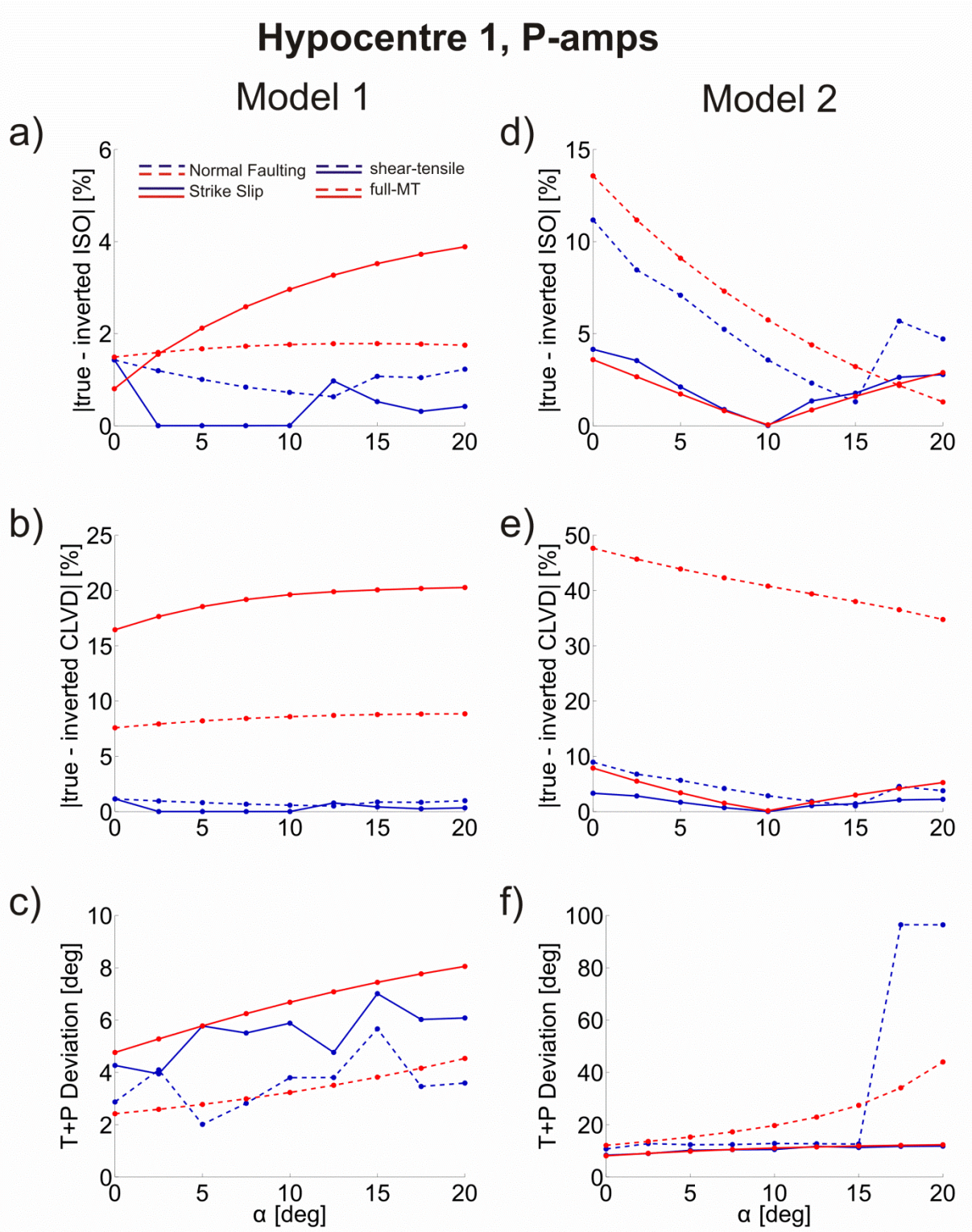

Figure A.5: Moment tensor inversion for weak (left) and strong (right) velocity mismodelling using P-wave amplitudes only at Hypocentre 1. Plots a) and b) show the difference between the retrieved and true percentages of ISO and CLVD components, respectively, using model 1. Plots d) and e) show the same for model 2. The deviations between P- and T-axes of retrieved and true fault planes are displayed in plots a) and f) for model 1 and model 2, respectively.

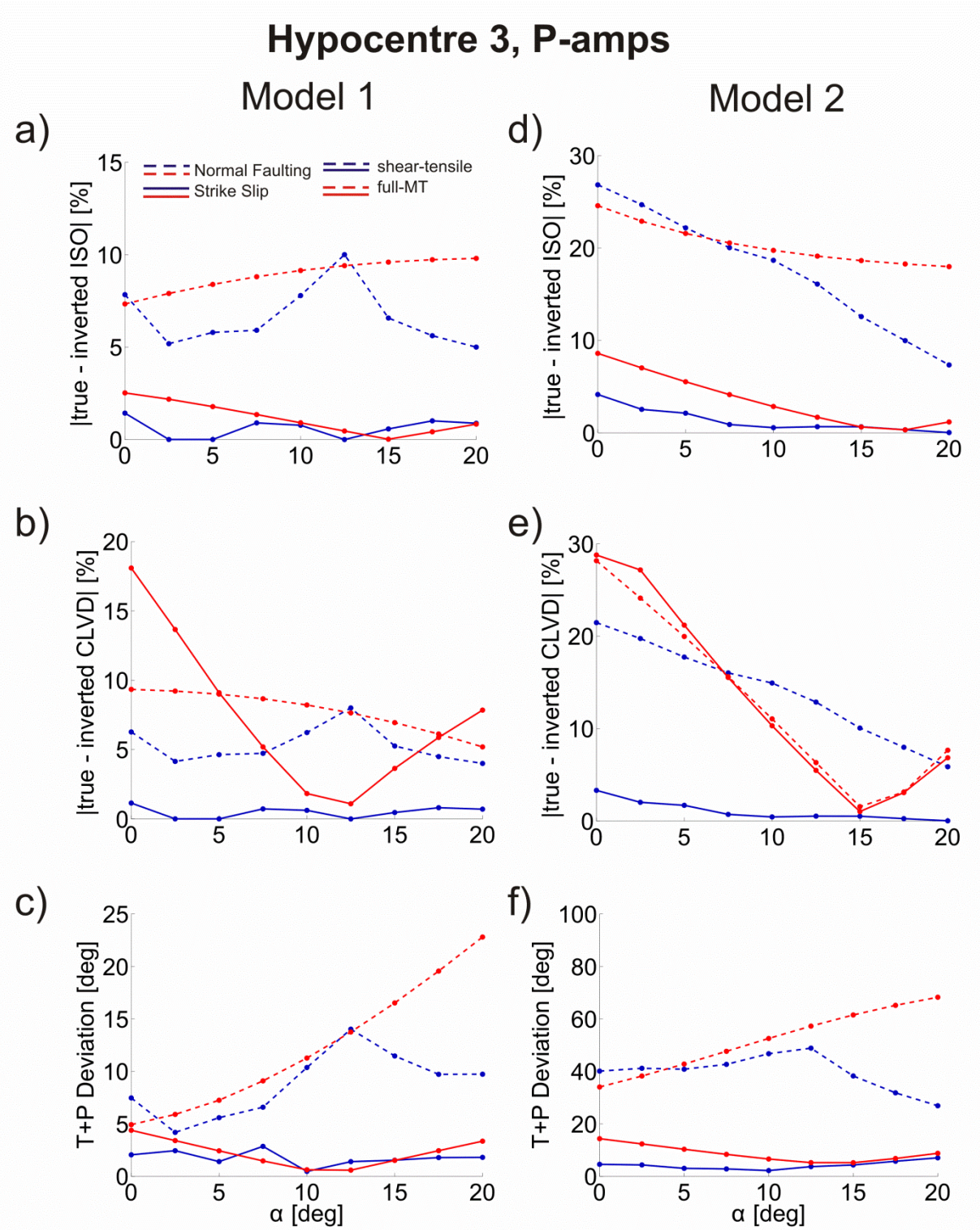

Figure A.6: Moment tensor inversion for weak (left) and strong (right) velocity mismodelling using P-wave amplitudes only at Hypocentre 3. For details, see the caption of Figure A.5.

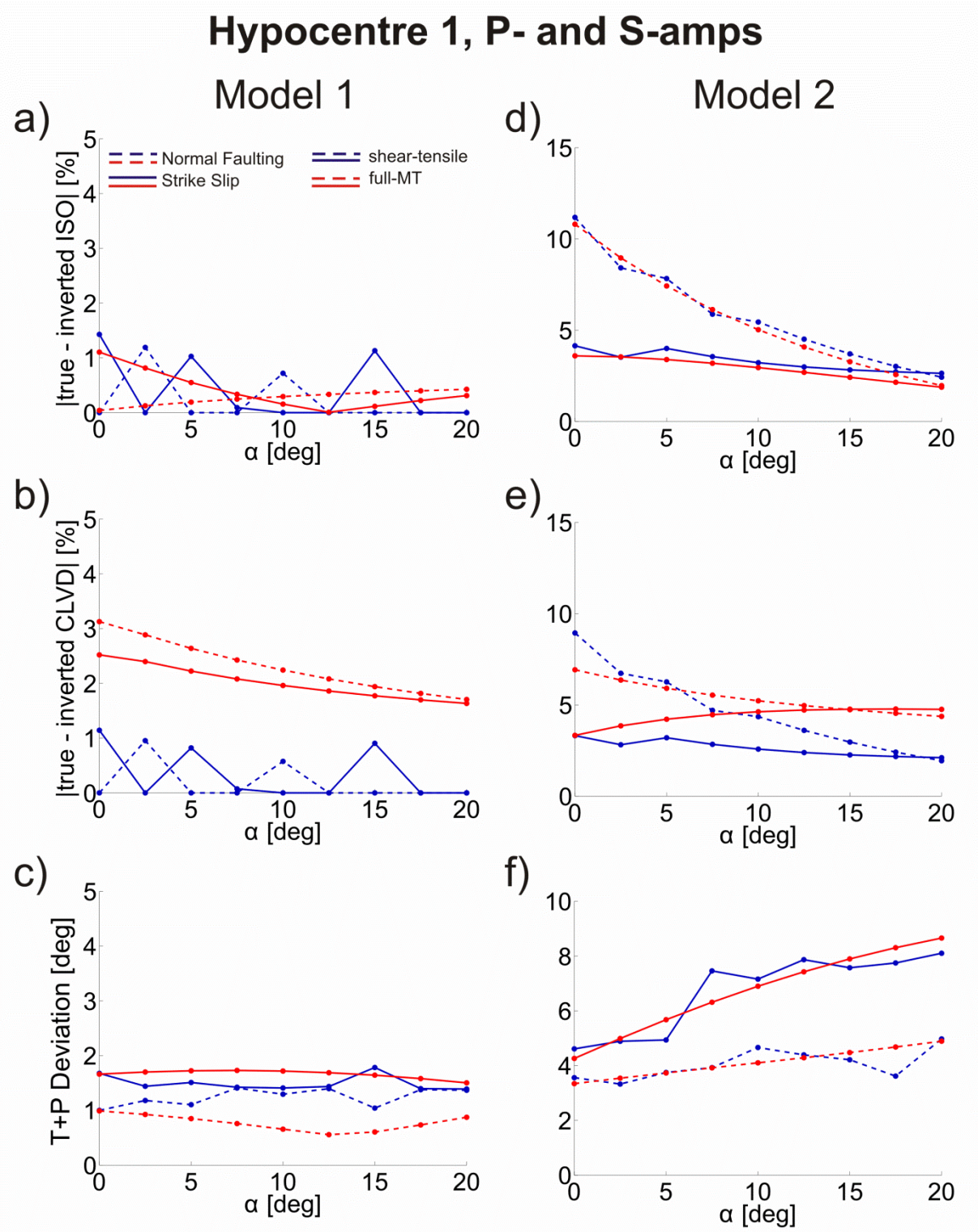

Figure A.7: Moment tensor inversion for weak (left) and strong (right) velocity mismodelling using P- and S-wave amplitudes at Hypocentre 1. For details, see the caption of Figure A.5.

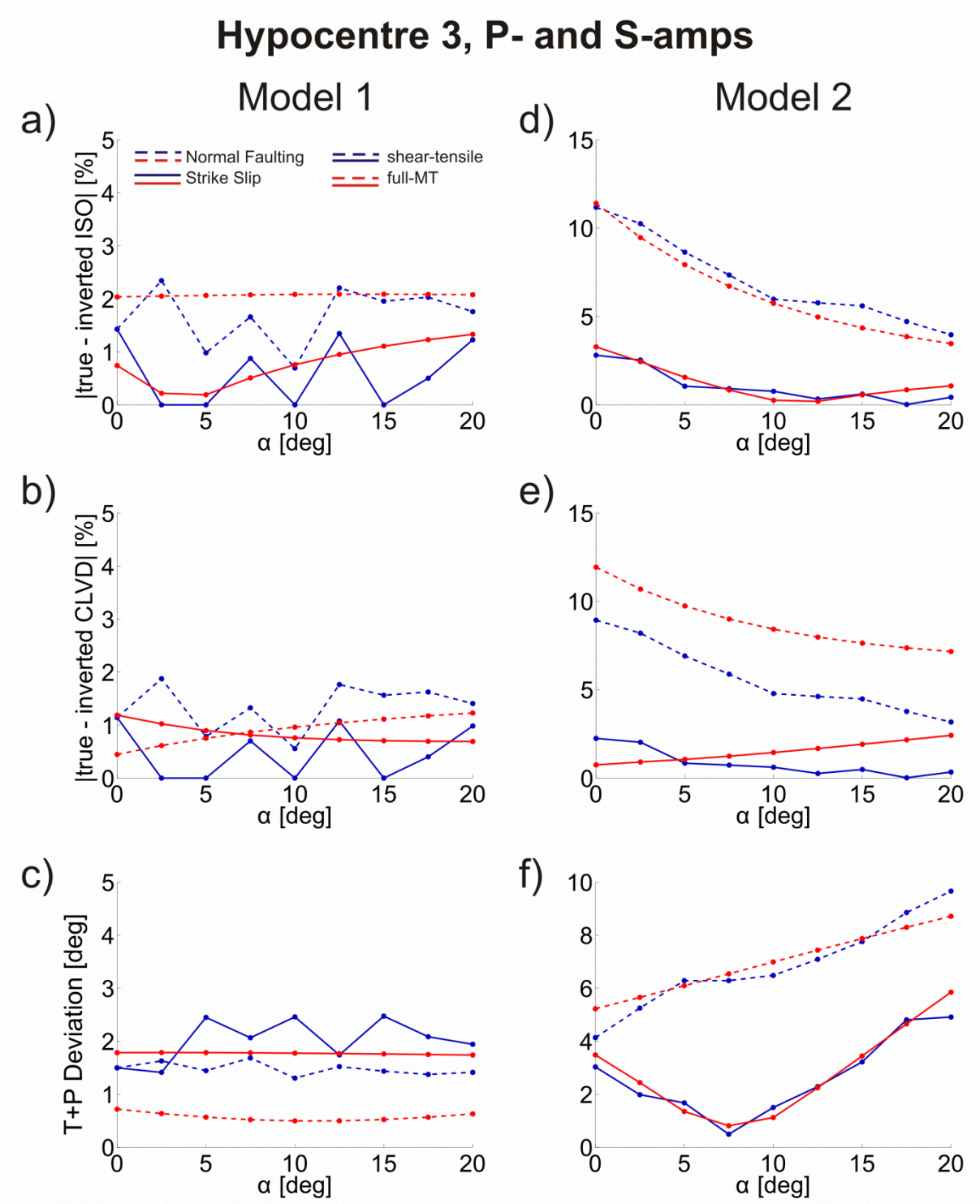

Figure A.8: Moment tensor inversion for weak (left) and strong (right) velocity mismodelling using P- and S-wave amplitudes at Hypocentre 3. For details, see the caption of Figure A.5.

References

Abercrombie, R. E., & Rice, J. R. (2005). Can observations of earthquake scaling constrain slip weakening? *Geophysical Journal International*, **162**(2), 406–424.

Aker, E., Kühn, D., Vavryčuk, V., Soldal, M., & Oye, V. (2014). Experimental investigation of acoustic emissions and their moment tensors in rock during failure. *International Journal of Rock Mechanics and Mining Sciences*, **70**, 286–295.

Aki, K., & Richards, P. G. (2002). *Quantitative seismology* (2nd ed., Vol. 1). University Science Books.

Ambraseys, N. N., & Zatopek, A. (1969). The Mudurnu Valley, West Anatolia, Turkey, earthquake of 22 July 1967. *Bulletin of the Seismological Society of America*, **59**(2), 521–589.

Andersen, L. M. (2001). *A relative moment tensor inversion technique applied to seismicity induced by mining* (PhD thesis). University of the Witwatersrand Johannesburg, South Africa.

Armijo, R., Meyer, B., Navarro, S., King, G., & Barka, A. (2002). Asymmetric slip partitioning in the Sea of Marmara pull-apart: a clue to propagation processes of the North Anatolian Fault? *Terra Nova*, **14**(2), 80–86.

Auld, B. A. (1973). Acoustic fields and waves in solids. *John Wiley & Sons Inc.*, **1**.

Backus, G., & Mulcahy, M. (1976). Moment tensors and other phenomenological descriptions of seismic sources—I. Continuous displacements. *Geophysical Journal International*, **46**(2), 341–361.

Barka, A., Akyüz, H. S., Altunel, E., Sunal, G., Çakir, Z., Dikbas, A., … De Chabalier, J. B. (2002). The surface rupture and slip distribution of the 17 August 1999 Izmit earthquake (M 7.4), North Anatolian fault. *Bulletin of the Seismological Society of America*, **92**(1), 43–60.

Barton, N. (2007). *Rock quality, seismic velocity, attenuation and anisotropy* (1st ed.). CRC Press.

Baumbach, M., Bindi, D., Grosser, H., Milkereit, C., Parolai, S., Wang, R., … Zschau, J. (2003). Calibration of an ML scale in northwestern Turkey from 1999 Izmit aftershocks. *Bulletin of the Seismological Society of America*, **93**(5), 2289–2295.

Ben-Zion, Y. (2003). Key formulas in earthquake seismology. *International Handbook of Earthquake and Engineering Seismology*, 1857–1875.

Ben-Zion, Y. (2008). Collective behavior of earthquakes and faults: Continuum-discrete transitions, progressive evolutionary changes, and different dynamic regimes. *Reviews of Geophysics*, **46**(4), RG4006.

Ben-Zion, Y., & Ampuero, J.-P. (2009). Seismic radiation from regions sustaining material damage. *Geophysical Journal International*, **178**(3), 1351–1356.

Bindi, D., Parolai, S., Grosser, H., Milkereit, C., & Karakisa, S. (2006). Crustal attenuation characteristics in northwestern Turkey in the range from 1 to 10 Hz. *Bulletin of the Seismological Society of America*, **96**(1), 200–214.

Bohnhoff, M., Grosser, H., & Dresen, G. (2006). Strain partitioning and stress rotation at the North Anatolian fault zone from aftershock focal mechanisms of the 1999 Izmit Mw= 7.4 earthquake. *Geophysical Journal International*, **166**(1), 373–385.

Bouchon, M., & Coutant, O. (1994). Calculation of synthetic seismograms in a laterally varying medium by the boundary element-discrete wavenumber method. *Bulletin of the Seismological Society of America*, **84**(6), 1869–1881.

Brace, W. F., & Byerlee, J. D. (1966). Stick-Slip as a Mechanism for Earthquakes. *Science*, **153**(3739), 990–992.

Bulut, F., Bohnhoff, M., Aktar, M., & Dresen, G. (2007). Characterization of aftershock-fault plane orientations of the 1999 Izmit (Turkey) earthquake using high-resolution aftershock locations. *Geophysical Research Letters*, **34**(20), L20306.

Burridge, R., & Knopoff, L. (1964). Body force equivalents for seismic dislocations. *Bulletin of the Seismological Society of America*, **54**(6A), 1875–1888.

Carcione, J. M. (2007). *Wave fields in real media: Wave propagation in anisotropic, anelastic, porous and electromagnetic media* (2nd ed., Vol. 38). Elsevier Science.

Červený, V. (2001). *Seismic ray theory*. Cambridge University Press.

Cesca, S., Rohr, A., & Dahm, T. (2013). Discrimination of induced seismicity by full moment tensor inversion and decomposition. *Journal of Seismology*, **17**(1), 147–163.

Charalampidou, E.-M., Stanchits, S., Kwiatek, G., & Dresen, G. (2015). Brittle failure and fracture reactivation in sandstone by fluid injection. *European Journal of Environmental and Civil Engineering*, **19**(5), 564–579.

Dahm, T. (1996). Relative moment tensor inversion based on ray theory: theory and synthetic tests. *Geophysical Journal International*, **124**(1), 245–257.

Davi, R., & Vavryčuk, V. (2012). Seismic network calibration for retrieving accurate moment tensors. *Bulletin of the Seismological Society of America*, **102**(6), 2491–2506.

Davi, R., Vavryčuk, V., Charalampidou, E.-M., & Kwiatek, G. (2013). Network sensor calibration for retrieving accurate moment tensors of acoustic emissions. *International Journal of Rock Mechanics and Mining Sciences*, **62**, 59–67.

Dziewonski, A. M., & Woodhouse, J. H. (1983). An experiment in systematic study of global seismicity: Centroid-moment tensor solutions for 201 moderate and large earthquakes of 1981. *Journal of Geophysical Research: Solid Earth*, **88**(B4), 3247–3271.

Dziewonski, A. M., Ekström, G., & Maternovskaya, N. N. (2001). Centroid—moment tensor solutions for July–September 2000. *Physics of the Earth and Planetary Interiors*, **124**(1), 9–23.

Eken, T., Bohnhoff, M., Bulut, F., Can, B., & Aktar, M. (2013). Crustal anisotropy in the Eastern Sea of Marmara region in northwestern Turkey. *Bulletin of the Seismological Society of America*, **103**(2A), 911–924.

Ellsworth, W. L. (2013). Injection-induced earthquakes. *Science*, **341**(6142), 1225942.

Finck, F., Kurz, J. H., Grosse, C. U., & Wolf-Reinhardt, H. (2003). Advances in moment tensor inversion for civil engineering. In *International Symposium on Non–Destructive Testing in Civil Engineering*. Berlin.

Foulger, G. R., Julian, B. R., Hill, D. P., Pitt, A. M., Malin, P. E., & Shalev, E. (2004). Non-double-couple microearthquakes at Long Valley caldera, California, provide evidence for hydraulic fracturing. *Journal of Volcanology and Geothermal Research*, **132**(1), 45–71.

Frohlich, C., Riedesel, M. A., & Apperson, K. D. (1989). Note concerning possible mechanisms for non double couple earthquake sources. *Geophysical Research Letters*, **16**(6), 523–526.

Frohlich, C. (1994). Earthquakes with Non—Double-Couple Mechanisms. *Science*, **264**(5160), 804–809.

Gilbert, F. (1971). Excitation of the normal modes of the Earth by earthquake sources. *Geophysical Journal International*, **22**(2), 223–226.

Goebel, T. H. W., Candela, T., Sammis, C. G., Becker, T. W., Dresen, G., & Schorlemmer, D. (2014). Seismic event distributions and off-fault damage during frictional sliding of saw-cut surfaces with pre-defined roughness. *Geophysical Journal International*, **196**(1), 612–625.

Görgün, E., Bohnhoff, M., Bulut, F., & Dresen, G. (2010). Seismotectonic setting of the Karadere–Düzce branch of the North Anatolian Fault Zone between the 1999 Izmit and Düzce ruptures from analysis of Izmit aftershock focal mechanisms. *Tectonophysics*, **482**(1), 170–181.

Graham, C. C., Stanchits, S., Main, I. G., & Dresen, G. (2010). Comparison of polarity and moment tensor inversion methods for source analysis of acoustic emission data. *International Journal of Rock Mechanics and Mining Sciences*, **47**(1), 161–169.

Gülen, L., Pinar, A., Kalafat, D., Özel, N., Horasan, G., Yilmazer, M., & Işikara, A. M. (2002). Surface fault breaks, aftershock distribution, and rupture process of the 17 August 1999 Izmit, Turkey, earthquake. *Bulletin of the Seismological Society of America*, **92**(1), 230–244.

Hamiel, Y., Lyakhovsky, V., Stanchits, S., Dresen, G., & Ben-Zion, Y. (2009). Brittle deformation and damage-induced seismic wave anisotropy in rocks. *Geophysical Journal International*, **178**(2), 901–909.

Hearn, E. H., McClusky, S., Ergintav, S., & Reilinger, R. E. (2009). Izmit earthquake postseismic deformation and dynamics of the North Anatolian Fault Zone. *Journal of Geophysical Research*, **114**, B08405.

Horálek, J., Šílený, J., & Fischer, T. (2002). Moment tensors of the January 1997 earthquake swarm in NW Bohemia (Czech Republic): double-couple vs. non-double-couple events. *Tectonophysics*, **356**(1), 65–85.

Hudson, J. A. (1981). Wave speeds and attenuation of elastic waves in material containing cracks. *Geophysical Journal International*, **64**(1), 133–150.

Hurd, O., & Bohnhoff, M. (2012). Stress-and Structure-Induced Shear-Wave Anisotropy along the 1999 Izmit Rupture, Northwest Turkey. *Bulletin of the Seismological Society of America*, **102**(5), 2177–2188.

Ickrath, M., Bohnhoff, M., Bulut, F., & Dresen, G. (2013). Stress rotation and recovery in conjunction with the 1999 Izmit Mw 7.4 earthquake. *Geophysical Journal International*, **196**(2), 951–956.

Jechumtálová, Z., & Šílený, J. (2005). Amplitude ratios for complete moment tensor retrieval. *Geophysical Research Letters*, **32**(22), L22303.

Jost, M. L., & Herrmann, R. B. (1989). A student's guide to and review of moment tensors. *Seismological Research Letters*, **60**(2), 37–57.

Julian, B. R., Miller, A. D., & Foulger, G. R. (1997). Non-double-couple earthquake mechanisms at the Hengill-Grensdalur volcanic complex, southwest Iceland. *Geophysical Research Letters*, **24**(7), 743–746.

Julian, B. R., Miller, A. D., & Foulger, G. R. (1998). Non-double-couple earthquakes 1. Theory. *Reviews of Geophysics*, **36**(4), 525–549.

Kagan, Y. Y. (1991). 3 D rotation of double couple earthquake sources. *Geophysical Journal International*, **106**(3), 709–716.

Kanamori, H., & Given, J. W. (1982). Use of long-period surface waves for rapid determination of earthquake source parameters 2. Preliminary determination of source mechanisms of large earthquakes (M S⩾ 6.5) in 1980. *Physics of the Earth and Planetary Interiors*, **30**(2), 260–268.

Kawakatsu, H. (1991). Enigma of earthquakes at ridge-transform-fault plate boundaries distribution of non-double couple parameter of Harvard CMT Solutions. *Geophysical Research Letters*, **18**(6), 1103–1106.

Kelly, K. R., Ward, R. W., Treitel, S., & Alford, R. M. (1976). Synthetic seismograms: a finite-difference approach. *Geophysics*, **41**(1), 2–27.

Kikuchi, M., & Kanamori, H. (1991). Inversion of complex body waves—III. *Bulletin of the Seismological Society of America*, **81**(6), 2335–2350.

Knopoff, L., & Randall, M. J. (1970). The compensated linear-vector dipole: a possible mechanism for deep earthquakes. *Journal of Geophysical Research*, **75**(26), 4957–4963.

Komatitsch, D., & Tromp, J. (1999). Introduction to the spectral element method for three-dimensional seismic wave propagation. *Geophysical Journal International*, **139**(3), 806–822.

Koulakov, I., Bindi, D., Parolai, S., Grosser, H., & Milkereit, C. (2010). Distribution of Seismic Velocities and Attenuation in the Crust beneath the North Anatolian Fault (Turkey) from Local Earthquake Tomography. *Bulletin of the Seismological Society of America*, **100**(1), 207–224.

Kravanja, S., Panza, G. F., & Šílený, J. (1999). Robust retrieval of a seismic point source time function. *Geophysical Journal International*, **136**(2), 385–394.

Kwiatek, G., Charalampidou, E.-M., Dresen, G., & Stanchits, S. (2014a). An improved method for seismic moment tensor inversion of acoustic emissions through assessment of sensor coupling and sensitivity to incidence angle. *International Journal of Rock Mechanics and Mining Sciences*, **65**, 153–161.

Kwiatek, G., Goebel, T. H. W., & Dresen, G. (2014b). Seismic moment tensor and b value variations over successive seismic cycles in laboratory stick-slip experiments. *Geopysical Research Letters*, **41**(16), 5838–5846.

Langridge, R. M., Stenner, H. D., Fumal, T. E., Christofferson, S. A., Rockwell, T. K., Hartleb, R. D., … Barka, A. A. (2002). Geometry, slip distribution, and kinematics of surface rupture on the Sakarya fault segment during the 17 August 1999 Izmit, Turkey, earthquake. *Bulletin of the Seismological Society of America*, **92**(1), 107–125.

Lay, T., & Wallace, T. C. (1995). *Modern global seismology*. San Diego, California: Academic Press.

Leonard, M., & Kennett, B. L. N. (1999). Multi-component autoregressive techniques for the analysis of seismograms. *Physics of the Earth and Planetary Interiors*, **113**(1), 247–263.

Lockner, D. A., Byerlee, J. D., Kuksenko, V., Ponomarev, A., & Sidorin, A. (1991). Quasi-static fault growth and shear fracture energy in granite. *Nature*, **350**(6313), 39–42.

Martínez-Garzón, P., Bohnhoff, M., Kwiatek, G., & Dresen, G. (2013). Stress tensor changes related to fluid injection at The Geysers geothermal field, California. *Geophysical Research Letters*, **40**(11), 2596–2601.

McGarr, A., Fletcher, J. B., Boettcher, M., Beeler, N., & Boatwright, J. (2010). Laboratory-based maximum slip rates in earthquake rupture zones and radiated energy. *Bulletin of the Seismological Society of America*, **100**(6), 3250–3260.

Miller, A. D., Foulger, G. R., & Julian, B. R. (1998). Non-double-couple earthquakes. 2. Observations. *Reviews of Geophysics*, **36**(4), 551–568.

Miller, S. A., Collettini, C., Chiaraluce, L., Cocco, M., Barchi, M., & Kaus, B. J. P. (2004). Aftershocks driven by a high-pressure CO2 source at depth. *Nature*, **427**(6976), 724–727.

Minson, S. E., Dreger, D. S., Bürgmann, R., Kanamori, H., & Larson, K. M. (2007). Seismically and geodetically determined non double-couple source mechanisms from the 2000 Miyakejima volcanic earthquake swarm. *Journal of Geophysical Research: Solid Earth (1978–2012)*, **112**, B10308.

Minson, S. E., & Dreger, D. S. (2008). Stable inversions for complete moment tensors. *Geophysical Journal International*, **174**(2), 585–592.

Nissen-Meyer, T., Fournier, A., & Dahlen, F. A. (2007). A two-dimensional spectral-element method for computing spherical-earth seismograms–I. Moment-tensor source. *Geophysical Journal International*, **168**(3), 1067–1092.

Ohtsu, M. (1991). Simplified moment tensor analysis and unified decomposition of acoustic emission source: application to in situ hydrofracturing test. *Journal of Geophysical Research: Solid Earth (1978–2012)*, **96**(B4), 6211–6221.

Oncescu, M. C. (1986). Relative seismic moment tensor determination for Vrancea intermediate depth earthquakes. *Pure and Applied Geophysics*, **124**(4-5), 931–940.

Örgülü, G., & Aktar, M. (2001). Regional moment tensor inversion for strong aftershocks of the August 17, 1999 Izmit earthquake (Mw= 7.4). *Geophysical Research Letters*, **28**(2), 371–374.

Panza, G. F., & Saraò, A. (2000). Monitoring volcanic and geothermal areas by full seismic moment tensor inversion: are non-double-couple components always artefacts of modelling? *Geophysical Journal International*, **143**(2), 353–364.

Parolai, S., Bindi, D., Baumbach, M., Grosser, H., Milkereit, C., Karakisa, S., & Zunbul, S. (2004). Comparison of different site response estimation techniques using aftershocks of the 1999 Izmit earthquake. *Bulletin of the Seismological Society of America*, **94**(3), 1096–1108.

Randall, G. E. (1994). Efficient calculation of complete differential seismograms for laterally homogeneous earth models. *Geophysical Journal International*, **118**(1), 245–254.

Ross, A., Foulger, G. R., & Julian, B. R. (1996). Non-double-couple earthquake mechanisms at the Geysers Geothermal Area, California. *Geophysical Research Letters*, **23**(8), 877–880.

Rössler, D., Krüger, F., & Rümpker, G. (2007). Retrieval of moment tensors due to dislocation point sources in anisotropic media using standard techniques. *Geophysical Journal International*, **169**(1), 136–148.

Roux, P., & Ben-Zion, Y. (2013). Monitoring fault zone environments with correlations of earthquake waveforms. *Geophysical Journal International*, **196**(2), 1073–1081.

Rudajev, V., & Šílený, J. (1985). Seismic events with non-shear component: II. Rock bursts with implosive source component. *Pure and Applied Geophysics*, **123**(1), 17–25.

Saikia, C. K. (1994). Modified frequency-wavenumber algorithm for regional seismograms using Filon's quadrature: modelling of Lg waves in eastern North America. *Geophysical Journal International*, **118**(1), 142–158.

Seeber, L., Armbruster, J. G., Ozer, N., Aktar, M., Baris, S., Okaya, D., … Field, E. (2000). The 1999 Earthquake Sequence along the North Anatolia Transform at the juncture between the two main ruptures. *The 1999 Izmit and Duzce Earthquakes: Preliminary Results*, 209–223.

Shigeishi, M., & Ohtsu, M. (2001). Acoustic emission moment tensor analysis: development for crack identification in concrete materials. *Construction and Building Materials*, **15**(5), 311–319.

Šílený, J., & Vavryčuk, V. (2000). Approximate retrieval of the point source in anisotropic media: numerical modelling by indirect parametrization of the source. *Geophysical Journal International*, **143**(3), 700–708.

Šílený, J., & Vavryčuk, V. (2002). Can unbiased source be retrieved from anisotropic waveforms by using an isotropic model of the medium? *Tectonophysics*, **356**(1), 125–138.

Šílený, J., & Milev, A. (2006). Seismic moment tensor resolution on a local scale: Simulated rockburst and mine-induced seismic events in the Kopanang gold mine, South Africa. *Pure and Applied Geophysics*, **163**(8), 1495–1513.

Šílený, J. (2009). Resolution of Non-Double-Couple Mechanisms: Simulation of Hypocenter Mislocation and Velocity Structure Mismodeling. *Bulletin of the Seismological Society of America*, **99**(4), 2265–2272.

Sipkin, S. A. (1986). Interpretation of non-double-couple earthquake mechanisms derived from moment tensor inversion. *Journal of Geophysical Research: Solid Earth (1978–2012)*, **91**(B1), 531–547.

Sokos, E. N., & Zahradnik, J. (2008). ISOLA a Fortran code and a Matlab GUI to perform multiple-point source inversion of seismic data. *Computers & Geosciences*, **34**(8), 967–977.

Stanchits, S. A., Lockner, D. A., & Ponomarev, A. V. (2003). Anisotropic changes in P-wave velocity and attenuation during deformation and fluid infiltration of granite. *Bulletin of the Seismological Society of America*, **93**(4), 1803–1822.

Stanchits, S., Vinciguerra, S., & Dresen, G. (2006). Ultrasonic velocities, acoustic emission characteristics and crack damage of basalt and granite. *Pure and Applied Geophysics*, **163**(5-6), 975–994.

Stickney, M. C., & Sprenke, K. F. (1993). Seismic events with implosional focal mechanisms in the Coeur d'Alene mining district, Northern Idaho. *Journal of Geophysical Research: Solid Earth*, **98**(B4), 6523–6528.

Stierle, E., Bohnhoff, M., & Vavryčuk, V. (2014a). Resolution of non-double-couple components in the seismic moment tensor using regional networks—II: application to aftershocks of the 1999 Mw 7.4 Izmit earthquake. *Geophysical Journal International*, **196**(3), 1878–1888.

Stierle, E., Vavryčuk, V., Šílený, J., & Bohnhoff, M. (2014b). Resolution of non-double-couple components in the seismic moment tensor using regional networks—I: a synthetic case study. *Geophysical Journal International*, **196**(3), 1869–1877.

Tchalenko, J. S. (1970). Similarities between shear zones of different magnitudes. *Geological Society of America Bulletin*, **81**(6), 1625–1640.

Templeton, D. C., & Dreger, D. S. (2006). Non-double-couple earthquakes in the Long Valley volcanic region. *Bulletin of the Seismological Society of America*, **96**(1), 69–79.

Tibi, R., Bock, G., Xia, Y., Baumbach, M., Grosser, H., Milkereit, C., … Zschau, J. (2001). Rupture processes of the 1999 August 17 Izmit and November 12 Düzce (Turkey) earthquakes. *Geophysical Journal International*, **144**(2), F1–F7.

Vavryčuk, V., & Yomogida, K. (1996). SH-wave Green tensor for homogeneous transversely isotropic media by higher-order approximations in asymptotic ray theory. *Wave Motion*, **23**(1), 83–93.

Vavryčuk, V. (2001). Inversion for parameters of tensile earthquakes. *Journal of Geophysical Research*, **106**(16), 339–16.

Vavryčuk, V. (2002). Non-double-couple earthquakes of 1997 January in West Bohemia, Czech Republic: evidence of tensile faulting. *Geophysical Journal International*, **149**(2), 364–373.

Vavryčuk, V. (2004). Inversion for anisotropy from non-double-couple components of moment tensors. *Journal of Geophysical Research*, **109**(B7), B07306.

Vavryčuk, V. (2005). Focal mechanisms in anisotropic media. *Geophysical Journal International*, **161**(2), 334–346.

Vavryčuk, V. (2007a). Asymptotic Green's function in homogeneous anisotropic viscoelastic media. *Proceedings of the Royal Society A: Mathematical, Physical and Engineering Science*, **463**, 2689–2707.

Vavryčuk, V. (2007b). On the retrieval of moment tensors from borehole data. *Geophysical Prospecting*, **55**(3), 381–391.

Vavryčuk, V. (2007c). Ray velocity and ray attenuation in homogeneous anisotropic viscoelastic media. *Geophysics*, **72**(6), D119–D127.

Vavryčuk, V., Bohnhoff, M., Jechumtálová, Z., Kolář, P., & Šílený, J. (2008). Non-double-couple mechanisms of microearthquakes induced during the 2000 injection experiment at the KTB site, Germany: A result of tensile faulting or anisotropy of a rock? *Tectonophysics*, **456**(1–2), 74–93. doi:10.1016/j.tecto.2007.08.019

Vavryčuk, V. (2010a). Focal Mechanisms abd Seismic Moment Tensors - Lecture Notes. Institute of Geophysics, The Czech Academy of Sciences.

Vavryčuk, V. (2010b). *The Amplitude Moment Tensor Inversion*. Prague: Institute of Geophysics, The Czech Academy of Sciences.

Vavryčuk, V. (2011). Tensile earthquakes: Theory, modeling, and inversion. *Journal of Geophysical Research: Solid Earth*, **116**(B12), B12320.

Vavryčuk, V. (2015a). Determination of parameters of viscoelastic anisotropy from ray velocity and ray attenuation: Theory and numerical modeling. *Geophysics*, **80**(3), in press.

Vavryčuk, V. (2015b). Moment tensor decompositions revisited. *Journal of Seismology*, **19**(1), 231–252.

Vidale, J., Helmberger, D. V., & Clayton, R. W. (1985). Finite-difference seismograms for SH waves. *Bulletin of the Seismological Society of America*, **75**(6), 1765–1782.

Yoshimitsu, N., Kawakata, H., & Takahashi, N. (2014). Magnitude− 7 level earthquakes: A new lower limit of self-similarity in seismic scaling relationships. *Geophysical Research Letters*, **41**(13), 4495–4502.

Zang, A., Wagner, F. C., Stanchits, S., Dresen, G., Andresen, R., & Haidekker, M. A. (1998). Source analysis of acoustic emissions in Aue granite cores under symmetric and asymmetric compressive loads. *Geophysical Journal International*, **135**(3), 1113–1130.

Zang, A., Wagner, F. C., Stanchits, S., Janssen, C., & Dresen, G. (2000). Fracture process zone in granite. *Journal of Geophysical Research: Solid Earth*, **105**(23), 651–661.

Acknowledgements

This dissertation was clearly only possible with the help of many people:
First of all I would like to thank my supervisor Prof. Marco Bohnhoff for giving me the opportunity to carry out my thesis in his group. Thank you for your continuous support, guidance and inspiring discussions. I am further very grateful to Dr. Vaclav Vavryčuk, my co-supervisor, for the intensive and fruitful collaboration. He introduced me into the world of moment tensors and I owe him much gratitude for the encouraging guidance and enthusiastic discussions throughout my visits in Prague.

A great thanks goes to the German Task Force for Earthquakes and especially Prof. Jochen Zschau and Dr. Claus Milkereit for providing Izmit aftershock recordings.

I thank Dr. Sergei Stanchits and Prof. Georg Dresen for kindly providing data collected during their AE experiment on the granite specimen.

A special thanks goes to the Christiane Nüsslein-Volhard Foundation for the financial support during my thesis and giving me the opportunity to exchange experiences with female scientists.

I would like to thank Dr. Jan Šílený for fruitful discussions especially at the beginning of this work. I further would like to thank Dr. Stefano Parolai and Dr. Dino Bindi for discussions about the Izmit earthquake and especially on attenuation issues.

Thank you Dr. Grzegorz Kwiatek and Dr. Fatih Bulut for the enlightening discussions and for helping me with all the programming issues.

I would like to thank the GFZ-Section 3.2 crew for the pleasant atmosphere, all the cakes in our cozy corner, the coffee breaks on the roof, and the after-work beer clubs. In particular, I would like to thank my PhD fellows Michele, Elmar, Maike (and Wanda), Vanessa, Tina, Christopher, Bita, Patricia, Digdem, Olli, Mark and Roman. Some of you are not only colleagues but became also friends! A special thanks goes to Rita for making my live at GFZ easier.

Thanks a lot to Jessica for carefully reading and spell-checking my thesis.

A very special thanks goes to my parents! Your firm believe in myself and your willingness to always be there for me form the basis of what I am now.

At last I want to thank the most important people in my live: Peter, Jannes, and Emil!